

A light-matter quantum interface: ion-photon entanglement and state mapping

Dissertation

zur Erlangung des Doktorgrades an der
Fakultät für Mathematik, Informatik und Physik
der Leopold-Franzens-Universität Innsbruck

vorgelegt von

Andreas Stute

durchgeführt am Institut für Experimentalphysik
unter der Leitung von
Univ.-Prof. Dr. Rainer Blatt

Innsbruck, Dezember 2012

Abstract

Quantum mechanics promises to have a great impact on computation. Motivated by the long-term vision of a universal quantum computer that speeds up certain calculations, the field of quantum information processing has been growing steadily over the last decades. Although a variety of quantum systems consisting of a few qubits have been used to implement initial algorithms successfully, decoherence makes it difficult to scale up these systems. A powerful technique, however, could surpass any size limitation: the connection of individual quantum processors in a network.

In a quantum network, “flying” qubits coherently transfer information between the stationary nodes of the network that store and process quantum information. Ideal candidates for the physical implementation of nodes are single atoms that exhibit long storage times; optical photons, which travel at the speed of light, are ideal information carriers. For coherent information transfer between atom and photon, a quantum interface has to couple the atom to a particular optical mode.

This thesis reports on the implementation of a quantum interface by coupling a single trapped $^{40}\text{Ca}^+$ ion to the mode of a high-finesse optical resonator. Single intracavity photons are generated in a vacuum-stimulated Raman process between two atomic states driven by a laser and the cavity vacuum field. In this Raman process, all Zeeman substates of the atom are spectroscopically resolved by tuning the frequency of the laser; via addressing specific atomic states, the polarization of the generated cavity photon is controlled, defining the photonic qubit. The electronic state of the ion is initialized, coherently manipulated, and read out via driving the quadrupole transition.

With these techniques in hand, we have demonstrated two protocols for quantum communication. The first protocol, ion-photon entanglement, is regarded as a key resource of distributed quantum information processing. In our realization, we control both phase and amplitude of the entangled ion-photon state, resulting in a state fidelity of $(97.4 \pm 0.2)\%$. The second protocol, ion-photon state mapping, realizes a faithful transfer of the qubit state from the stationary to the flying qubit with a maximum process fidelity of $(92 \pm 2)\%$. The bichromatic driving scheme that we have developed enables time-independence of the quantum states in both protocols, making this scheme applicable to a variety of physical systems incorporating non-degenerate qubit states.

In the future, the ion-photon interface that we have demonstrated will enable the coupling of distant ions; furthermore, it may allow for the optical coupling of an ion to other quantum systems, such as quantum dots or superconducting qubits. Such a hybrid quantum system could combine the advantages of the individual systems.

Zusammenfassung

Die Gesetze der Quantenmechanik versprechen, die Computertechnologie zu revolutionieren. Motiviert von der Vision eines universellen Quantencomputers ist das Forschungsfeld der Quanteninformationsverarbeitung in den letzten Jahrzehnten kontinuierlich gewachsen. Obwohl erste Algorithmen erfolgreich in kleinen Quantensystemen mit einigen Quantenbits (Qubits) implementiert wurden, stellt die Skalierbarkeit dieser Systeme eine große Herausforderung dar. Hier könnte eine bewährte Technik klassischer Computer helfen: Die Verbindung individueller Quantenprozessoren in einem Netzwerk.

In einem solchen Quantennetzwerk übermitteln „fliegende“ Qubits kohärent Information zwischen stationären Knotenpunkten des Netzwerkes, welche die Quanteninformation speichern und verarbeiten. Ideal für die technische Realisierung der Knotenpunkte sind einzelne Atome, da sie lange Kohärenzzeiten besitzen. Als „fliegende“ Qubits eignen sich optische Photonen, die in einer Glasfaser übertragen werden können. Für den reversiblen Informationstransfer zwischen Atom und Photon wird eine Quantenschnittstelle benötigt, welche das Atom gezielt an eine optische Mode koppelt.

Die vorliegende Arbeit beschreibt die Realisierung einer solchen Schnittstelle, in der ein einzelnes $^{40}\text{Ca}^+$ -Ion an die Mode eines optischen Resonators hoher Güte gekoppelt wird. Einzelne Photonen werden über einen Ramanprozess zwischen zwei atomaren Zuständen erzeugt. Dieser Ramanprozess wird vom Vakuumfeld des Resonators und von einem Laser getrieben. Über die Frequenz des Lasers werden alle Zeemanzustände des Atoms spektroskopisch aufgelöst und die Polarisation des erzeugten Photons kontrolliert. Die Polarisation des Photons definiert das „fliegende“ Qubit, und der elektronische Zustand des Atoms definiert das stationäre Qubit, welches über einen Quadrupolübergang initialisiert, manipuliert und ausgelesen wird.

Diese Techniken wurden anschließend angewendet, um zwei Protokolle für die Quantenkommunikation zu realisieren. Im ersten Protokoll wurde Atom-Photon-Verschränkung erzeugt, die eine universelle Ressource für die Quantenkommunikation darstellt. In unserer Realisierung werden Phase und Amplitude des verschränkten Atom-Photon-Zustandes mit einer Zustands-Fidelity von $(97.4 \pm 0.2)\%$ kontrolliert. Im zweiten Protokoll wurde ein beliebiger Quantenzustand des Atoms kohärent auf das Photon übertragen. Hierbei beträgt die maximale Prozess-Fidelity $(92 \pm 2)\%$. Das von uns entwickelte Anregungsschema mittels zweier phasenkohärenter optischer Felder stellt die Zeitunabhängigkeit der Quantenzustände in beiden Protokollen sicher. Dieses Schema ist daher auf beliebige physikalische Systeme mit nichtentarteten Qubitzuständen anwendbar.

In Zukunft wird die hier realisierte Quantenschnittstelle die Kopplung entfernter Ionen sowie die Kopplung eines Ions an andere Quantensysteme wie Quantenpunkte oder supraleitende Qubits ermöglichen. Ein solches hybrides Quantensystem ermöglicht, die Vorteile der individuellen Systeme zu vereinen.

*Quand tu veux construire un bateau,
ne commence pas par rassembler du bois,
couper des planches et distribuer du travail,
mais réveille au sein des hommes
le désir de la mer grande et belle.*

*Wenn du ein Schiff bauen willst, dann trommle nicht Menschen zusammen
um Holz zu beschaffen, Aufgaben zu vergeben und die Arbeit einzuteilen,
sondern lehre die Menschen die Sehnsucht nach dem weiten, endlosen Meer.*

Antoine de Saint-Exupéry, Citadelle

Contents

1	Introduction	1
2	Coupling an atomic qubit to a photon qubit	7
2.1	Quantum bits	7
2.2	Two-level system coupled to a cavity	12
2.3	Three-level system: vacuum-stimulated Raman transitions	15
3	States and transitions in $^{40}\text{Ca}^+$ for an ion-photon interface	19
3.1	Trapped calcium ions as quantum bits	19
3.2	Transitions for generating single photons	21
3.3	Model: Eighteen-level system coupled to two cavity modes	22
4	Experimental setup	29
4.1	Overview	29
4.2	Linear Paul trap	31
4.3	Optical cavity	32
4.4	Laser systems	34
4.5	Transfer lock	39
4.6	Laser beam geometry	42
4.7	Ion addressing	44
4.8	Magnetic field	45
4.9	Atomic fluorescence detection	47
4.10	Photon state detection	47
4.11	Radiofrequency generation and data acquisition	50
4.12	Technical considerations for a new setup	51
5	Atomic qubit	53
5.1	Experimental sequence	53
5.2	Doppler cooling	53
5.3	State initialization	56
5.4	State detection	57
5.5	Coherent manipulation of the atomic qubit	58
5.6	Sideband cooling	59
5.7	Atomic coherence time: Ramsey spectroscopy	61
5.8	Minimization of micromotion	65

6	Controlling the ion-cavity coupling	69
6.1	Localization in the standing wave	69
6.2	Probing the radial structure of the cavity mode	70
7	Cavity-assisted Raman spectroscopy	75
7.1	Geometry of beams and magnetic field	75
7.2	Raman spectra for different geometries	79
7.3	Motional sidebands	82
8	Tunable ion-photon entanglement	85
8.1	Motivation	85
8.2	Entanglement and Bell inequalities	86
8.3	Bichromatic Raman transition	88
8.4	Experimental sequence and temporal pulse-shape overlap	91
8.5	Quantum state tomography	93
8.6	Time independence of the entangled state	96
8.7	Tunable phase of the entangled state	99
8.8	Tunable amplitudes of the entangled state	99
8.9	Experimental imperfections	101
8.10	Conclusion	102
9	Ion-photon state mapping	105
9.1	Description of the protocol	105
9.2	Implementation of the protocol	105
9.3	Quantum process tomography	108
9.4	Time evolution of the photon polarization	109
9.5	Time independence of the mapping process	112
9.6	Conclusion	114
10	Summary and Outlook	115
A	Battery circuit for trap-cavity piezo control	117
B	Journal publications	119
	Bibliography	131
	Danksagung	133

1 Introduction

Quantum mechanics represents one of the greatest advances in physics in the twentieth century. Not only does it explain fundamental phenomena in atomic physics, chemistry, material sciences, and many more areas of modern science, but also it has mediated the engineering of materials such as semiconductors, which resulted in the technical revolution of classical computation.

In the last decades, it was discovered that certain principles of quantum mechanics promise to have a great impact on computation. While classical qubits are in state 0 or one, quantum bits (qubits) can be in a superposition state. As the large state space of quantum systems makes them difficult to simulate, Benioff and Feynman proposed in the early 1980s to use one quantum system to simulate another [1, 2]. At that time, however, such ideas were considered pure thought experiments. This changed with the development of algorithms that exploit superposition and interference principles of quantum mechanics to turn (exponentially) hard mathematical problems on a classical digital computer into easy (polynomial) ones on a quantum computer. The most prominent examples of this quantum speedup are Shor’s algorithm for prime factorization [3] and Grover’s search algorithm [4]. Moreover, Bennet and Brassard developed a first *quantum cryptography* protocol [5]: a quantum key distribution enabling intrinsic secure communication based on the laws of quantum physics.

Given these opportunities, many technologies have since been investigated with the goal of implementing a quantum computer [6, 7]. A variety of quantum systems consisting of a few qubits have been demonstrated to be capable of quantum operations and have been used to successfully implement first algorithms. Among these systems are photons, nuclear spins, quantum dots, superconducting qubits, neutral atoms, and trapped ions [6, 7]. What started as a thought experiment 30 years ago has become the field of quantum information science.

However, both decoherence in real-world quantum systems and the inaccuracy of an inherent analogue system mean that it will be difficult to scale up quantum systems [8]. Major developments that allow for the realization of large-scale quantum computers despite these obstacles are *error-correction protocols* [9, 10] and methods for *fault-tolerant quantum computation* [8]. These protocols have been successfully implemented [11–13] and would in principle allow for a scaling-up of error-afflicted systems, but they require a significant overhead in the number of physical qubits. In addition, at any stage in the development of quantum computers, the state space and the computational power of any individual quantum processor will be limited.

In order to surpass this limited size and to overcome the error-correction overhead, a powerful technique of classical computation can be introduced: the connection of

individual processors in a network. Processors now share resources and information, and computation can be distributed among the network's individual units. In the quantum version of a computational network [14–16], the nodes of the network have to be capable of generating, storing, and processing quantum information, and the connecting channels have to coherently transfer the analogue quantum information between the individual nodes. The concepts of *quantum networks* and *quantum communication* not only appear promising for the distribution of computational tasks, but are also combined into new applications such as blind quantum computing [17]. In this scheme, the formulation of a certain task and its computation on a remote quantum server are hidden from each other, possibly enabling the secure use of initial quantum servers running at specialized facilities.

The technological prerequisites for quantum computation are often referred to as the five *DiVincenzo criteria* [18]. Two additional DiVincenzo criteria stipulate the requirements for *quantum communication*: a coherent interface between *stationary* and *flying* qubits as well as transmission of flying qubits between remote locations [18]. For the physical implementation of flying qubits, photons in the optical domain have proven to be ideal information carriers; they are transmitted at the speed of light through optical fibers or the atmosphere with little disturbance [19]. The flying qubit itself can be encoded in different degrees of freedom, such as polarization, wavelength or photon arrival time. The nodes of a quantum network can be realized by matter qubits that exhibit long storage times. In contrast to solid-state devices such as quantum dots and superconducting qubits, atoms are indistinguishable by nature. As a consequence, their properties can be exactly reproduced at any node of the network. Two well-studied approaches in the context of quantum networks are single atoms [14, 20–22] and atomic ensembles [23, 24]. Here, we focus on single, trapped atoms. For coherent information transfer between atom (stationary qubit) and photon (flying qubit), a *quantum interface* has to couple the atom to a particular optical mode, as implemented by two different approaches.

The *probabilistic approach* selects photons over a limited solid angle [21, 25]. Only a small fraction of photons, typically on the percent level, are therefore collected. In contrast, by placing the atom inside a low-loss cavity, its coupling to the cavity mode is enhanced. The atom is said to be *strongly coupled* to the cavity mode if this atom-cavity coupling strength is much larger than both the atom's and the cavity's coupling to the other optical vacuum modes. As photons can be generated with near-unit efficiency in such cavity systems [26, 27], this approach is called the *deterministic approach* [14, 15]. The strongest coupling is achieved with small-mode-volume cavities, where the mode volume is inversely proportional to cavity length. For ions, achieving a strong ion-field coupling is quite challenging due to the difficulty of integrating mirrors within an ion-trap apparatus. In contrast, cavities of just tens of μm in length are possible in experiments with neutral atoms [28]. It is thus in the context of neutral atoms that the greatest progress toward a cavity-based interface has been demonstrated [22, 29, 30].

Depending on the network topology and the interface approach, different quantum communication protocols can be employed. In this thesis, we focus on two protocols: a first one that generates distant entanglement and a second one that directly transfers a quantum state between two distant nodes. The next paragraphs first describe these protocols and their realizations by other research groups worldwide and then motivate the approach of this thesis.

The first protocol generates entanglement between distant matter qubits, a resource for quantum communication. It can be realized in both the deterministic and the probabilistic interface approach and makes use of entanglement between the state of a single photon and the state of an atomic or solid-state quantum memory, as has been demonstrated in recent experiments with trapped ions [25, 31], neutral atoms [21, 22, 32], atomic ensembles [33, 34], and nitrogen-vacancy spins [35]. By interference of two photons that are entangled with their respective emitters, probabilistic entanglement between the distant emitters can be achieved, as recently demonstrated with single ions [36], atomic ensembles [37], and single neutral atoms [22, 38]. Once entanglement between distant matter qubits is accomplished, it can be used for different communication protocols, e.g., state transfer between remote qubits via quantum teleportation [31].

The success probability of this first protocol, using the probabilistic approach, is typically on the order of $10^{-7} - 10^{-9}$ [36, 38]. This small efficiency, however, does not affect the fidelity of the process since the detection of photons heralds a successful event and realizes an *inherent error detection* [15]. For long distances between the stationary qubits, however, the optical channel will introduce further losses due to scattering and absorption that scale exponentially with its length. In the classical world, such losses are mitigated by the use of repeaters that periodically amplify the signal. Although quantum states can not be amplified or copied [39], a *quantum repeater* can be realized via a more complex protocol, invented by Briegel et. al. [40]. Here, additional qubits at intermediate nodes are used for entanglement swapping and purification steps, enabling long-distance quantum communication with only polynomial overhead in time and the number of qubits [40].

In the second protocol, a quantum state is directly transferred between two nodes. The original proposal [41] makes use of the deterministic approach: the state is transferred from a first atom onto a cavity photon, which carries it over an optical channel to a second atom-cavity system. This second protocol has recently been realized with single, neutral atoms [22], employing the polarization of a single photon as a flying qubit. Due to scattering and absorption in optical elements, however, the success probability of the protocol is below one. Although in principle the efficiency to generate and receive photons in atom-cavity interfaces can approach unity, optical losses during the transfer will always result in an overall probabilistic transfer protocol. Nevertheless, high fidelities can be reached by a complementary version of inherent error detection: if photons are generated and received in a Raman transition, detection of a particular atomic state heralds the absorption of a photon. Once a heralding technique

can be applied, this second protocol could be realized as well using the probabilistic approach, although with lower efficiency. It may also be possible to implement another quantum repeater scheme based on this second protocol.

Deterministic or not, the cavity approach has proven to enable much higher efficiencies than the approach of collecting photons over a limited solid angle. Additionally, a herald allows for the realization of probabilistic protocols by the cavity approach. The cavity approach thus combines versatility with a high efficiency. In addition, for all protocols that rely on the initialization or the read-out of the atomic state, the success probability of the protocol increases with the efficiency of atomic state initialization and read-out. Here, trapped ions have the advantage of deterministic methods for coherent state manipulation and readout [42, 43]. Although these methods have also been demonstrated for neutral atoms [44, 45], they have not yet been combined with the cavity interface.

Integrating a single trapped ion with a high-finesse cavity would thus combine two efficient techniques and realize the natural archetype of a quantum interface. Additionally, trapped ions offer long storage times, precise positioning with respect to the cavity mode and a localization to about 10 nm via ground-state cooling in three dimensions [42]. Due to the difficulty of combining an ion-trap with a small-mode-volume cavity, however, ion-trap cavities to date have only been constructed on the cm scale [46–51], without reaching strong coupling between a single atom and a single photon. Special techniques have thus to be developed for the successful implementation of such a quantum interface.

In this dissertation, the potential of an ion-cavity system to improve both efficiency and fidelity of quantum network protocols is explored. The main results are the implementation of ion-photon entanglement and state mapping which are published in [52–54].

This dissertation is structured as follows: chapter 2 reviews the concepts of quantum information and cavity-quantum electrodynamics. It introduces the cavity-driven Raman transition for realizing the quantum interface. In chapter 3, states and transitions in $^{40}\text{Ca}^+$ for an ion-photon interface are discussed, and a theoretical model is introduced. Chapter 4 describes the experimental apparatus consisting of ion trap, cavity, and laser systems. Additionally, the polarization detection of the photonic qubit is explained. After an introduction of the level scheme of $^{40}\text{Ca}^+$, chapter 5 explains the experimental tools for initialization, coherent manipulation, and state detection of the atomic qubit, focusing on recently improved techniques. In chapter 6, control over the relative ion-cavity position in all three spatial dimensions is demonstrated. As a result, the ion-cavity coupling is maximized. Chapter 7 discusses the choice of states and transitions in $^{40}\text{Ca}^+$ and an optimal experimental geometry for an ion-photon interface. Via Raman spectroscopy, specific qubit states are addressed and single cavity photons with the desired polarization are generated. As a first quantum interface protocol, entanglement between a single ion and a single photon is demon-

strated in chapter 8 with a fidelity of $(97.4 \pm 0.2)\%$. A bichromatic driving scheme enables both tunability and time-independence of this ion-photon entanglement. A second protocol is implemented in chapter 9: the mapping of the quantum state of a single ion onto a single photon within the cavity with a maximum process fidelity of $(92 \pm 2)\%$. The mapping process is time-independent, allowing us to characterize the interplay between efficiency and process fidelity. Finally, chapter 10 summarizes the results presented and provides an outlook to future experiments.

2 Coupling an atomic qubit to a photon qubit

An ion-photon interface requires the interaction between two well-defined qubits, one atomic and one photonic. After a short introduction to the theoretical notation of a qubit's quantum state and its visualization on the Bloch or Poincaré sphere, this chapter defines the atomic and photonic qubits employed in this work and introduces the concept of quantum-state measurement.

In the second part of this chapter, we introduce the Jaynes-Cummings model that describes the interaction of a cavity with a two-level system. Although the fundamental phenomena of the atom-cavity interaction can be analyzed in this model, the experiments described in this thesis employ a Raman transition, and the atom is more appropriately described as a three-level system. We thus extend the theoretical model to a third atomic level and a coherent external drive field. Via adiabatic elimination of one level, this model can be reduced to an effective two-level system that qualitatively reveals most of the experimental phenomena observed. Finally, we discuss the coherence of the Raman process, an important figure of merit that determines fidelity and efficiency of the ion-photon interface.

2.1 Quantum bits

Every *bit*, the smallest unit of information in a classical computer, has two logical values, 0 and 1, and is therefore physically implemented by devices that possess two states. In contrast to a classical qubit, a *quantum bit (qubit)* can be in any superposition of the two states $|0\rangle$ and $|1\rangle$:

$$\alpha |0\rangle + \beta |1\rangle. \tag{2.1}$$

Physical implementations of qubits are, e.g., a two-level atom, the polarization of a spin-1/2 particle, or the polarization of a single photon.

In the ideal case, a qubit is isolated from its environment and can mathematically be described as a closed system. It is then characterized by a pure state, i.e., a state vector $|\psi\rangle$ of the two-dimensional Hilbert space \mathcal{H}_2 , spanned by the basis vectors $|0\rangle \equiv \begin{pmatrix} 1 \\ 0 \end{pmatrix}$ and $|1\rangle \equiv \begin{pmatrix} 0 \\ 1 \end{pmatrix}$. For the normalization of every state vector, the complex amplitudes $\alpha, \beta \in \mathbb{C}$ must fulfill $|\alpha|^2 + |\beta|^2 = 1$. One can then express the pure state $|\psi\rangle$ in terms of the two real parameters ϑ, φ :

$$|\psi\rangle = \cos \vartheta |0\rangle + e^{i\varphi} \sin \vartheta |1\rangle. \tag{2.2}$$

In reality, however, every physical qubit couples to its environment and therefore suffers from decoherence. To describe a system realistically, the mathematical formalism of the density matrix is used. Rather than describing the state of a single quantum system, the density matrix describes an ensemble of quantum states. It thus takes into account the fact that in quantum mechanics, one always has to measure an ensemble of identically prepared particles in order to assign a ‘state’ to the ensemble. In general, an ensemble of quantum states consists of a statistical mixture of pure states $|\psi_i\rangle$, each with probability p_i . Such a mixed ensemble is described by the density matrix

$$\rho = \sum_{i=1} p_i |\psi_i\rangle\langle\psi_i| \quad (2.3)$$

with p_i real, positive and normalized such that $\sum_{i=1} p_i = 1$. The density matrix is Hermitian and normalized: $\rho^\dagger = \rho$, $\text{tr}[\rho] = 1$. In the case of a classical mixture of two states, e.g., where half of the representatives of the ensemble are in state $|0\rangle$ and the other half in state $|1\rangle$, the density matrix $\rho = |0\rangle\langle 0| + |1\rangle\langle 1|$ represents a completely mixed ensemble (for convenience, the term ‘ensemble’ is often replaced by ‘state’). On the contrary, if all representatives of the ensemble are in the same quantum state, e.g. $|0\rangle$, the density matrix $\rho = |0\rangle\langle 0|$ represents a pure ensemble. In order to measure the degree to which an ensemble is mixed, the purity $\text{tr}[\rho^2]$ is used. In the case of a pure ensemble, the purity yields 1; for a completely mixed state, it is $1/2$. (In general, the purity of a completely mixed state is $1/d$, where d is the dimension of the Hilbert space.)

In order to describe the state of two qubits, the state vectors of both qubits are combined via the tensor product $|\psi_i^{(1)}\rangle \otimes |\psi_i^{(2)}\rangle$, and the Hilbert space \mathcal{H}_{tot} of two qubits is the tensor product of the Hilbert spaces of the two subsystems $\mathcal{H}_{tot} = \mathcal{H}_2^{(1)} \otimes \mathcal{H}_2^{(2)}$.

Physical implementation of the atomic and photonic qubit

The experiments presented in this thesis employ two different qubits: the electronic state of a single ion and the polarization state of a single photon. For the ion, different electronic states can be used to implement a physical qubit (sec. 3.1.2). For the ion-photon entanglement experiment of chapter 8, for example, the states $|D\rangle \rightarrow |0\rangle$ and $|D'\rangle \rightarrow |1\rangle$ define the atomic qubit.

The photonic qubit is defined via the polarization states of a single photon throughout this thesis: $|H\rangle \rightarrow |0\rangle$ and $|V\rangle \rightarrow |1\rangle$, where H and V represent a horizontally and vertically polarized photon, respectively. The orthogonal polarization states that correspond to the axes of the Poincaré sphere can be written as linear combinations of H and V and are listed in table 2.1.

2.1.1 Bloch-and Poincaré sphere representation

A convenient and intuitive illustration of the state of a qubit is given by the Bloch- or Poincaré sphere. Due to normalization and hermiticity, the density matrix ρ of a

polarization name	polarization state	qubit state
horizontal (linear)	$ H\rangle$	$ 0\rangle$
vertical (linear)	$ V\rangle$	$ 1\rangle$
diagonal (linear)	$ D\rangle = \frac{1}{\sqrt{2}}(H\rangle + V\rangle)$	$ +\rangle_x = \frac{1}{\sqrt{2}}(0\rangle + 1\rangle)$
anti-diagonal (linear)	$ A\rangle = \frac{1}{\sqrt{2}}(H\rangle - V\rangle)$	$ -\rangle_x = \frac{1}{\sqrt{2}}(0\rangle - 1\rangle)$
right circular	$ R\rangle = \frac{1}{\sqrt{2}}(H\rangle + i V\rangle)$	$ +\rangle_y = \frac{1}{\sqrt{2}}(0\rangle + i 1\rangle)$
left circular	$ L\rangle = \frac{1}{\sqrt{2}}(H\rangle - i V\rangle)$	$ -\rangle_y = \frac{1}{\sqrt{2}}(0\rangle - i 1\rangle)$

Table 2.1: Photon polarization states that are used for state tomography and their corresponding qubit states.

single qubit can be decomposed in the Pauli-operator basis [55]

$$\rho = \frac{1}{2}(\mathbb{1} + \vec{r} \cdot \vec{\sigma}) \quad (2.4)$$

with the Bloch (or polarization) vector \vec{r} , the unit vectors \hat{e}_i , and $\vec{\sigma} = \sigma_x \hat{e}_x + \sigma_y \hat{e}_y + \sigma_z \hat{e}_z$, where the Pauli-spin matrices are

$$\sigma_x = \begin{pmatrix} 0 & 1 \\ 1 & 0 \end{pmatrix}, \sigma_y = \begin{pmatrix} 0 & -i \\ i & 0 \end{pmatrix}, \sigma_z = \begin{pmatrix} 1 & 0 \\ 0 & -1 \end{pmatrix}. \quad (2.5)$$

As a consequence, a distinct Bloch vector \vec{r} can be assigned to each state ρ via the expectation value of $\vec{\sigma}$: $\vec{r} = \text{tr}[\rho \vec{\sigma}] = \langle \vec{\sigma} \rangle$. As $\vec{r} \in \mathbb{R}^3$, it can be characterized by its Cartesian coordinates (r_x, r_y, r_z) or its polar coordinates $(r = |\vec{r}|, \vartheta, \varphi)$. For a pure state $|\psi\rangle$, $r = |\vec{r}| = 1$, and the tip of the Bloch vector \vec{r} lies on the surface of the three-dimensional unit sphere which for this purpose is called the Bloch (or Poincaré) sphere, shown in fig. 2.1. For a mixed state, $r \leq 1$, and the the Bloch vector lies within the sphere.

In addition to illustrating a certain quantum state, the Bloch and Poincaré sphere can also be employed to illustrate the measurements necessary for state tomography.

2.1.2 Quantum state measurement for tomography

In order to evaluate the ion-photon entanglement and state mapping experiments presented in chapter 8 and chapter 9, the resulting quantum states of ion and photon have to be characterized. Such characterization is realized via tomographic measurements in which the expectation value of certain observables is measured for a number of identically prepared quantum systems. In general, a measurement of observable \mathcal{A} projects a quantum state into an eigenstate of \mathcal{A} . The expectation value of \mathcal{A} is given by

$$\langle \mathcal{A} \rangle = \text{tr}[\mathcal{A}\rho]. \quad (2.6)$$

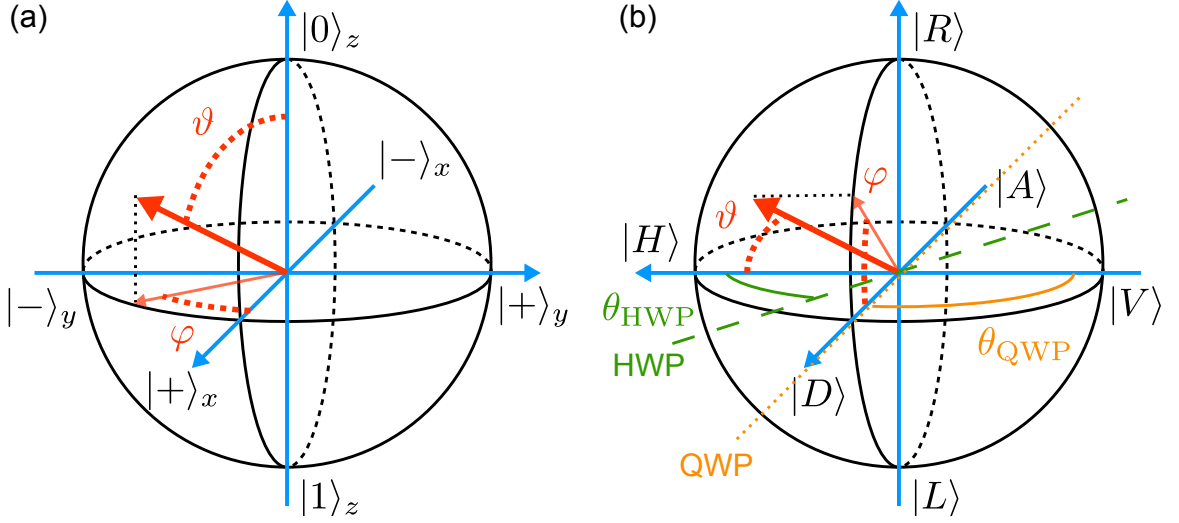


Figure 2.1: (a) Bloch sphere and (b) Poincaré sphere. While the Bloch sphere is typically oriented such that the states $|0\rangle_z$ and $|1\rangle_z$ lie on the north and south pole, the Poincaré sphere is typically oriented such that linear polarizations lie in the equator, and the north and south poles of the sphere represent circular polarizations. The Bloch vector (red) is characterized via two real parameters ϑ and φ . Rotation axes on the Poincaré sphere caused by half- and quarter-waveplates at angle θ with respect to the optical axis are indicated by the green dashed and orange dotted line, respectively.

A measurement of σ_z , e.g., for the pure state of eq. (2.2), projects the state into $|0\rangle$ (the north pole of the Bloch sphere) with probability $\cos^2(\vartheta)$ and into $|1\rangle$ (the south pole) with probability $\sin^2(\vartheta)$. From the probabilities obtained, however, one can only assign the angle ϑ , i.e., an intersecting plane of the Bloch sphere with a plane parallel to the x - and y -axes. In order to assign a Bloch vector, i.e., the second parameter φ , the state also has to be projected along two different directions, e.g., x and y , corresponding to measurements of σ_x and σ_y .

While the measurement of σ_z is implemented for the ion via the fluorescence detection method (explained in sec. 5.4) and for the photon via a polarizing beamsplitter (PBS), the two additional observables σ_x and σ_y are measured via the application of rotations on the qubit before the projective measurement. These rotations are described by unitary operations \hat{U} that can be interpreted as acting either on the state $\rho \rightarrow \hat{U}\rho\hat{U}^\dagger$ (Schrödinger picture) or on the operator $\mathcal{A} \rightarrow \hat{U}^\dagger\mathcal{A}\hat{U}$ (Heisenberg picture). The expectation value is equal in both cases: $\text{tr}[\mathcal{A}\hat{U}\rho\hat{U}^\dagger] = \text{tr}[\hat{U}^\dagger\mathcal{A}\hat{U}\rho]$. In the second interpretation, the Bloch sphere is rotated with respect to the vector. As the measurement direction remains the north-south axis, the measured observable, in general, now has components of σ_x and σ_y .

The physical implementation of such rotations is realized in a different way for the ion and the photon. For the ion, unitary rotations are realized via laser pulses

with certain length and phase. As shown in [56], a laser pulse resonant with the qubit transition with Rabi frequency Ω , pulse duration t and phase ϕ causes a unitary operation $\hat{U}(t)$ on the state (or the observable) with

$$\hat{U}(t, \phi) = \begin{pmatrix} \cos(\Omega t) & -ie^{-\phi} \sin(\Omega t) \\ -ie^{\phi} \sin(\Omega t) & \cos(\Omega t) \end{pmatrix} \quad (2.7)$$

As shown in [55], every unitary operation \hat{U} on the Hilbert space \mathcal{H}_2 of a qubit can be interpreted as a rotation of the qubit's Bloch vector. For the unitary operation of eq. (2.7), the rotation axis, given by $\cos(\phi)\hat{e}_x + \sin(\phi)\hat{e}_y$, is restricted to the equator of the Bloch sphere. The rotation angle is determined by Ωt . For $\phi = 0$, for example, the Bloch vector is rotated along the x -axis of the Bloch sphere, while $\phi = \pi/2$ results in a rotation along the y -axis. For a rotation angle of $\Omega t = \pi/2$ (a so-called π -pulse), north and south pole are exchanged. If we choose $\Omega t = \pi/4$ (a so-called $\pi/2$ -pulse), the rotation angle is 90° , and north and south pole are rotated to the equator. In order to measure σ_x and σ_y , we thus apply rotations on the ion with $\phi = 0, \Omega t = \pi/4$ and $\phi = \pi/2, \Omega t = \pi/4$, respectively.

The polarization state of a single photon is measured with optical detectors at both output ports of a PBS that projects the polarization to $|H\rangle$ or $|V\rangle$. In order to measure in a different basis, unitary rotations are realized via birefringent optical crystals, known as waveplates, that are mounted in front of the PBS (sec. 4.10). Common waveplates are half- and quarter-waveplates (HWP and QWP, respectively). Their names correspond to the maximum phase retardation that is imposed on the polarization along the ordinary or extraordinary axis of the crystal at a specific wavelength. The unitary rotations \hat{U}_{HWP} and \hat{U}_{QWP} that are caused by the two waveplates are given in [57] as:

$$\hat{U}_{\text{HWP}}(\theta) = e^{i\pi/2} \begin{pmatrix} \cos(2\theta) & \sin(2\theta) \\ \sin(2\theta) & -\cos(2\theta) \end{pmatrix} \quad (2.8)$$

$$\hat{U}_{\text{QWP}}(\theta) = \frac{1}{\sqrt{2}} \begin{pmatrix} 1 + i \cos(2\theta) & i \sin(2\theta) \\ \sin(2\theta) & 1 - i \cos(2\theta) \end{pmatrix}, \quad (2.9)$$

where θ corresponds to the physical angle of the waveplate with respect to the optical axis and not the angle of rotation in the Poincaré sphere. The half-waveplate causes a rotation of the polarization vector on the Poincaré sphere by the fixed angle of 180° around an axis in the equatorial plane of the Poincaré sphere. For any angle of the HWP, linear polarizations thus stay linear, while right- and left circular polarizations are exchanged. The rotation axis is defined by the optical axis of the waveplate. For $\theta = 22.5^\circ$, the rotation axis is identified to be the green dashed line in fig. 2.1(b). For this setting of the HWP, $|H\rangle \leftrightarrow |D\rangle$ and $|V\rangle \leftrightarrow |A\rangle$ are exchanged. As a consequence, a measurement along the axis of $|D\rangle, |A\rangle$ is realized.

The quarter-waveplate causes a rotation of the polarization vector by the fixed angle of 90° around an axis determined in the same way as for the half-waveplate.

A QWP can thus be used to rotate states to or from the equator. For $\theta = 45^\circ$, the rotation axis is the axis of $|D\rangle, |A\rangle$ as indicated by the orange dotted line in fig. 2.1(b). As a consequence, the circular polarizations are rotated $|R\rangle \rightarrow |V\rangle$ and $|L\rangle \rightarrow |H\rangle$. This setting of the QWP thus allows for a measurement along the axis of $|R\rangle, |L\rangle$.

In summary, we have defined the atomic and photonic qubits and described how measurements along different directions of the Bloch or Poincaré sphere can be realized via laser pulses or waveplate angles. In the remainder of the chapter, we introduce the theoretical model of the atom-cavity interaction.

2.2 Two-level system coupled to a cavity

A simple model for the interaction of an atom with a light field is given by the Jaynes-Cummings formalism [58]. This model treats the atom as an idealized two-level system that interacts with single photons of a quantized mode of the electromagnetic field, described by the excitations of a quantum harmonic oscillator (fig. 2.2(a)). This model describes a realistic situation if the coupling between atom and resonator is large compared to their couplings to the environment. Additionally, the normal modes of the resonator are assumed to be well separated in frequency and only one of them populated with photons. For an atom at rest, the Jaynes-Cummings Hamiltonian is given by

$$\mathcal{H} = (\hbar\omega_0/2)\sigma_z + \hbar\omega_c(\hat{a}^\dagger + a) + \hbar g(\sigma^+ + \sigma^-)(\hat{a} + \hat{a}^\dagger). \quad (2.10)$$

Here, $\hbar\omega_0$ is the energy splitting between the ground state $|g\rangle$ and excited state $|e\rangle$ of the atom, and $\sigma^+ = |e\rangle\langle g|$ and $\sigma^- = |g\rangle\langle e|$ are the atomic raising and lowering operators, respectively. The operators \hat{a}^\dagger and \hat{a} are the creation and annihilation operators of the electromagnetic field mode of the resonator with a single photon energy of $\hbar\omega_c$. In the dipole approximation, the maximum atom-cavity coupling strength g for an atom that is well-localized within the resonator standing wave is given by the scalar product of the atomic dipole moment $\vec{\mu}_{eg}$ and the electric field vector of the resonator \vec{E}_c

$$\hbar g = -\vec{\mu}_{eg} \cdot \vec{E}_c. \quad (2.11)$$

Out of the four coupling terms in eq. (2.10), the term $\sigma^+\hat{a}^\dagger$ corresponds to a photon being generated in the resonator and the atom changing to the excited state, while the term $\sigma^-\hat{a}$ corresponds to one photon being absorbed and the atom changing to the ground state. These two terms that rotate at fast frequency $\omega_0 + \omega_c$, do not conserve energy and can only be allowed on times scales in accordance with the uncertainty principle. Typically, we are interested in the dynamics that take place over many optical cycles [59]. If the optical frequencies ω_0 and ω_c are much larger than the coupling constant g , the fast rotating terms at frequency $\omega_0 + \omega_c$ average out in the Heisenberg equations of motion. The Jaynes-Cummings Hamiltonian in this *rotating wave approximation* thus considers only the energy conserving terms $\sigma^+\hat{a}$ and $\sigma\hat{a}^\dagger$,

rotating at slow frequency $|\omega_0 - \omega_c|$:

$$\mathcal{H} = \frac{\hbar\omega_0}{2}\sigma_z + \hbar\omega_c(\hat{a}^\dagger + \hat{a}) + \hbar g(\sigma^+\hat{a} + \sigma^-\hat{a}^\dagger). \quad (2.12)$$

The Jaynes-Cummings Hamiltonian can be diagonalized in the basis of the dressed states [60, 61] that contain the number of photons in the resonator mode. In the experiments described in this thesis, we consider interactions of the ion with the cavity involving a single excitation. We therefore restrict the system to the states $|g, 0\rangle$, $|g, 1\rangle$ and $|e, 0\rangle$. The nontrivial eigenstates of this subspace are

$$\begin{aligned} |1, +\rangle &= \cos\vartheta |g, 1\rangle - \sin\vartheta |e, 0\rangle \\ |1, -\rangle &= \sin\vartheta |g, 1\rangle + \cos\vartheta |e, 0\rangle, \end{aligned} \quad (2.13)$$

where the mixing angle ϑ is given by

$$\tan 2\vartheta = \frac{2g}{\omega_c - \omega_0}. \quad (2.14)$$

If the resonator is resonant with the atom, i.e., $\omega_c = \omega_0$, the states $|g, 1\rangle$ and $|e, 0\rangle$ are degenerate. The coupling then mixes these states, resulting in the so-called vacuum-Rabi splitting [61] (fig. 2.2(b)). In this case, the eigenstates are $|1, \pm\rangle = \frac{1}{\sqrt{2}}(|g, 1\rangle \pm |e, 0\rangle)$, and the energy splitting is $2g$. If the system starts in one of the states $|g, 1\rangle$ or $|e, 0\rangle$ at time $t = 0$, it undergoes oscillations between these two states over time, corresponding to a periodic exchange of energy between the atom and the resonator.

2.2.1 Dissipation

So far, our model includes only the coupling between the atom and the mode of the resonator. In reality, however, both atom and cavity also couple to a reservoir of vacuum modes of the environment. Such coupling results in dissipative processes such as spontaneous emission of the atom and photon loss of the cavity. These dissipative processes are included in a master equation that is derived in the literature [62, 63] by treating the system as an open quantum system. If the interactions between the system and the reservoir are weak (Born approximation) and without memory, i.e., correlations between the system and the reservoir are short-lived compared to the timescale of system dynamics (Markov approximation), the master equation describing the time evolution of the system's density matrix ρ is given by [64]

$$\frac{d\rho}{dt} = \frac{-i}{\hbar} [\mathcal{H}, \rho] + \mathcal{L}_{\text{diss}}(\rho) \quad (2.15)$$

with $[\mathcal{H}, \rho] = \mathcal{H}\rho - \rho\mathcal{H}$. The Liouville super-operator $\mathcal{L}_{\text{diss}}$ can be written in the Lindblad form via collapse operators C_k [64], which take into account the coupling between the system and the reservoir:

$$\mathcal{L}_{\text{diss}}(\rho) = \frac{1}{2} \sum_k \left(2C_k\rho C_k^\dagger - \rho C_k^\dagger C_k - C_k^\dagger C_k\rho \right). \quad (2.16)$$

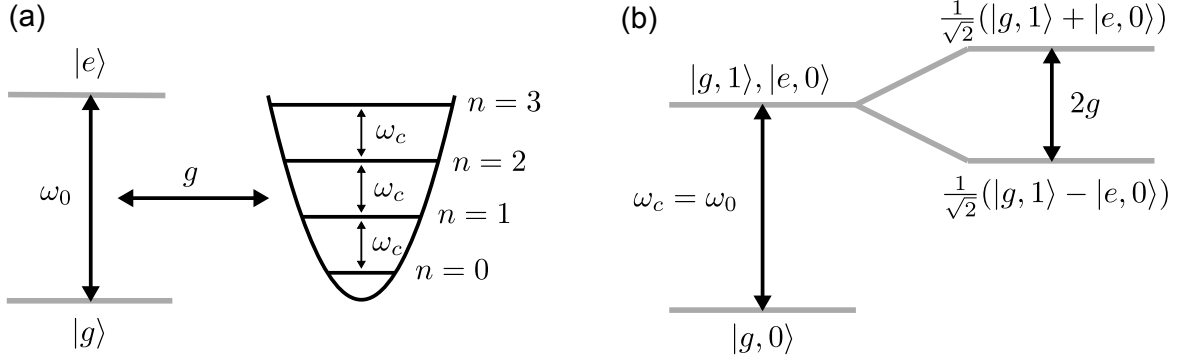


Figure 2.2: (a) Atom-cavity coupling. The atom is represented by a two-level system consisting of the ground state $|g\rangle$ and excited state $|e\rangle$ with energy splitting $\hbar\omega_0$. The atom couples with coupling strength g to the electromagnetic field of a single resonator mode which is represented by a harmonic oscillator at frequency ω_c . The composite system's Hilbert space is the tensor product of the individual spaces of atom and resonator. (b) Schematic energy level diagram of the combined atom-cavity system containing one or zero excitations. For resonant coupling, i.e., $\omega_c = \omega_a$, the coupling g mixes the degenerate states $|g, 1\rangle$ and $|e, 0\rangle$ equally. The new eigenstates are split in energy by $2g$.

In the master equation, the spontaneous emission of the atom can be introduced by the collapse operator $C_{\text{atom}} = \sqrt{2\gamma}\sigma$, where 2γ is the spontaneous emission rate of the atom. Its action on the subspace of the atom corresponds to both decay of the excited-state population and decay of coherences between the excited and ground state. Cavity-photon loss is introduced into the master equation by the collapse operator $C_{\text{cavity}} = \sqrt{2\kappa}\hat{a}$, where 2κ is the rate of photon decay of the resonator.

The system dynamics of the model including dissipation are determined by the parameters g, γ, κ and the atom-cavity detuning $\delta = \omega_a - \omega_c$. Three regimes are described in [65]. For $g \gg \gamma, \kappa, |\delta|$, the so-called *strong-coupling* regime, the system dynamics are dominated by the lossless oscillations of eq. (2.13). For $g \ll \gamma, \kappa, |\delta|$, the *weak-coupling* regime, the system dynamics are dominated by dissipation, and the coupling g no longer sets the relevant timescale. In this weak coupling regime, the system dynamics are dominated by photon loss from the cavity if $\kappa \gg \gamma, g$ (*bad cavity limit*) or by spontaneous emission of the atom if $\gamma \gg \kappa, g$ (*bad atom limit*).

In our experimental apparatus, we reach an intermediate coupling regime with $g \approx \gamma \gg \kappa$ on a dipole transition. Due to the level structure of the ion, the excited state $|e\rangle$, however, has an additional decay channel. Taking into account both decay channels, our system is placed in the bad-atom limit of the weak coupling regime as $\gamma \gg g \gg \kappa$. Instead of resonantly exciting the ion, we therefore apply a different technique in the experiment: a Raman transition involving three atomic levels in a Λ -type configuration. Of the two dipole transitions between the three levels, one is driven by the cavity and the other by a laser, as will be described in the next section.

2.3 Three-level system: vacuum-stimulated Raman transitions

Raman transitions constitute an important concept of atomic physics and optics that enables the coherent generation of single photons in the resonator, even in the absence of the strong coupling regime. In order to model the cavity-driven Raman transitions described in this thesis, at least a third atomic level has to be added to the system. We therefore first extend the model of sec. 2.2 to a three-level system in a Λ -type configuration. We then show that this three-level system can be simplified to an effective two-level system that manifests a tunable coupling and thus describes the experimental situation more appropriately than the previous two-level approach.

To describe the ion-photon entanglement and state mapping measurements, the three-level model will be further extended to a four-level system driven by a bichromatic field for the description of ion-photon entanglement in sec. 8.6 and to a five-level system driven by a bichromatic field for the description of ion-photon state mapping in sec. 9.5.

2.3.1 Three-level system coupled to a cavity

We consider a three-level atom in a Λ -configuration, consisting of two ground states $|S\rangle$ and $|D\rangle$ and one excited state $|P\rangle$, as sketched in fig. 2.3(a). A drive laser with Rabi frequency Ω_l and angular frequency ω_l drives the $S - P$ transition, while the atom interacts with the resonator on the $P - D$ transition with coupling strength g . The Hamiltonian of the system contains three contributions

$$\mathcal{H} = \mathcal{H}_0 + \mathcal{H}_l + \mathcal{H}_c \quad (2.17)$$

with

$$\mathcal{H}_0 = E_S \hat{\sigma}_{SS} + E_D \hat{\sigma}_{DD} + E_P \hat{\sigma}_{PP} + \hbar\omega_c \hat{a}^\dagger \hat{a} \quad (\text{bare Hamiltonian}) \quad (2.18)$$

$$\mathcal{H}_l = \frac{\hbar\Omega_l}{2} (\hat{\sigma}_{SP} e^{i\omega_l t} + \hat{\sigma}_{PS} e^{-i\omega_l t}) \quad (\text{atom-laser interaction}) \quad (2.19)$$

$$\mathcal{H}_c = \hbar g (\hat{a}^\dagger \hat{\sigma}_{DP} + \hat{\sigma}_{PD} \hat{a}) \quad (\text{atom-cavity interaction}). \quad (2.20)$$

The bare Hamiltonian \mathcal{H}_0 with $\hat{\sigma}_{SS} = |S\rangle\langle S|$ ($\hat{\sigma}_{PP}, \hat{\sigma}_{DD}$ similarly) contains the energy of the bare atomic levels S, P, D given by E_S, E_P, E_D and the energy of cavity photons $\hbar\omega_c$. In the atom-laser interaction \mathcal{H}_l , the laser field is approximated by a coherent state with large amplitude, which remains unperturbed by the absorption or emission of single photons by the atom [66]. Ω_l is the Rabi frequency of the laser field, and the atomic raising and lowering operators are now defined as $\hat{\sigma}_{SP} = |S\rangle\langle P|$, $\hat{\sigma}_{PS}^\dagger = \hat{\sigma}_{PS} = |P\rangle\langle S|$ and $\hat{\sigma}_{DP} = |D\rangle\langle P|$, $\hat{\sigma}_{PD}^\dagger = \hat{\sigma}_{PD} = |P\rangle\langle D|$. The Jaynes-Cummings-type interaction of the cavity with the atomic $P - D$ transition in \mathcal{H}_c is analogous to the two-level interaction of sec. 2.2.

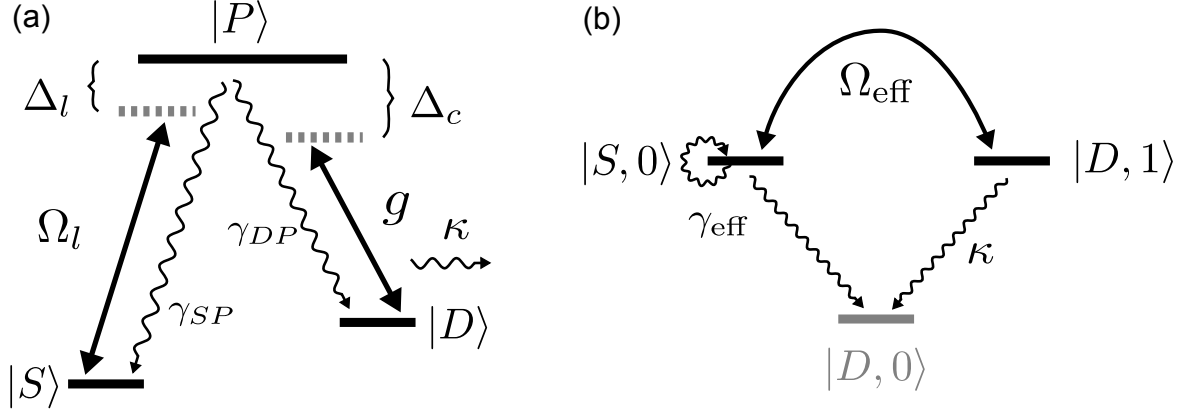


Figure 2.3: (a) Three-level system in a Λ -type configuration. A laser with Rabi frequency Ω_l couples the states $|S\rangle$ and $|P\rangle$ with detuning Δ_l , while the cavity couples $|P\rangle$ and $|D\rangle$ with vacuum-Rabi frequency $2g$ and detuning Δ_c . $|P\rangle$ spontaneously decays to $|S\rangle$ and $|D\rangle$ at rates $2\gamma_{SP}$ and $2\gamma_{DP}$, respectively. Cavity decay is denoted by κ . (b) Effective two-level system. The Raman process couples $|S, 0\rangle$ to $|D, 1\rangle$ (where 0 and 1 denote the number of photons in the cavity) at the effective Raman-Rabi frequency Ω_{eff} . Spontaneous emission of the atom γ_{eff} leads to dephasing and decay to the uncoupled state $|D, 0\rangle$.

2.3.2 Raman interaction picture

We can remove the time dependence of the atom-laser interaction term 2.19 in H by performing a unitary transformation \hat{U} (interaction picture). If \hat{U} maps a state $|\psi\rangle$ of the system to the new state $|\psi'\rangle = \hat{U}|\psi\rangle$, the Hamiltonian transforms into $\mathcal{H} = \hat{U}H\hat{U}^\dagger - i\hbar\hat{U}\frac{d\hat{U}^\dagger}{dt}$. For the Hamiltonian of eq. (2.17), a suitable unitary transformation is given by

$$\hat{U} = e^{i\hat{\sigma}_{SS}\omega_l t}. \quad (2.21)$$

Additionally, we can set the energy reference of the atom to the P level, i.e., subtract E_P from the energy of all states. In the new basis, the Hamiltonian is now given by

$$\mathcal{H}_0 = \hbar\Delta_l\hat{\sigma}_{SS} + (E_D - E_P)\hat{\sigma}_{DD} + \hbar\omega_c\hat{a}^\dagger\hat{a} \quad (2.22)$$

$$\mathcal{H}_l = \frac{\hbar\Omega_l}{2}(\hat{\sigma}_{SP} + \hat{\sigma}_{PS}) \quad (2.23)$$

$$\mathcal{H}_c = \hbar g(\hat{a}^\dagger\hat{\sigma}_{DP} + \hat{\sigma}_{PD}\hat{a}), \quad (2.24)$$

where $\Delta_l = (E_S - E_P)/\hbar - \omega_l$ is the detuning between the laser and the $S - P$ transition.

2.3.3 Effective two-level system

If the detuning of the drive laser Δ_l from the $S - P$ transition matches the detuning of the cavity $\Delta_c = \omega_c - (E_P - E_D)/\hbar$ from the $P - D$ transition, population is

directly transferred between the S and D states. This Raman resonance dominates the system dynamics if the excitation of the P state is suppressed, i.e., if the detunings $\Delta_c, \Delta_l \gg \Omega_l, g, \gamma_P$ (with $\gamma_P = \gamma_{DP} + \gamma_{SP}$ including the decay of P to both S and D). Under these conditions, the excited P state can be adiabatically eliminated [67–70] by performing a second unitary transformation. This calculation is carried out in [65]. Here, we summarize the result for a model that includes one drive laser. By applying the transformation $\hat{U} = e^{\hat{S}}$ [68, 69] with

$$\hat{S} = \frac{\Omega_l}{2\Delta_l}(\hat{\sigma}_{SP} - \hat{\sigma}_{PS}) + \frac{g}{\Delta_c}(\hat{a}^\dagger \hat{\sigma}_{DP} + \hat{\sigma}_{PD} \hat{a}), \quad (2.25)$$

expanding the transformed Hamiltonian $\mathcal{H}' = \hat{U}\mathcal{H}\hat{U}^\dagger$ in a power series in $1/\Delta_l$ and $1/\Delta_c$, and keeping only the first order terms, one obtains [65]: $\mathcal{H}' = \mathcal{H}'_0 + \mathcal{H}'_{\text{Raman}} + \mathcal{H}'_{\text{AC-Stark shift}}$ with

$$\mathcal{H}'_0 = \mathcal{H}_0 = \Delta_l \hat{\sigma}_{SS} + (E_D - E_P) \hat{\sigma}_{DD} + \hbar\omega_c \hat{a}^\dagger \hat{a} \quad (2.26)$$

$$\mathcal{H}'_{\text{Raman}} = \frac{\hbar g \Omega_l}{4} \left(\frac{1}{\Delta_l} + \frac{1}{\Delta_c} \right) (\hat{a}^\dagger \hat{\sigma}_{SD} + \hat{\sigma}_{DS} \hat{a}) \quad (2.27)$$

$$\mathcal{H}'_{\text{AC-Stark shift}} = \frac{\hbar \Omega_l^2}{2\Delta_l} (\hat{\sigma}_{SS} - \hat{\sigma}_{PP}) + \frac{\hbar g^2}{\Delta_c} (\hat{a}^\dagger \hat{a} (\hat{\sigma}_{DD} - \hat{\sigma}_{PP}) - \hat{\sigma}_{PP}). \quad (2.28)$$

While \mathcal{H}_0 remains unchanged by this transformation, the interaction term now exhibits a Raman coupling $\mathcal{H}'_{\text{Raman}}$ between the S and D states. This coherent coupling describes the population transfer from $|S, 0\rangle$ to $|D, 1\rangle$ (where 0 and 1 denote the number of photons in the cavity) during which one photon from the laser is absorbed and one photon is emitted into the resonator (fig. 2.3b). At Raman resonance, the detuning of the drive laser equals the detuning of the resonator $\Delta_l = \Delta_c = \Delta$, and the Rabi frequency of the Raman coupling simplifies to $\Omega_{\text{eff}} = \frac{\hbar g \Omega_l}{2\Delta}$. The energy shift of the S and P levels due to the fields of the drive laser and the cavity, described by $\mathcal{H}'_{\text{AC-Stark shift}}$, will be important for the consideration of the state-mapping scheme in chapter 9.

2.3.4 Comparison to Raman transitions driven by two lasers

One important result of the previous section is the effective Raman-Rabi frequency at Raman resonance

$$\Omega_{\text{eff}} = \frac{g \Omega_l}{2\Delta}. \quad (2.29)$$

In our model for a three-level system, dissipation has so far been neglected. In our experiment, the dominant dissipation channel is decay from the P state, which is off-resonantly excited by the drive laser. The rate γ_{eff} of such spontaneous decay can be approximated [65] in the limit $\Delta \gg \Omega_l, \gamma_P$ by

$$\gamma_{\text{eff}} \approx \left(\frac{\Omega_l}{2\Delta} \right)^2 \gamma_P. \quad (2.30)$$

In order to estimate how much this off-resonant scattering influences the coherence of the Raman transfer, we calculate the ratio of the coherent Raman coupling rate to the off-resonant scattering rate. Using the parameters of our experimental apparatus, we typically reach $\Omega_{\text{eff}}/\gamma_{\text{eff}} = 1 - 5$ for drive-laser Rabi frequencies of 20 – 100 MHz. In contrast, for a direct excitation of the P state, the ratio would be $g/\gamma_P = 0.1$. The Raman process thus increases this ratio by more than one order of magnitude.

Compared to a Raman process driven by two lasers, however, the cavity-driven Raman process is limited to a maximum detuning. For a comparison, we first consider the case in which both $S-P$ and $P-D$ transitions are driven by a laser, with which the reader might be more familiar. Here, the atom-cavity coupling g is replaced with the Rabi frequency of the second laser Ω_{l_2} (for convenience, we now define $\Omega_{l_1} = \Omega_l$) that is tuned to Raman resonance $\Delta_{l_1} = \Delta_{l_2} = \Delta$. The effective Raman-Rabi frequency is now $\Omega_{\text{eff}} = \frac{\Omega_{l_1}\Omega_{l_2}}{2\Delta}$ and the ratio of effective coupling to scattering can be approximated by

$$\frac{\Omega_{\text{eff}}}{\gamma_{\text{eff}}} = \frac{2\Delta\Omega_{l_2}}{\gamma_P\Omega_{l_1}} \approx \frac{2\Delta}{\gamma} \quad (\text{two-laser Raman transition}) \quad (2.31)$$

if the Rabi frequencies of the two lasers $\Omega_{l_1} \approx \Omega_{l_2}$ are approximately equal. By increasing the detuning Δ of both lasers from the excited state, one can therefore decrease the effect of off-resonant scattering. The Raman-Rabi frequency can be maintained at a constant value via simultaneously increasing the Rabi frequencies Ω_{l_1} and Ω_{l_2} of the lasers.

For the cavity-driven Raman transition, the situation is different. The ratio of coherent to incoherent coupling is

$$\frac{\Omega_{\text{eff}}}{\gamma_{\text{eff}}} = \frac{g\Delta}{\gamma_P\Omega_l} = \frac{g^2}{\gamma\Omega_{\text{eff}}} \quad (\text{cavity-laser Raman transition}), \quad (2.32)$$

where we have rewritten the ratio as a function of Ω_{eff} itself. From eq. (2.32), it is apparent that off-resonant scattering is attenuated by increasing the detuning or decreasing the Rabi frequency Ω_l of the drive laser. As only the Rabi frequency Ω_l can be increased but not the atom-cavity coupling g , the Raman-Rabi frequency Ω_{eff} decreases at the same time. In a realistic experimental environment, the coherence of the Raman process will at some stage be limited by the atomic coherence time or dark counts of the photon detectors.

In conclusion, the Raman transfer allows us to move from a weakly coupled regime into a regime where the coherent rate Ω_{eff} is larger than the decoherent rates $\gamma_{\text{eff}}, \kappa$. However, while the theoretical description of a three-level system serves well to investigate the fundamental properties of the Raman transfer, it has to be further extended to describe the complex dynamics of the real atom. In the next chapter, we therefore introduce a more realistic model.

3 States and transitions in $^{40}\text{Ca}^+$ for an ion-photon interface

While the previous chapter modeled the atom-cavity interaction in the simplest possible way, i.e., via an idealized two- or three-level system, this chapter introduces the level scheme of a trapped $^{40}\text{Ca}^+$ ion that serves as the atomic qubit in our experiment. After an introduction to the various transitions employed for laser cooling, state manipulation and detection, we discuss a range of atomic states that can constitute an atomic qubit and the possible transitions for coupling to an optical resonator. After choosing appropriate states and transitions for qubit and cavity, we construct a realistic theoretical model based on the master equation formalism that serves to describe our experimental findings. This model contains all eighteen atomic levels, two orthogonally polarized cavity modes, external laser fields and dissipation channels.

3.1 Trapped calcium ions as quantum bits

Ion traps combine long storage times with an excellent isolation of the ions from the environment. Single-charged alkaline earth ions offer relatively simple electronic level structures in which laser cooling can be realized by driving one strong dipole transition with additional repumping on a weaker dipole transition. For the realization of a qubit, two states have to be identified that have long lifetimes and long coherence times compared to any gate operation time [18] such that spontaneous decay and coupling to the environment can be neglected on the timescale of an experiment. In alkaline earth ions, (a range of) pairs of states have been proven to fulfill this requirement: the ground state and a long-lived metastable state [42], two electronic spin states of the ground state [71, 72], or two hyperfine ground states of an atomic species possessing nuclear spin [73, 74].

In this work, we use a single $^{40}\text{Ca}^+$ ion. A simplified level scheme of $^{40}\text{Ca}^+$ consisting of the lowest five angular momentum state manifolds is sketched in fig. 3.1. In this thesis, we will use the abbreviated notation $|L_J, m_J\rangle$ in order to specify the Zeeman substate with magnetic quantum number m_J of the state manifold $^{2S+1}L_J$ with orbital angular momentum L , spin S , and total angular momentum quantum number J .

For efficient Doppler cooling, we drive the dipole transition between the $S_{1/2}$ ground state and the $P_{1/2}$ excited-state with a linewidth of $\Gamma_{P_{1/2}-S_{1/2}} = (2\pi) \times 20.7$ MHz via a laser at 397 nm. As the excited $P_{1/2}$ state also decays with a branching ratio of 1/12 to the metastable $D_{3/2}$ state, we additionally apply a repumping beam at 866 nm that drives any $D_{3/2}$ state population back to the $P_{1/2}$ state. The second metastable $D_{5/2}$

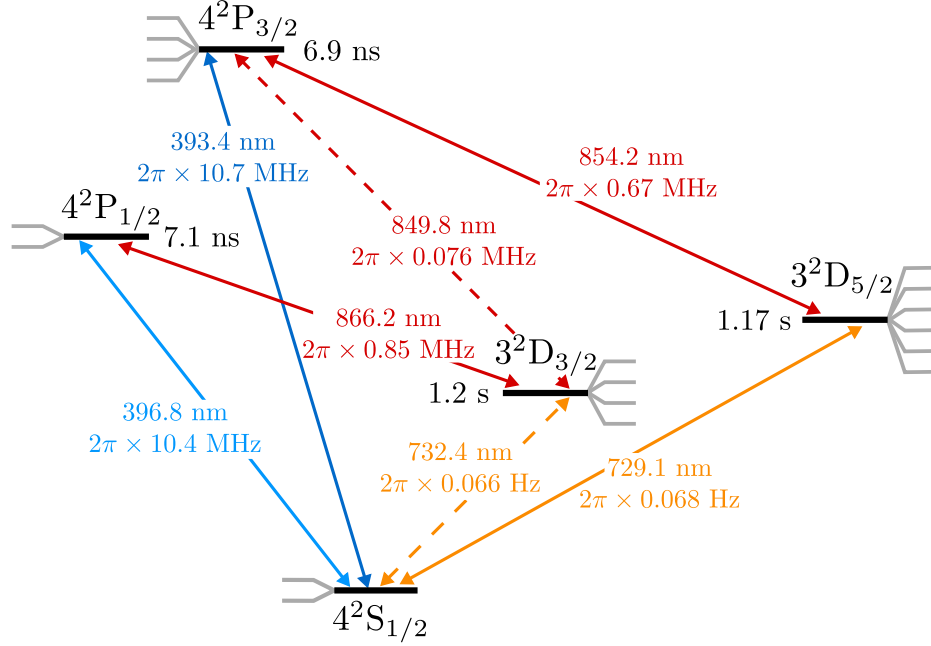


Figure 3.1: Simplified level scheme of $^{40}\text{Ca}^+$ with state lifetimes and transition wavelengths in air taken from [76–78]. The lowest three angular-momentum state manifolds, ground-state manifold $S_{1/2}$, excited-state manifolds $P_{1/2}$ and $P_{3/2}$, and metastable manifolds $D_{3/2}$ and $D_{5/2}$, split into the Zeeman sub-levels indicated. Doppler cooling and state detection via the fluorescence method are provided on the $S_{1/2} \leftrightarrow P_{1/2}$ dipole transition at 397 nm with additional repumping on the $P_{1/2} \leftrightarrow D_{3/2}$ transition at 866 nm. The $S_{1/2} \leftrightarrow D_{5/2}$ quadrupole transition at 729 nm is driven for coherent manipulation of the atomic qubit. In order to re-initialize the qubit in the $S_{1/2}$ ground state, we repump any population of the $D_{5/2}$ qubit state to the $P_{3/2}$ state via a laser at 854 nm. The cavity is tuned into resonance with the transition at 854 nm. We drive the 393 nm transition in order to generate photons in the cavity via a $S_{1/2} \leftrightarrow P_{3/2} \leftrightarrow D_{5/2}$ Raman process. For comparison with the ion-cavity coupling g and the cavity decay κ , the width of each transition is given as a half-width $\gamma = \Gamma/2$, calculated from the branching ratios of [78, 79].

state, however, remains uncoupled from this cooling cycle and therefore represents an ideal qubit in combination with the ground $S_{1/2}$ state. The $S_{1/2} \leftrightarrow D_{5/2}$ quadrupole transition at 729 nm is driven with a narrow-linewidth laser to control the qubit’s state, while we apply the 397 nm and 866 nm cooling lasers as during the cooling cycle to discriminate between the two qubit states [75]. If the ion is initially in the $S_{1/2}$ state, it will exhibit fluorescence that is detected by a PMT or a CCD camera. If the ion initially is in the $D_{5/2}$ state, however, it will remain uncoupled from the lasers at 397 nm and 866 nm and no fluorescence will be measured.

3.1.1 Zeeman structure

In order to lift the degeneracy of the energy levels, a small magnetic field of magnitude B is applied. As indicated in fig. 3.1, each manifold with total angular-momentum quantum number J is split into $2J + 1$ Zeeman substates m_J with energy shift

$$\Delta E_{J,m_J} = \hbar m_J g_J \mu_B B, \quad (3.1)$$

where $\mu_B = 9.3 \cdot 10^{-24}$ J/T ≈ 1.4 MHz/G is the Bohr magneton and g_J is the Landé factor of level ${}^{2S+1}L_J$. The Landé factor is calculated via $g_J = 3/2 + [S(S+1) - L(L+1)]/[2J(J+1)]$, corresponding to $g_{S_{1/2}} = 2, g_{P_{1/2}} = 2/3, g_{P_{3/2}} = 4/3, g_{D_{3/2}} = 4/5, g_{D_{5/2}} = 6/5$.

In the experimental apparatus, the magnitude of the magnetic field is chosen such that states of the $S_{1/2}$ and the $D_{5/2}$ manifolds are well resolved in frequency. As a result, substates of the $S_{1/2} \leftrightarrow D_{5/2}$ quadrupole transition at 729 nm and the cavity-driven Raman transition between $S_{1/2} \leftrightarrow P_{3/2} \leftrightarrow D_{5/2}$ can be addressed in a frequency-selective manner. The frequency splitting of these transitions is given by

$$\Delta \nu_{S_{1/2},m_J \leftrightarrow D_{5/2},m'_J} = -\mu_B B (g_{D_{5/2}} m_J - g_{S_{1/2}} m'_J). \quad (3.2)$$

In our setup, we apply a magnetic field between 3 and 5 G, resulting in frequency splittings of a few MHz.

3.1.2 Qubits for an ion-photon interface

If we employ the $S_{1/2}$ - $D_{5/2}$ quadrupole transition for coherent manipulation of the atomic state, a qubit can be encoded in any pair of Zeeman substates of the $S_{1/2}$ and $D_{5/2}$ manifolds. Typically, the states $|S_{1/2}, \pm \frac{1}{2}\rangle$ and $|D_{5/2}, \pm \frac{1}{2}\rangle$ are used to define an *optical qubit* as these pairs are the least sensitive to magnetic field noise. However, for the ion-photon quantum interface protocols realized in this thesis, a *spin qubit*, defined by two Zeeman substates of the same state manifold, constitutes a more convenient choice. Optical and spin qubits can be converted into each other via coherent pulses at 729 nm.

For the ion-photon entanglement described in chapter 8, the atomic qubit consists of the $|D_{5/2}, -\frac{5}{2}\rangle$ and $|D_{5/2}, -\frac{3}{2}\rangle$ states. A single π -pulse transfers this *spin qubit* to an *optical qubit* for state detection. For state mapping (chapter 9), the atomic qubit is defined by the spin qubit consisting of the $|S_{1/2}, +\frac{1}{2}\rangle$ and $|S_{1/2}, -\frac{1}{2}\rangle$ states.

3.2 Transitions for generating single photons

Coupling one of the atomic transitions to the mode of an optical resonator is advantageous both for the efficient generation of single photons and for a reversible state-mapping process between atom and photon [41]. Given the level structure of ${}^{40}\text{Ca}^+$,

a resonator could be coupled either to one of the dipole transitions, $S \leftrightarrow P$ or $P \leftrightarrow D$, or to the quadrupole-allowed transitions, $S \leftrightarrow D$. The strongest absolute coupling would be achieved by using the $S \leftrightarrow P$ transitions, at 397 or 393 nm, due to matrix elements (Einstein coefficients) and the vacuum mode density, which is proportional to the square of the frequency. Technically, however, engineering highly reflective mirror coatings at ultraviolet wavelengths is challenging. On one of the $S \leftrightarrow D$ transitions, a resonator has been coupled to a single ion with a rate $g = 2\pi \times 134$ Hz, three orders of magnitude larger than the atomic decay rate $\gamma_{\text{SD}} = 2\pi \times 0.07$ Hz [47]. Nevertheless, for quantum processes on these timescales, the coherence of the ion-cavity coupling would be obscured by technical imperfections such as magnetic field fluctuations and laser instability, as discussed in sec. 5.7. In contrast, two of the $P \leftrightarrow D$ transitions offer both a strong transition strength ($\gamma_{\text{PD}} \sim 1$ MHz) and a wavelength ($\lambda = 866$ nm, 854 nm) at which ultra-low-loss mirror coatings are possible. These transitions thus emerge as the most attractive for an atom-photon interface. In contrast to Refs. [46, 48], by using the $D_{5/2}$ rather than the $D_{3/2}$ manifold, we can take advantage of the tools for initialization, coherent manipulation and state detection of the atom described in chapter 5.

3.3 Model: Eighteen-level system coupled to two cavity modes

For simplicity, the atom has been treated up to this point as an idealized two- or three-level system in order to study the fundamental concept of the atom-cavity interaction. In this section, we introduce a more realistic theoretical model that describes the experimental results achieved with a single $^{40}\text{Ca}^+$ ion coupled to two polarization modes of the cavity. Our theoretical model is based on the master equation formalism and allows for a numerical simulation of the system dynamics.

A simpler, realistic model has been derived for an eight-level system in [65]. For a simulation of the measurements presented in this thesis, the current model includes an eighteen-level system coupled to two orthogonally polarized cavity modes. The simulations, originally written by Carlos Russo, have been rewritten as part of this thesis work, with assistance of Tracy Northup, and now include a bichromatic drive field at the $S_{1/2} \leftrightarrow P_{3/2}$ transition and the two cavity modes coupling to the $P_{3/2} \leftrightarrow D_{5/2}$ transition.

In this section, we describe the individual terms of the system's Hamiltonian after a short introduction to the atom-light interaction in the dipole approximation.

3.3.1 Electric dipole interaction

The first term in the Taylor expansion of the interaction between an atom and the electromagnetic field corresponds to the electric dipole interaction [80]:

$$\mathcal{H}_{\text{int}} = -\vec{d} \cdot \vec{E}, \quad (3.3)$$

with $\vec{d} = e\vec{r}$ the atomic dipole moment. As the electron coordinates \vec{r} have odd parity, the transition matrix element $\langle \psi_b | -e\vec{r} \cdot \vec{E} | \psi_a \rangle$ is non-zero if the wave-functions $|\psi_a\rangle$ of the initial state and $|\psi_b\rangle$ of the final state have opposite parity. As this holds true for all transitions involved in the $S_{1/2} \leftrightarrow P_{3/2} \leftrightarrow D_{5/2}$ Raman process, these transitions are described by the electric dipole approximation.

Writing the dipole operator in spherical coordinates $\vec{d} = \sum_{q=0,\pm 1} d_q \hat{e}_q$ with $\hat{e}_0 = \hat{e}_z, \hat{e}_{\pm 1} = \frac{1}{\sqrt{2}}(\hat{e}_x \pm i\hat{e}_y)$, the transition matrix element between initial state $|J_a, m_a\rangle$ and final state $|J_b, m_b\rangle$ can be written as a product of the reduced matrix element and a Clebsch-Gordon coefficient [81]:

$$\langle J_b, m_b | d_q | J_a, m_a \rangle = \mu_{A,B} \cdot \langle J_a, 1; m_a, q | J_b, m_b \rangle. \quad (3.4)$$

The reduced dipole moment $\mu_{A,B}$ is independent of the geometry, i.e., the quantum numbers m_a, m_b . It is related to the lifetime $\tau_{A,B}$ of the transition between manifolds A and B via [80]

$$\frac{1}{\tau_{A,B}} = 2\gamma_{A,B} = \frac{8\pi^2}{3\epsilon_0 \hbar \lambda^3} |\mu_{A,B}|^2. \quad (3.5)$$

The Clebsch-Gordon coefficients $\langle J_a, 1; m_a, q | J_b, m_b \rangle$ describe the geometric component of the transition amplitudes between individual Zeeman substates. They can be interpreted as the coupling of the state $|J_a, 1; m_a, q\rangle$ with a photon with angular momentum 1 and polarization $q = 0, \pm 1$ (linear and circular polarizations) to the state $|J_b, m_b\rangle$. The Clebsch-Gordon coefficients are given by [81]

$$\begin{aligned} \langle J_a, 1; m_a, q | J_b, m_b \rangle &= (-1)^{2(J_a+m_b)} \\ &\cdot \sqrt{\frac{2(2J_a)! (J_b - m_b)! (J_b + m_b)!}{(2J_b)! (J_a - m_a)! (J_a + m_a)! (m_a - m_b + 1)! (m_b - m_a + 1)!}} \end{aligned} \quad (3.6)$$

and are indicated in fig. 3.2 for the $S_{1/2} \leftrightarrow P_{3/2}$ and $P_{3/2} \leftrightarrow D_{5/2}$ transitions available for cavity-driven Raman transitions.

3.3.2 Hamiltonian

For clarity, the total Hamiltonian describing the ion-cavity system is divided into three parts: the bare-ion Hamiltonian \mathcal{H}_0 , the ion-laser interaction $\mathcal{H}_{\text{ion-laser}}$, and the ion-cavity interaction $\mathcal{H}_{\text{ion-cavity}}$:

$$\mathcal{H} = \mathcal{H}_0 + \mathcal{H}_{\text{ion-laser}} + \mathcal{H}_{\text{ion-cavity}} \quad (3.7)$$

Hamiltonian for the bare ion and bare cavity

The bare-ion, bare-cavity Hamiltonian can be decomposed into a number of terms, one for each atomic manifold L_J and both cavity modes $c = a, b$:

$$\mathcal{H}_0 = \mathcal{H}_{0,S_{1/2}} + \mathcal{H}_{0,P_{3/2}} + \mathcal{H}_{0,P_{1/2}} + \mathcal{H}_{0,D_{5/2}} + \mathcal{H}_{0,D_{3/2}} + \mathcal{H}_{0,a} + \mathcal{H}_{0,b}. \quad (3.8a)$$

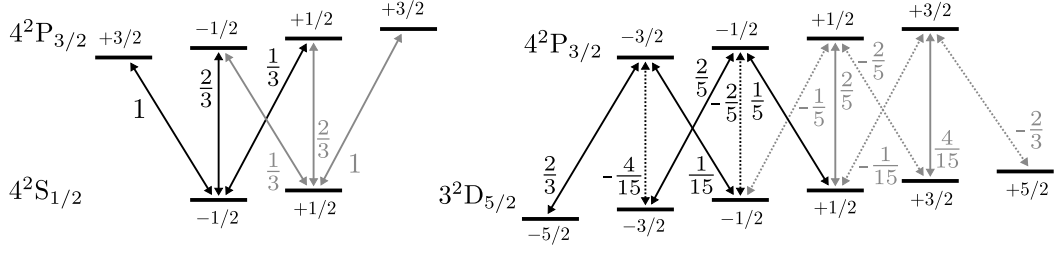


Figure 3.2: Clebsch-Gordan coefficients for the $S_{1/2} \leftrightarrow P_{3/2}$ and $P_{3/2} \leftrightarrow D_{5/2}$ transitions. Square-root signs are omitted for clarity. The coefficient for the $|P_{3/2}, -3/2\rangle$ to $|D_{5/2}, -3/2\rangle$, e.g., is $-\sqrt{4/15}$. Dotted lines indicate negative coefficients.

The transformation to the interaction picture rotates each subspace at the laser frequency of the corresponding dipole transition as in eq. (2.21). In the interaction picture, the energy of the atomic states is then given by the laser detunings Δ_{l,L_J} and the Zeeman shift:

$$\mathcal{H}_{0,L_J} = \sum_{m_J=-J}^{+J} \hbar(\Delta_{l,L_J} + m_J g_J \mu_B B) \hat{\sigma}_{L_J, m_J}^{L'_J, m'_J} \quad (3.8b)$$

$$\mathcal{H}_{0,c} = \sum_{c=a}^b \hbar(\Delta_c - \Delta_{l_i})(\hat{a}^\dagger \hat{a} + \hat{b}^\dagger \hat{b}) \quad (3.8c)$$

where $\hat{\sigma}_{L_J, m_J}^{L'_J, m'_J}$ is the projector corresponding to the transition from $|L_J, m_J\rangle$ to $|L'_J, m'_J\rangle$. Of great importance for the entanglement and state-mapping experiments is the fact that the two cavity modes differ in polarization but are degenerate in energy. Their common detuning from the $P_{3/2} \leftrightarrow D_{5/2}$ transition is denoted by $\Delta_c = \Delta_a = \Delta_b$.

Ion-laser interaction Hamiltonian

The Hamiltonian for the ion-laser interaction can be decomposed into three parts:

$$\mathcal{H}_{\text{ion-laser}} = \mathcal{H}_{\text{ion-laser}, SP} + \mathcal{H}_{\text{ion-laser}, DP}^{(1)} + \mathcal{H}_{\text{ion-laser}, DP}^{(2)}, \quad (3.9a)$$

where the repump transition $P_{1/2} \leftrightarrow D_{3/2}$ is labelled (1), and $P_{3/2} \leftrightarrow D_{5/2}$ is labelled (2). The laser fields can be treated in the semi-classical approximation where the field operator is replaced with its expectation value, as the absorption or emission of single photons by the atom does not change the state of the laser field [66]. Additionally neglecting motion of the ion, i.e., setting $\vec{k} \cdot \vec{r} = 0$ for $\delta r \ll \lambda$, the laser field can be approximated as $\hbar\Omega_0 \vec{e} \cos(\omega t)$ with Rabi frequency $\Omega_0 = \mu_{A,B} E_0 / \hbar$ and polarization \vec{e} . In the interaction picture, both ion-laser interactions of the repump lasers $\Omega_{\text{rep}}^{(1)}$ at the $P_{3/2} \leftrightarrow D_{5/2}$ and transitions $\Omega_{\text{rep}}^{(2)}$ at the $P_{1/2} \leftrightarrow D_{3/2}$ transitions are time-independent as the subspace of the manifolds $D_{5/2}$ and $D_{3/2}$ are transformed

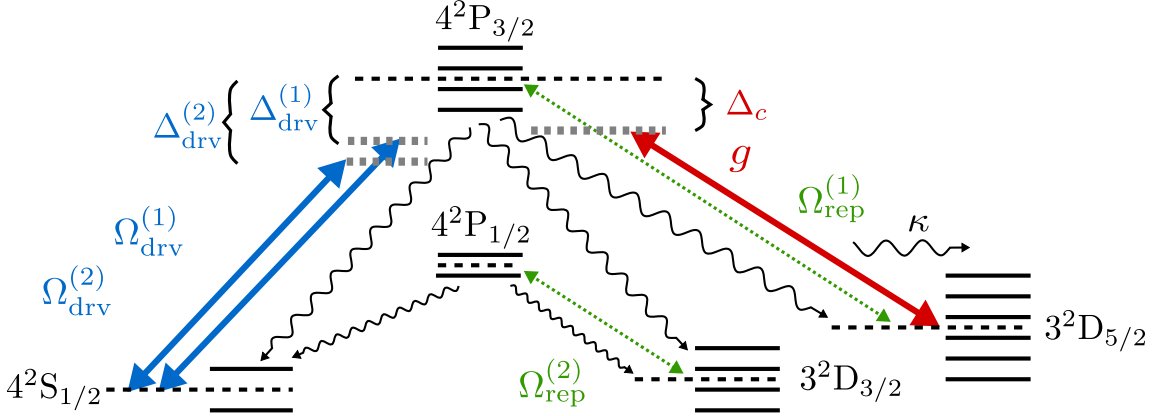


Figure 3.3: Eighteen-level system as implemented in the theoretical model of $^{40}\text{Ca}^+$. Indicated are the most important couplings and decay channels.

individually by the unitary transformations $e^{i|D_{5/2}\rangle\langle D_{5/2}|\omega_{\text{rep}}^{(1)}t}$ and $e^{i|D_{3/2}\rangle\langle D_{3/2}|\omega_{\text{rep}}^{(2)}t}$, respectively. For the bichromatic drive field in $\mathcal{H}_{\text{ion-laser},SP}$, which is applied for the ion-photon entanglement and state mapping, the situation is different. Here, both fields address the same transition at different laser frequencies $\omega_{\text{drv}}^{(1,2)}$. We choose the transformation $e^{i|S_{1/2}\rangle\langle S_{1/2}|\omega_{\text{drv}}^{(1)}t}$, which results in a time-dependent coupling term of the second field. The three components of eq. (3.9a) then read:

$$\mathcal{H}_{\text{ion-laser},SP} = \frac{\hbar(\Omega_{\text{drv}}^{(1)} + \Omega_{\text{drv}}^{(2)} e^{i(\omega_{\text{drv}}^{(2)} - \omega_{\text{drv}}^{(1)})t})}{2} \sum_{m_S = -\frac{1}{2}}^{\frac{1}{2}} \sum_{m_P = -\frac{3}{2}}^{\frac{3}{2}} \left[\vec{\epsilon}_{\text{drv}} \cdot \vec{d}_{S_{1/2},m_S}^{P_{3/2},m_P} \hat{\sigma}_{P,m_P}^{S,m_S} + h.c. \right] \quad (3.9b)$$

$$\mathcal{H}_{\text{ion-laser},DP}^{(1)} = \frac{\hbar\Omega_{\text{rep}}^{(1)}}{2} \sum_{m_D = -\frac{5}{2}}^{\frac{5}{2}} \sum_{m_P = -\frac{3}{2}}^{\frac{3}{2}} \left[\vec{\epsilon}_{\text{rep}}^{(1)} \cdot \vec{d}_{D_{5/2},m_D}^{P_{3/2},m_P} \hat{\sigma}_{P_{3/2},m_P}^{D_{5/2},m_D} + h.c. \right] \quad (3.9c)$$

$$\mathcal{H}_{\text{ion-laser},DP}^{(2)} = \frac{\hbar\Omega_{\text{rep}}^{(2)}}{2} \sum_{m_D = -\frac{3}{2}}^{\frac{3}{2}} \sum_{m_P = -\frac{1}{2}}^{\frac{1}{2}} \left[\vec{\epsilon}_{\text{rep}}^{(2)} \cdot \vec{d}_{D_{3/2},m_D}^{P_{1/2},m_P} \hat{\sigma}_{P_{1/2},m_P}^{D_{3/2},m_D} + h.c. \right]. \quad (3.9d)$$

Here, the atomic dipole vectors are written in spherical coordinates:

$$\vec{d}_{L_J,m_J}^{L'_J,m'_J} = \langle J, 1; m_J, q | J', m'_J \rangle \cdot \begin{cases} \vec{\epsilon}_- & \text{for } m'_J = m_J - 1 \\ \vec{\epsilon}_0 & \text{for } m'_J = m_J \\ \vec{\epsilon}_+ & \text{for } m'_J = m_J + 1. \end{cases} \quad (3.10)$$

Fig. 3.3 illustrates the individual terms of the coupled eighteen-level system.

Ion-cavity interaction Hamiltonian

The standing wave field inside the Fabry-Perot resonator with polarization $\vec{\epsilon}$ can be written as

$$\hat{E}_{\text{cavity}}(\vec{k}, \vec{r}) = \sqrt{\frac{\hbar\omega}{2\epsilon_0 V}} \vec{\epsilon} \cos(\vec{k} \cdot \vec{r}) (\hat{a}e^{-i\omega ct} + \hat{a}^\dagger e^{i\omega ct}). \quad (3.11)$$

For a resonator of length L and waist w_0 , the mode volume is given by $V = Lw_0^2\pi/4$. In the dipole approximation, the coupling constant $g_0^{(A,B)}$ between ion and resonator field on the transition A, B then is

$$g_0^{(A,B)} = \frac{\mu_{A,B}}{\hbar} \sqrt{\frac{2\hbar\omega}{\epsilon_0 Lw_0^2\pi}} = \sqrt{\frac{3c\gamma_{A,B}\lambda^2}{Lw_0^2\pi^2}}. \quad (3.12)$$

As the cavity supports two orthogonal polarization modes, the ion-cavity interaction Hamiltonian contains the coupling of both degenerate modes with annihilation operators \hat{a} and \hat{b} :

$$\mathcal{H}_{\text{ion-cavity}} = \hbar g_0^{(D_{5/2}, P_{3/2})} \sum_{m_D=-\frac{5}{2}}^{\frac{5}{2}} \sum_{m_P=-\frac{3}{2}}^{\frac{3}{2}} \left[(\hat{a}\vec{\epsilon}_a + \hat{b}\vec{\epsilon}_b) \cdot \vec{d}_{D_{5/2}, m_D}^{P_{3/2}, m_P} \hat{\sigma}_{P_{3/2}, m_P}^{D_{5/2}, m_D} + h.c. \right], \quad (3.13)$$

where we again neglect the motion of the ion and assign the maximum coupling strength to both modes.

3.3.3 Dissipation

In addition to the Hermitian terms, dissipation is added to the system via collapse operators as introduced in sec. 2.2.1 for the two-level system. For the eighteen-level system with two cavity modes, three dissipation channels are relevant in the experiment: spontaneous emission of the atom, photon loss of the cavity field and laser phase noise. For the spontaneous emission of the atom, only the decay of the $P_{3/2}$ and $P_{1/2}$ states are taken into account as the timescale of experiments is short compared to the lifetime of the $D_{5/2}$ and $D_{3/2}$ states. The collapse operators of all three dissipation channels are written out in [65].

3.3.4 Numerical simulation

Numerical simulations of the system are implemented with the *quantum optics toolbox* by Sze Tan [82], a collection of Matlab routines that simplifies the formulation of a master equation and its numerical integration. In the context of the measurements presented in this thesis, two different kinds of simulations are realized:

- For simulation of the Raman spectra described in chapter 7, the steady state of the system is calculated by solving the equation $\dot{\rho} = 0$. In this case, the

system is driven by a monochromatic laser on the $S_{1/2} \leftrightarrow P_{3/2}$ transition and two repump lasers on the $P_{3/2} \leftrightarrow D_{5/2}$ and $P_{1/2} \leftrightarrow D_{3/2}$ transitions. From the resulting steady-state density matrix, we calculate the rate of photons at both polarizations that leave the cavity. Repeating this procedure for a range of laser detunings, we are able to reproduce the most prominent features of the Raman spectra.

- For simulation of the ion-photon state mapping measurements described in chapter 9, the time evolution of the system's density matrix ρ is calculated via numerical integration of the master equation. In this case, the system is driven by a bichromatic field on the $S_{1/2} \leftrightarrow P_{3/2}$ transition. For four different atomic input states, the polarization of cavity photons is calculated as a function of time, revealing the coherence of the mapping process. In this way, both the expected temporal single-photon shapes and the expected process fidelity are simulated. Moreover, the simulations help us to understand an unexpected interference effect of the bichromatic field, discussed in chapter 9. A significant part of the state-mapping simulations have been carried out by Birgit Brandstätter and will be further discussed in her thesis [83].

4 Experimental setup

Coupling a single atom to the mode of a high-finesse optical resonator offers a range of prospects to survey the features of quantum mechanics and benefit from them. First, fundamental effects of cavity-quantum electrodynamics can be explored. This was the subject of first studies carried out after the construction of the vacuum chamber containing ion-trap and high-finesse cavity by Carlos Russo [65]: by controlling fields driving the single ion, the statistical properties of the cavity field are tuned. In this way, the system can be steered to behave like a single-ion laser in a threshold-less quantum regime or in a classical regime featuring a laser threshold, as demonstrated in [84]. In subsequent studies, described in Helena Barros' thesis [85], we realized a single-photon source with our ion-cavity system, featuring high efficiency and high two-photon suppression [27].

With the tool for single photon generation at hand, another kind of studies become possible: the realization of quantum information protocols that employ the coherent ion-cavity interaction in order to distribute information in a quantum network. In such a quantum network, remote, stationary ions are linked by optical channels. The cavity now acts as a coherent interface between stationary and flying qubits via emitting and receiving single photons and transferring the information between atom and photon. The goal of this dissertation was to realize such an ion-photon interface by demonstrating fundamental protocols for ion-photon entanglement and state mapping. For this purpose, a laser at a wavelength of 729 nm was integrated into the existing experimental apparatus for coherent manipulation of the ion. The optical setup of the laser beams driving the Raman transition for the generation of single photons with controlled polarization was modified to generate a bichromatic field.

After a review of the design of the ion trap and the high-finesse cavity, this chapter focuses on those laser systems and the transfer lock of the cavity frequency. Additionally, it explains the geometry of the main laser beams with respect to the trap and the magnetic field axis and introduces the part of the apparatus that enables the readout of the atomic and photonic qubit. Finally, we consider some aspects of the vacuum-chamber design that should be considered for the construction of any new apparatus.

4.1 Overview

In the design of many cavity-QED experiments, a goal of high priority is to minimize the mode volume of the cavity in order to maximize the coupling between the atom and the cavity mode (eq. (3.12)). In the microwave domain, strong coupling has

been realized with macroscopic cavities on the length scale of tens of millimeters to centimeters [86, 87]. In the optical domain, mirror distances of just tens of micrometers to $\sim 100 \mu\text{m}$ enable strong coupling of single photons to single neutral atoms [28, 88].

For an ion-trap experiment in the optical domain, the combination of the trap with a high-finesse optical resonator appears as challenging as it is promising. Not only should the mirrors of the resonator be placed outside of the trap volume in order to avoid any change of the trapping potential, but also charges induced by laser light on the dielectric mirror surfaces result in patch potentials, disturbing the effective trapping potential [89]. On the one hand, the development of small traps therefore seems of great importance for this venture in order to achieve a small cavity mode volume. On the other hand, large traps offer deep trapping potentials and a large ion-electrode separation. Large traps thus feature long trapping times, low heating rates and minimal disturbance of the trapping potential due to patch potentials of the trap electrodes and the dielectric mirrors [90]. Furthermore, the location of both mirrors has to be controlled on the picometer scale in the direction of the cavity axis in order to stabilize the cavity's resonance frequency, and on the micrometer scale in the orthogonal directions to position the atom in an antinode of the cavity's standing wave (chapter 6). Typically, such high-precision adjustment of the mirrors is realized via piezoelectrics (piezos), controlled with high voltages. Care must then be taken in order to shield the ion from the electric fields originating from the piezos.

Due to the numerous technical challenges, only a few research groups have successfully realized integrated ion-trap cavity-QED systems to date [46, 47, 49–51]. Our experimental setup was built with the aim of employing the ion-cavity coupling in a Raman process. Here, the effective coupling strength can be made large compared to incoherent processes, such as atomic decay, by increasing the Raman detuning (sec. 2.3). With this strategy, a coupling strength one order of magnitude lower than the atomic decay rate can still result in a moderate effective coupling. This coupling has proven to be strong enough for the realization of fundamental quantum network protocols (chapter 8 and 9), while keeping the technological requirements feasible in a realistic laboratory setting. We use a slightly modified version of the standard Innsbruck linear Paul trap [91] optimized for optical access to the two cavity mirrors, which surround the cavity at a separation of about 2 cm (fig. 4.1). Trap and cavity are mounted in a vacuum chamber supporting ultra-high vacuum conditions at a pressure of $5 - 9 \cdot 10^{-11}$ mbar. Seven viewports offer optical access from outside the chamber both to address the ion with laser beams and to collect photons from the ion and the cavity (fig 4.1). The next two sections summarize the working principle of the Paul trap and the characterization of the optical resonator.

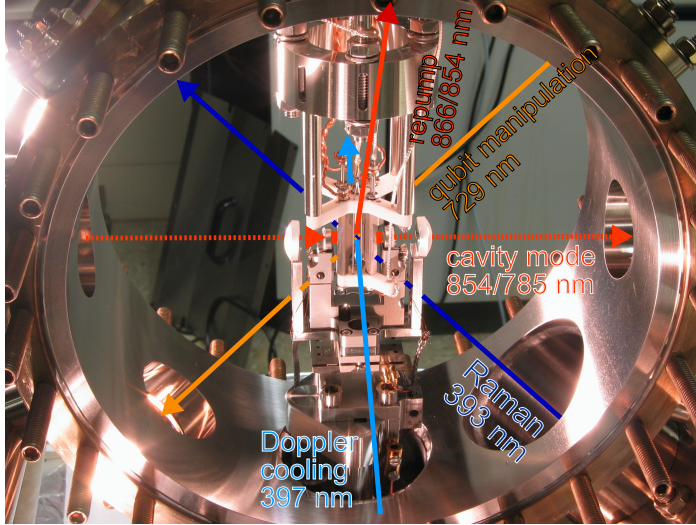


Figure 4.1: Photograph of the inside of the vacuum chamber, taken by Carlos Russo during the assembly process, with main laser beams indicated. The trap is mounted rigidly from the top of the chamber, while the cavity is mounted on translation stages from below. Two CF200 viewports (not shown) offer optical access to the ion from the front and back, two CF63 viewports (right/left) offer access to the cavity, and three CF63 viewports offer access to the ion from the side. One flange (lower left) is connected to a pump assembly consisting of an ion getter pump, a titanium sublimation pump, and an ultra-high vacuum gauge.

4.2 Linear Paul trap

The development of traps for charged particles started with the extension of linear quadrupole mass filters to three dimensions [92]. While Penning traps store charged particles in static electric and magnetic fields, Paul traps make use of an oscillating electric quadrupole field. A radial potential is generated by applying of electric radiofrequency (RF) fields to hyperbolically shaped electrodes [92]. Additional electrodes along the symmetry axis of the trap generate a static electric field in order to confine the particle in the third dimension.

The equation of motion of a single ion in a Paul trap can be transformed to a Mathieu equation with stable solutions [42]. The trajectory consists of secular motion at a frequency $\omega_{\text{sec}} \ll \omega_{\text{drive}}$ and a fast, small oscillation at the trap drive frequency ω_{drive} , called micromotion (sec. 5.8).

The design of our trap (fig. 4.2) is discussed in [65, 91]. The radial potential is generated by four blades, of which two opposing blades are grounded and the other two are connected to a helical resonator with a quality factor of about 200. An RF signal of 23.4 MHz is generated by a signal generator (Marconi) and is amplified to 5 W at 50 Ω load, resulting in radial trap frequencies for a single $^{40}\text{Ca}^+$ ion of $\omega_{\text{radial}}/(2\pi) = 3$ MHz. Two tip electrodes at a separation of 4 mm are used to axially confine the ion. With a

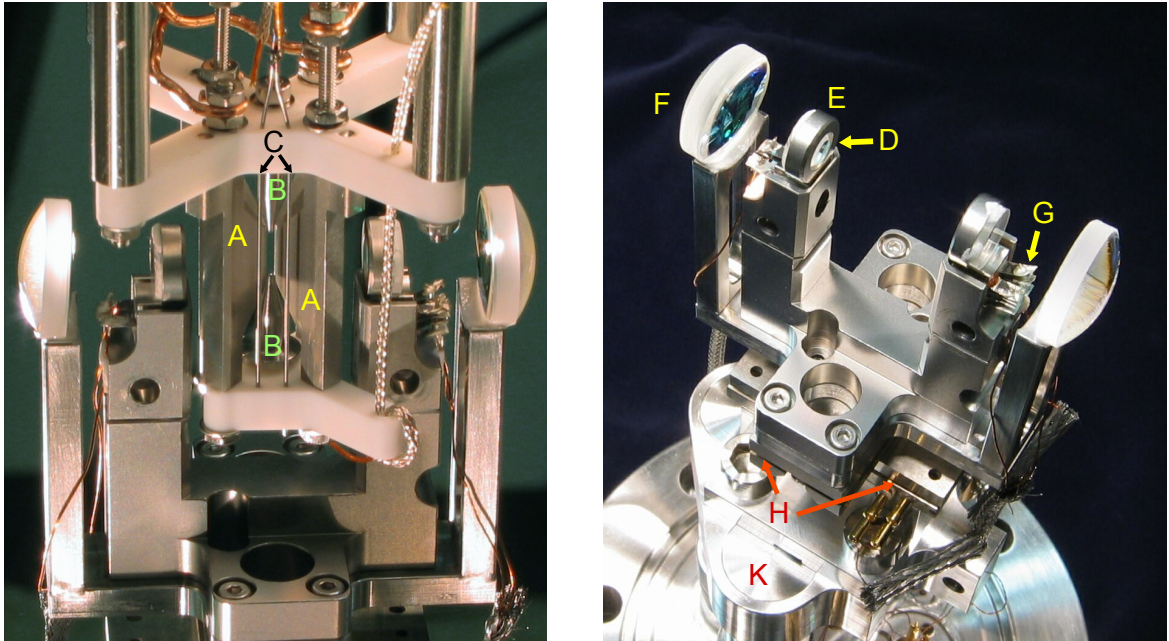


Figure 4.2: Photographs of the trap-cavity assembly and the cavity mount taken by Carlos Russo during the assembly process. Trap radiofrequency electrodes (A), tip electrodes (B), and wires for micromotion compensation (C) are mounted to white ceramic holders. Cavity mirrors (D) are glued to stainless-steel holders (E) glued on piezo stacks (G) that allow for adjustment of the mirror position along the cavity axis. Collimation lenses (F) are fixed to the same mount as the mirrors. Translation stages driven by slip-stick piezos (H) allow for adjustment of the entire cavity mount with respect to the trap in the two horizontal directions. The mount is fixed to a table (K) that can be tilted by means of a feedthrough.

DC voltage of about 900 V applied to the the tip electrodes, the axial trap frequency is measured to be $\omega_{\text{axial}} = 1.1$ MHz. Two pairs of rigid wires serve as micromotion compensation electrodes. The voltages applied to the tip and micromotion electrodes are generated by a stable high-voltage source¹ ($\Delta V/V \sim 10^{-5}$).

In order to load a single $^{40}\text{Ca}^+$ ion into the trap, a calcium oven is heated by a current of 4.5 A. The beam of neutral calcium emitted from the oven is collimated by the cavity holder and ionized in the trapping volume by two laser beams [65].

4.3 Optical cavity

At the heart of our experimental setup lies the high-finesse optical resonator. For the realization of a coherent light-matter interface, the goal of many cavity-QED experiments is to obtain a coupling strength between the stationary qubit and the

¹ISEG EH08020x_405_SHVK1

vacuum mode of the resonator as high as possible (sec. 2.3). In the case of symmetric Fabry-Perot cavities, i.e., where both mirrors have the same radius of curvature, the mode volume V_0 of the fundamental TEM₀₀ with waist w_0 is given by

$$V_0 = Lw_0^2\pi/4, \quad (4.1)$$

where L is the mirror separation. A small mode volume can be achieved by a short cavity, a small mode waist, or both. For neutral atom experiments, the mode volume is typically minimized in a near-planar configuration where the mirror separation is chosen to be much smaller than the radius of curvature of the mirrors R [28]. For a single ion in a linear Paul trap, the near-planar approach is impractical as the mode waist would be too large at the mm-to-cm scale separation between the mirrors required so that the mirrors are outside the trap blades. A confocal cavity geometry provides the most stable optical mode with respect to any displacement of the mirrors [93]. This configuration was chosen in the experimental design of ref. [94] with the objective of coupling 500 ions to the TEM₀₀ mode with waist $w_0 = 37 \mu\text{m}$. Here, the coupling strength of an individual ion is $g_0 = 2\pi \times 0.5 \text{ MHz}$. A configuration in between the confocal and the planar geometry with waist $w_0 = 24 \mu\text{m}$ has been chosen in [95], resulting in a single-ion coupling strength of $g_0 = 2\pi \times 0.92 \text{ MHz}$.

In our setup, a near-concentric optical-resonator configuration has been chosen as it minimizes the mode waist at the ion's position and therefore maximizes the coupling strength. Furthermore, a long cavity minimizes the cavity decay rate κ , resulting in maximum cooperativity [65]. Two mirrors with radius of curvature specified to $R = 10 \text{ mm}$ are mounted around the trap with a separation of $L = (19.96 \pm 0.02) \text{ mm}$. Each cavity mirror is mounted on a shear-mode piezo stack. The *fast* stack is composed of two PZT layers, the *slow* one of six PZT layers, glued together by hand. Each of the layers can be driven by a maximum of $\pm 250 \text{ V}$. For a voltage difference of 400 V , the mirrors on the slow and fast piezo stack move by 1.6 and $0.5 \mu\text{m}$, respectively [65]. The length of the cavity is actively stabilized with respect to an ultra-stable passive cavity by means of a transfer lock at 783 nm as described in sec. 4.4. The entire cavity mount, containing both mirrors and mode-matching lenses, is positioned via translation stages driven by slip-stick piezo elements (Omicron MS5) in the two horizontal directions (fig. 4.2) with a precision of $\sim 100 \text{ nm}$ per step. Additionally, the angle of the cavity mount can be coarsely positioned by means of a vacuum feed through and micropositioning screws.

At the wavelength $\lambda = 854 \text{ nm}$, resonant with the $P_{3/2} \leftrightarrow D_{5/2}$ transition that is relevant for this dissertation, the finesse measurement yields a value of $\mathcal{F} = 77,000 \pm 1,000$. Due to asymmetric mirror transmissions $\mathcal{T}_1 = 1.3 \pm 0.3 \text{ ppm}$ and $\mathcal{T}_2 = 13 \pm 1 \text{ ppm}$, the cavity field decays preferentially through one mirror of the resonator. For the decay rate we obtain

$$\kappa = \frac{2\pi c}{4L\mathcal{F}} = 2\pi \times (48.8 \pm 0.6) \text{ kHz}. \quad (4.2)$$

All relevant parameters of the cavity are reported in Carlos Russo's thesis [65].

Since [65], technical improvements such as better Doppler cooling (sec. 5.2) and precise vertical positioning of the ion via adjusting the voltages of the trap tip electrodes have led to an improved localization of the ion inside the mode structure of the resonator (chapter 6). We have re-measured and re-interpreted the values of the mirror radius of curvature R and the cavity length L given in [65]. In contrast to [65], we determine the mirror distance $L = (19.96 \pm 0.02)$ mm from a measurement of the cavity's free spectral range. Although this results in a higher uncertainty of L , we are now able to estimate the error on the manufacturer-specified value of R by a measurement of the frequency splitting of the TEM₀₀ and TEM₀₁ modes, which depends on both L and R [96]. We infer $R = (10.02 \pm 0.01)$ mm, from which we calculate

$$w_0 = \sqrt{\frac{\lambda}{2\pi}(L(2R - L))^{1/2}} = (13.2 \pm 0.8)\mu\text{m} \quad (4.3)$$

and thus a maximum coupling rate of

$$g_0 = 2\pi \times (1.43 \pm 0.01) \text{ MHz} \quad (4.4)$$

for the $D_{5/2} \leftrightarrow P_{3/2}$ transition, while [65] states $w_0 = (13.2 \pm 0.2) \mu\text{m}$ and $g_0 = 2\pi \times (1.55 \pm 0.02) \text{ MHz}$.

A fundamental property of the cavity is that it supports degenerate polarization modes, which we parametrize with orthogonal linear polarizations H (horizontal) and V (vertical). Any birefringence induced by stress of the mirror coatings is smaller than the cavity linewidth, as demonstrated by the high fidelities of ion-photon entanglement and state mapping (chapter 8 and 9).

The output coupling efficiency was calculated to be 16% at 854 nm in [65] due to combined mirror losses of 68 ± 2 ppm. However, from the photon generation efficiency of the atom-photon entanglement process (sec. 8.4), in which we calibrate the output path (sec. 4.10), we conclude that the output coupling rate is higher: 20%.

4.4 Laser systems

In an ion-trap experiment, the various laser systems are important experimental tools that control the quantum state of the ion. Most laser systems in our laboratory are shared between several experimental setups, which individually control the frequency and intensity of their beams by acousto-optical modulators (AOMs). All lasers are brought to the vacuum chamber via optical fibers. With the exception of the photo-ionization lasers, all lasers are frequency-stabilized to high-finesse reference cavities. The laser frequencies are measured by a wave-meter (High Finesse WS7). The optical setup of the lasers at 397 nm, 866 nm and 854 nm for cooling and state detection, at 422 nm and 375 nm for photo-ionization, and at 785 nm for the transfer lock of the trap cavity have been described in detail in [65, 85]. In this section, we focus on the

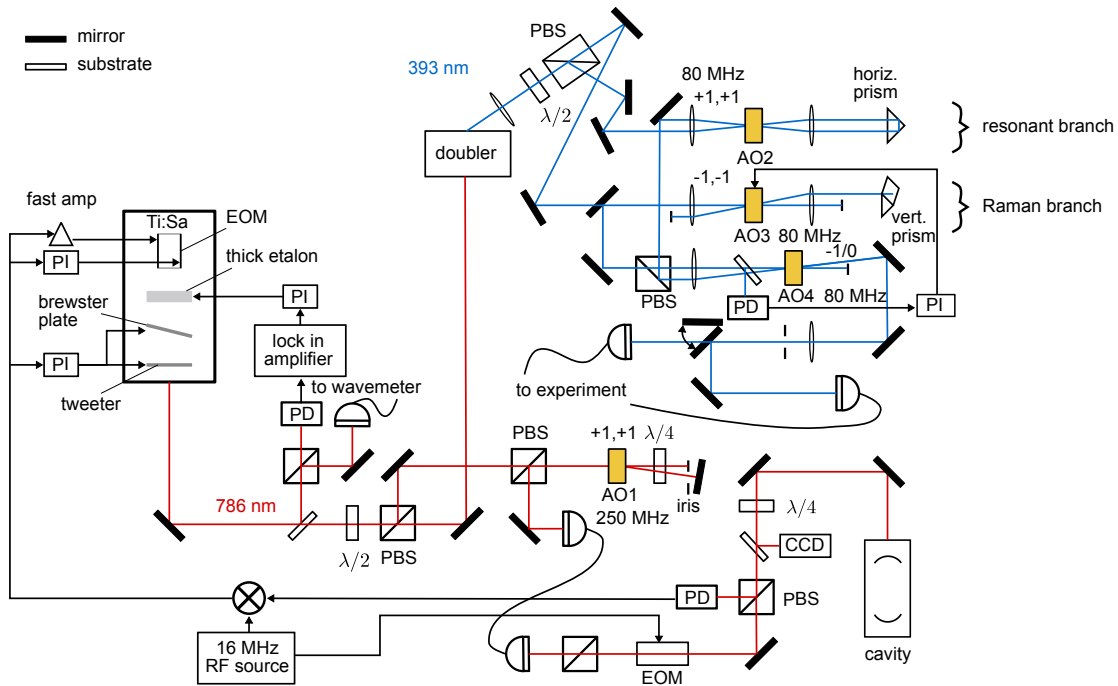


Figure 4.3: Laser setup at 393 nm for driving Raman transitions. PD: photodiode, PI: proportional-integral controller, AO: acousto-optic modulator, PBS: polarizing beamsplitter. A Ti:sapph ring laser at 786 nm is stabilized to an external reference cavity using the Pound-Drever Hall method. The laser frequency is tuned to match the cavity’s resonance via an AOM (AO1). Feedback is applied to a tweeter mirror, a Brewster plate, and an intra-cavity EOM [97]. Additionally, the angle of the thick etalon is stabilized via an external lock-in amplifier. Light at 786 nm is frequency-doubled to 393 nm and frequency shifted via double pass AOMs. In the resonant branch, the light is shifted by +160 MHz by AO2 (vertically mounted) in double-pass configuration to match the resonance of the $S_{1/2} \leftrightarrow P_{3/2}$ transition (+1, +1 denotes the diffraction order in first and second passage through the AOM). In the Raman branch, we use the $-1, -1$ order of AO3 (horizontally mounted, double pass) that is shifted by -160 MHz in order to match the Raman transition. A third AOM (AO4) in single-pass configuration is driven at two frequencies to generate the bichromatic field. AO4 is switched off if the resonant beam is used. The beam is coupled to one of two fibers that guide the light to two different ports at the experimental table.

setup of the laser at 393 nm that is used for generating a bichromatic Raman field (sec. 8.3) and which was re-designed in 2011, and the setup of the laser at 729 nm for state manipulation that was built in 2009. Additionally, we review the trap-cavity lock highlighting recent improvements.

Raman laser at 393 nm

In order to produce photons on the $S_{1/2} \leftrightarrow P_{3/2} \leftrightarrow D_{5/2}$ transition, we drive the $S_{1/2} \leftrightarrow P_{3/2}$ transition at 393 nm with a laser while the $P_{3/2} \leftrightarrow D_{5/2}$ transition is coupled to the vacuum field of the cavity (chapter 7). Light at 393 nm is obtained by frequency-doubling the light of a titanium-sapphire (Ti:sapph) ring laser (Coherent 899-21) at 786 nm. The Ti:sapph laser is pumped by a solid-state laser (Coherent Verdi V10). For frequency doubling, we use a commercial system (Coherent MBD-200) consisting of a frequency-doubling crystal inside an actively stabilized bow-tie cavity. For an input power to the doubler of about 500 mW at 786 nm, we achieve an output power of up to 80 mW at 393 nm. At the ion, we typically obtain 1-2 mW of 393 nm laser light, more than sufficient for driving the Raman transition.

The linewidth of the Raman transition is limited by the cavity linewidth for Rabi frequencies of the 393 nm laser below saturation (sec. 2.3). The linewidth of the 393 nm laser thus has to be smaller than $2\kappa \approx 100$ kHz in order to efficiently drive the Raman process. The electronics of the Ti:sapph laser system were therefore modified by Helena Barros for stabilizing its frequency to an external high-finesse cavity [85]. One branch of the laser traverses an electro-optical modulator (EOM) driven at a frequency of 17 MHz in order to produce optical sidebands. The beam is then coupled into a temperature-stabilized reference cavity. In order to generate a Pound-Drever-Hall (PDH) error signal [98], we mix the cavity reflection signal detected on a fast photodiode (125 MHz bandwidth) with the frequency that drives the EOM. This external error signal is used as input for proportional-integral (PI) controllers that close the feedback loop to a mirror which is mounted on a piezo ("tweeter"), an angle-tunable glass plate ("Brewster plate"), and an intra-cavity EOM (fig. 4.3) following the setup presented in [97]. For the tweeter mirror and the Brewster plate, the feedback signal is added to the internal error signal of the laser's locking electronics. An intra-cavity EOM was additionally installed into the ring laser for increasing the lock bandwidth. In order to take advantage of the EOM's tuning range and its bandwidth, we divide its feedback signal into two branches that share a common ground. Each signal is connected to one of the two electrodes of the EOM. In the fast branch, the PDH error signal is filtered by an amplifier² with a bandwidth of 10 MHz. In the slow branch, the error signal is amplified to ± 150 V. Additionally, we have modified the lock of the thick etalon to provide stable frequency tuning over a range of ~ 5 GHz. It is now stabilized via an external lock-in amplifier providing a separate error signal to an additional PI controller. With all feedback signals applied to the individual components, we estimate from the deviations of the in-loop error signal that the linewidth of the 393 nm laser is less than 30 kHz. At one third of the linewidth of the Raman transition, the laser linewidth therefore does not limit the efficiency of the Raman process.

After the frequency doubling stage, the ultraviolet laser light is split into two

²FEMTO HVA-10M-60-B

branches (fig. 4.3), one providing a resonant beam and the other providing a beam for driving the Raman transition (Raman beam). Both of these branches are tuned in frequency by a double-pass AOM driven at 70 – 90 MHz. The use of different diffraction orders allows for shifting the frequencies of the resonant and the Raman beam with different sign. In the resonant branch, we use the first positive diffraction order of both passages through the AOM (+1, +1 order) to generate a beam that is in total shifted by +160 MHz and thus resonant with the $S_{1/2} \leftrightarrow P_{3/2}$ transition. This beam is only used for alignment of optical elements on the experimental table: the fluorescence signal at 393 nm collected from the ion is maximized by aligning the resonant beam onto the ion, yielding a signal-to-noise rate which is one order of magnitude larger than the Raman beam. In the Raman branch, we use the first negative diffraction order of both passages (–1, –1 order) of the AOM to obtain an off-resonant beam that drives the Raman transition. This beam subsequently traverses a second AOM which is arranged in single-pass configuration. We use the –1 order of this AOM, obtaining a detuning of ~ 400 MHz of the Raman beam from the $S_{1/2} \leftrightarrow P_{3/2}$ transition. In order to generate the phase-stable bichromatic Raman field, we drive this AOM with two distinct frequencies simultaneously and couple both first-order shifted beams into the same fiber. As both beams traverse the same optical elements between the AOM and the fiber, namely, two lenses, interferometric stability is not an issue. With this setup we can efficiently generate a bichromatic field with frequency differences up to 13 MHz, as needed for the state mapping (sec. 9.2). For frequency differences exceeding 13 MHz, the coupling efficiency to a single-mode fiber decreases as the angular separation of the two beams rises above the aperture of the fiber. The RF sources that drive the AOMs are described in sec. 4.11.

The bichromatic field is coupled into one of two polarization-maintaining fibers that guide the light to two different ports on the experimental table (sec. 7.1). As the AC-Stark shift of the Raman transition depends on the Rabi frequency of the drive laser, intensity fluctuations of the drive beam lead to a reduced efficiency of the Raman transfer for low Rabi frequencies. We have therefore introduced two stages of active intensity stabilization of the 393 nm beam. The first one detects the intensity after the frequency doubler and feeds back to the double-pass AOM to cancel the 20% intensity noise of the commercial system. Furthermore, the 12 m long optical fiber connecting the laser and the experimental table introduces slow polarization fluctuations, which are converted into intensity fluctuations of up to 5% after a polarizing beamsplitter (PBS). We therefore use a homebuilt sample-and-hold circuit that actively stabilizes the intensity of laser pulses between subsequent executions of the experimental sequence to $\leq 1\%$ via feedback to the single-pass AOM. The error signal is provided by a fast photodiode³ (bandwidth 200 MHz) that detects the beam intensity after it has traversed the vacuum chamber.

³Femto HCA-S-200M

Quadrupole laser at 729 nm

In contrast to previous studies carried out with this experimental apparatus [84, 85], we need to initialize, coherently manipulate, and detect the state of the atomic qubit for the realization of quantum interface protocols. For this purpose, we introduced a laser at 729 nm that drives the quadrupole $S_{1/2} \leftrightarrow D_{5/2}$ transition. As described in chapter 5, spectroscopy on this transition is also used to characterize trap frequencies, magnetic field, heating rates and micromotion.

For coherent manipulation of the ion's state via the narrow quadrupole transition, the laser should be stabilized to high precision both in frequency and intensity. In our laboratory, a Ti:sapph laser at 729 nm is frequency-stabilized to an ultra-stable high-finesse cavity resulting in a laser linewidth of a few Hz, as described in Michael Chwalla's thesis [97]. As an ultra-stable laser requires an ultra-stable frequency reference, a reference cavity is build out of ultra-low expansion (ULE) material. In order to shield the cavity from external perturbations, temperature and mechanical stability of the entire mount are actively stabilized. In one of three experimental setups sharing the light of this ultra-stable laser, the frequency of the cavity is measured over time with respect to the resonance frequency of a trapped $^{40}\text{Ca}^+$ ion using Ramsey spectroscopy [97]. The long-term frequency drift of the cavity on the order of a few Hz/s is then compensated by an AOM that shifts the frequency of the laser with respect to the reference cavity. By seeding a tapered semiconductor amplifier (Toptica TA100) on the same optical table with ~ 10 mW of the light from the Ti:sapph laser, we obtain ~ 400 mW at the output of the TA100 at an operating current of 1.5 A. In this way, three experimental setups benefit from the effort of constructing an ultra-stable laser at 729 nm.

After mode-cleaning the output of the TA100 via a single-mode optical fiber, we divide the remaining 150 mW of 729 nm light between two experimental setups. In our setup, the beam is guided to the experimental table via a polarization-maintaining fiber after passing through two single-pass AOMs, which each shift the frequency by a fixed value of 80 MHz. The AOMs are used for stabilizing the intensity after the fiber and for canceling the frequency noise generated by acoustic vibrations of the fiber. The latter is achieved by the approach of [99]: a beamsplitter before the AOM and a photodiode at one beamsplitter port are used to realize an optical beat measurement between the light in front of the AOM and the light that traverses both AOM and fiber, is reflected at the fiber output facet, and travels back to the beamsplitter. The beat signal at 160 MHz contains the phase noise induced by the fiber. This noise is compensated by a phase-locked loop, described in detail in [97, 100].

On the experimental table, we use a double-pass AOM at 270 MHz in order to tune the frequency of the 729 nm beam to the target quadrupole transition frequency. Short fibers (1-2 m) guide the light to the vacuum chamber. As the optimum direction of the beam for driving the target quadrupole transitions depends on the direction of the magnetic field for a particular measurement (sec. 8.3 and sec. 9.2), we have

installed optics for beam focusing and polarization control at three different ports illuminating the ion from three non-collinear directions. All three ports are used for the compensation of micromotion in three dimensions (sec. 5.8). For one of the ports, a summer student, Peter Cristofolini, developed an objective capable of addressing one of two neighboring ions. His supervision was part of this thesis work. After assembly of the objective in a clean-room, Diana Habicher [101] characterized its beam profile at the ion’s position (sec. 4.7).

4.5 Transfer lock

In order to drive one arm of a Raman transition with the vacuum field of the cavity, the cavity’s frequency must satisfy a resonance condition with the other Raman arm driven by the laser. The frequency of both laser and cavity must therefore be stable within the linewidth of the Raman transition. For vanishing Rabi frequencies of the drive laser, the linewidth of the Raman transition approaches the cavity linewidth 2κ . To efficiently drive the Raman transition, the resonance frequency of the cavity must then be accurate to within 2κ . This requirement transfers to a length stability of $\delta l = \lambda/(2\mathcal{F}) \approx 6$ pm [65]. This small value highlights the technical challenge we have to face for stabilizing the length of the cavity.

As an optical cavity which is mounted on an ULE spacer is a very precise frequency reference, we use a transfer lock technique [65, 102] in which a diode laser is stabilized to such a reference cavity. The length of the cavity around the ion trap (referred to in the following as the *trap cavity*) in turn is stabilized to the laser. The wavelength of this laser is chosen to be 785 nm, far from any relevant $^{40}\text{Ca}^+$ transition to avoid AC-Stark shifts of the atomic levels. The coating of the cavity mirrors was therefore designed to enable a high finesse both at 854 nm and 785 nm.

In order to resonantly drive the Raman transition, the detuning of the cavity from the $P_{3/2} \leftrightarrow D_{5/2}$ transition has to match the detuning of the drive laser from the $S_{1/2} \leftrightarrow P_{3/2}$ transition (fig. 3.1). We therefore overlap a reference beam at 854 nm which is 400 MHz detuned from the $P_{3/2} \leftrightarrow D_{5/2}$ transition with the beam at 785 nm at a dichroic mirror and couple both lasers to the trap cavity (fig. 4.4). While scanning the length of the cavity via the fast piezo, we now tune the length of the trap cavity via the slow piezo such that it becomes resonant with the 854 nm beam. While we are able to tune across five free spectral ranges with the slow piezo, we typically choose the mode for which we have to apply the smallest voltage in order to avoid excess micromotion (sec. 5.8). We now tune the frequency of the 785 nm laser until we find a mode that is resonant with the trap cavity and the reference cavity at the same time (“double resonance”). For exact matching of the two frequencies, we adjust the frequency of a double-pass AOM that shifts the frequency of the 785 nm light sent to the trap cavity. To avoid AC-Stark shifts of any atomic state, we choose the TEM_{01} mode at 785 nm in the trap cavity because it has an intensity minimum along the

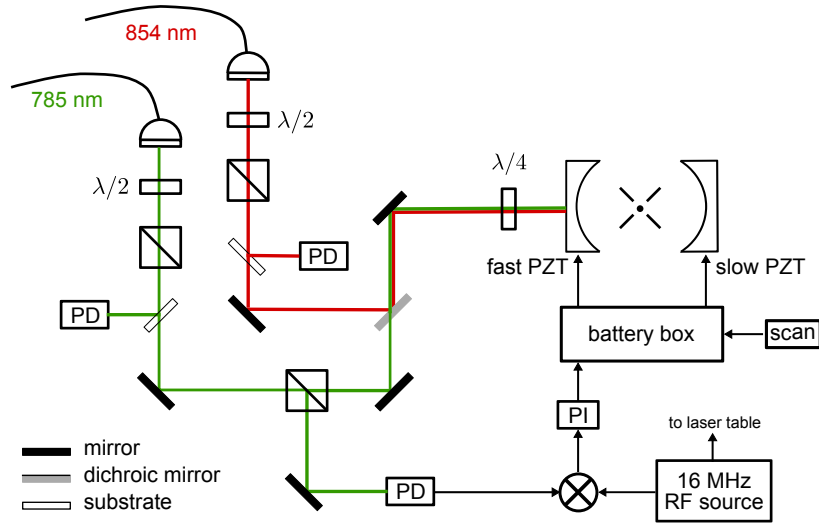


Figure 4.4: Transfer lock of the trap cavity. The laser at 854 nm, about 400 MHz detuned from the $P_{3/2} \leftrightarrow D_{5/2}$ transition, is used as a frequency reference. The laser at 785 nm is first tuned to a frequency which is resonant with the trap cavity and its reference cavity on the laser table (not drawn) at the same time. The laser frequency is then stabilized to the reference cavity. A Pound-Drever-Hall signal provides feedback to the trap-cavity piezos in order to stabilize the cavity length with respect to the laser at 785 nm.

cavity axis where the ion is trapped. Once double resonance is achieved, the 854 nm reference beam is no longer needed and is turned off.

Transfer-lock laser at 785 nm

Finding a double resonance would be an unproblematic procedure if one had a perfect laser system available that can be tuned without mode hops. However, for a real system, the effort of finding double resonance depends on how smoothly the 785 nm laser can be tuned. Until 2010, we used a Toptica DL100 laser that jumped several times to different modes during a scan over the free spectral range of the trap cavity. As a consequence, double resonance could only be achieved by chance at a certain piezo voltage and laser current. The laser was therefore exchanged for a Toptica DLpro laser, which is tunable without mode hops for more than one free spectral range of the trap cavity (8 GHz). This new laser system marks a very important technical upgrade of our setup that can hardly be overestimated. In order to frequency stabilize the transfer lock laser, we employ the PDH locking technique by generating optical sidebands with an EOM. The diode laser is locked to the reference cavity via the piezo controlled grating position and the diode injection current. A graphic illustration of the optical setup of the transfer lock laser is given in [65], fig. 4.15 and [85], fig. 4.10.

Ultra-stable reference cavity

The same cavity is used as a frequency reference both for the 786 nm laser (later doubled to 393 nm) and the 785 nm laser. Drifts of the reference cavity thus shift both the trap cavity frequency and the Raman laser frequency. To first order, these shifts are equal and Raman resonance is then still fulfilled. The reference cavity was originally designed for the laser system at 729 nm. Its design is described in detail in [103]. The mirrors are glued rigidly to a 15 cm long ULE spacer, resulting in a free spectral range of 1 GHz. The entire mount of the spacer with the mirrors is located in a vacuum chamber at $\sim 10^{-8}$ mbar, which sits on a rubber board on the optical table. The temperatures of the chamber and the surrounding insulating box are stabilized in two separate stages. The finesse of the cavity at 785 nm has been measured to be $\mathcal{F} = 2000$, corresponding to a linewidth of 500 kHz [65].

Battery box

The lock of the trap cavity to the reference laser is accomplished via controlling the voltage of the fast piezo (fig. 4.2 (G) and 4.4), corresponding to microscopic displacements of the mirror $\ll 1$ nm. Simultaneously, we position the ion in the cavity standing wave by controlling the voltage of the slow piezo within ± 200 V, corresponding to macroscopic displacements on the order of several hundreds of nanometers. In order to change the position of the standing wave while the cavity is locked, the fast piezo has to follow the macroscopic displacement of the slow piezo. Following the slow piezo over a free spectral range requires tuning the voltage applied to the fast piezo by about 100 V, more than the ± 15 V output voltage of the PI controller. In the past, the signals for both piezos were generated by high-voltage amplifiers. Although the amplifiers were low-pass filtered, their stability used to limit the linewidth of the trap cavity lock.

We therefore developed an electric circuit to combine the feedback signal with high-voltage batteries⁴, explained in appendix A. For a common displacement of both mirrors, as required for the scan of the cavity standing wave with respect to the ion, we implemented a feed-forward: a fraction of the voltage applied to the fast piezo is simultaneously applied to the slow piezo in order to displace both piezos by the same amount.

By driving the piezos with batteries instead of high-voltage amplifiers, we were able to slightly improve the cavity lock. However, the stability of the cavity remains limited by acoustic vibrations excited by the acoustic noise of flow boxes and the air conditioning system coupling to the vacuum chamber [85]. We previously thought that acoustic vibrations of the trap-cavity mount compromised the cavity stability along the cavity axis [65]. However, we have recently demonstrated that this is not the case,

⁴Energizer EVEREADY 493, 300V

using a measurement in which the standing wave is translated around the ion position (sec. 6.1).

As the piezo stacks are mounted at a distance of about one centimeter from the trapping volume, care has to be taken that the electric fields originating at the piezo stacks do not disturb the trapping potential. The stacks are therefore glued inside of a stainless-steel mount [65]. Nevertheless, we have recently observed that a voltage change at the piezo stacks by more than 10 V results in an increase of micromotion in the direction orthogonal to both the cavity and trap axis, measured via spectroscopy on the quadrupole transition (sec. 5.8). As excess micromotion reduces the coupling strength of the ion to the cavity, we no longer position the standing wave with respect to the ion via changing the voltage of both piezo stacks. Instead, we use the piezo translation stage that moves the entire cavity mount. In this way, any excess micromotion remains compensated.

4.6 Laser beam geometry

The propagation and polarization axes of laser beams with respect to the trap axes in an ion-trap experiment are typically chosen in order to cool all motional modes and manipulate the qubit on sidebands of target quadrupole transitions [104]. In our experimental setup, moreover, we have to choose the magnetic field direction carefully with respect to the cavity axis in order to define the polarization states of the photonic qubit (sec. 7.1). The direction of the magnetic field in turn determines the necessary beam polarizations.

In our setup, we choose the direction of the magnetic field to be orthogonal to the cavity axis. The direction of each laser beam is assigned with respect to the trap, cavity, and magnetic field axes depending on its purpose. The configuration of the main laser beams is indicated in fig. 4.5.

The Raman drive laser at 393 nm can be sent to the ion along two paths. Beam A propagates at an angle of $\sim 45^\circ$ to both the cavity and trap axis. Its linear polarization is oriented orthogonal to the magnetic field axis in order to drive σ^+ and σ^- transitions simultaneously (sec. 7.1). Beam B propagates in the direction of the magnetic field with circular polarization and thus can drive either σ^+ or σ^- transitions.

For Doppler cooling and state detection, two beams at 397 nm are directed to the ion from different directions (fig 4.5). The reason for using two beams will be explained in sec. 5.2. A third beam with σ^+ polarization propagating along the magnetic field direction is used for optical pumping.

Two repump beams at 854 nm and 866 nm are guided from the laser table to the experimental table in the same optical fiber with orthogonal linear polarizations. These two beams are sent to the ion along the direction of the magnetic field with linear polarization, so that they drive both σ^+ and σ^- transitions. In this way, all states of the $D_{5/2}$ and $D_{3/2}$ manifolds are repumped. Additionally, a probe beam at

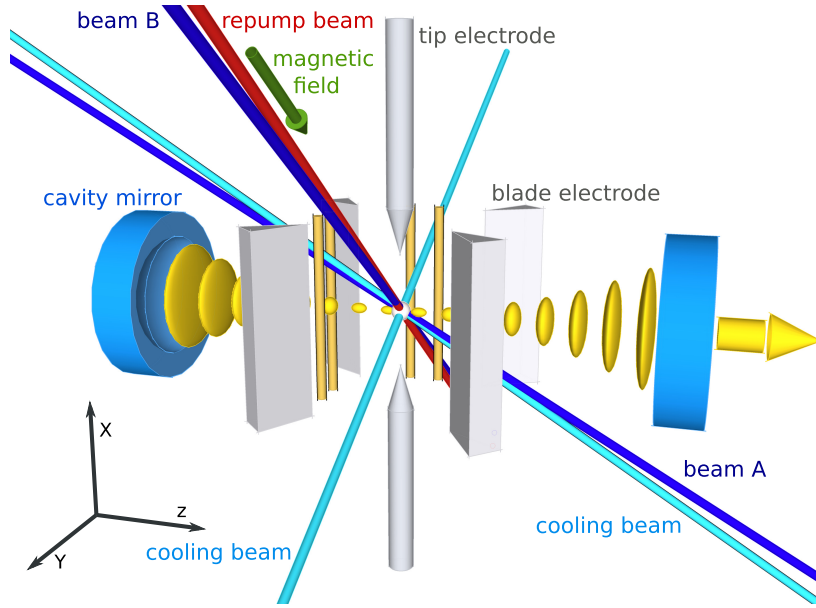


Figure 4.5: Geometry of main laser beams with respect to ion trap and cavity. Sketched are tip and blade electrodes (grey), and micromotion compensation electrodes (yellow). The cavity mirrors (blue) confine a standing wave (yellow); an arrow at one mirror indicates the output channel. The orientation of the magnetic field is perpendicular to the cavity axis. The Raman transition is driven by beam A (linearly polarized) or beam B (circularly polarized), both at 393 nm. Two beams at 397 nm cool the ion. A third, σ^+ polarized 397 nm beam (not shown) for optical pumping propagates along the magnetic field. From the opposite direction, linearly polarized repump beams at 854 nm and 866 nm share the same path. Three laser beams at 729 nm for coherent state manipulation are available from different directions (not shown): one in the $x - y$ plane and with an angle of about 22.5° to the trap axis, one parallel to beam A, and one orthogonal to beam A in the $x - z$ plane. The photo-ionization beams at 422 nm and 375 nm (not shown) are collinear with the cooling beam in the $x - y$ plane.

854 nm or 866 nm can be sent through the trap cavity for cavity alignment purposes but not used during experiments.

Three beams at 729 nm are sent to the ion. The first beam propagates orthogonal to the cavity axis and with an angle of about 22.5° to the trap axis (in the x - y plane in fig. 4.5). This angle is chosen in order to reduce the Lamb-Dicke parameter with respect to the ion's axial mode of motion. This first beam is used for state initialization and read-out in the ion-photon entanglement measurements. The second and third beam are sent to the ion under an angle of 45° , to the trap and cavity axis. The second beam is used for state initialization in the state-mapping measurements, where the magnetic field direction is changed (sec. 9.2). The third beam is a tightly focused beam that can address one of two ions, as explained in the next section.

Photo-ionization beams at 422 nm and 375 nm are overlapped with the 397 nm beam propagating in the plane orthogonal to the cavity axis.

4.7 Ion addressing

In future experiments, we envision coupling two ions to the same cavity mode, requiring control over their individual coupling at any time. Such control could in principle be achieved by shifting the ions within the standing wave of the cavity (sec. 6.1). However, compared to switching high voltage signals on the μs -timescales within a sequence of laser pulses, the shelving of individual ions to an uncoupled state offers a more robust technique. Any addressing laser beam must be focused to a waist smaller than the typical distance of the ions in order to avoid perturbation of the neighboring ion. For a trap-tip voltage of 900 V, this distance is about $5\ \mu\text{m}$. As a second constraint, the beam should have a component along the trap axis in order to be able to drive sidebands of the axial motion. Although optical access to the ion from outside of the vacuum chamber seems ample in our setup, the best spots are already occupied by the two objectives of PMT and CCD camera. No simple solution for an addressing beam through either of the two large viewports at an angle of 45° , could be found due to significant spherical aberrations caused by the 1 cm thick glass. From the other directions, only a viewport with diameter of $a = 35\ \text{mm}$ at a distance from the ion of $d \approx 130\ \text{mm}$ is available. The diffraction limit for these parameters yields an Airy diameter of $1.22 d\lambda/a = 3.3\ \mu\text{m}$ at 729 nm [105]. Opting for this viewport, we thus had to build a diffraction-limited objective.

After determining all constraints, Peter Cristofolini designed the lenses and the mechanical setup of the objective [106]. Optimization of the lens positions and radii with the ray tracing software Zeemax results in an expected rms-spot radius of $4\text{--}5\ \mu\text{m}$ for a setup with three meniscus lenses correcting the spherical aberrations of one collimation lens and the vacuum window. While the lenses were manufactured by Lens Optics, the aluminum rings and the objective holder were built in our own mechanical workshop. All parts were mounted in a clean room in order to avoid dust particles settling in between the lenses.

The objective was mounted on a translation stage with motorized actuators and characterized by Diana Habicher [101]. In order to measure the Gaussian intensity profile of the beam after the objective, we translate a single ion through the beam via adjustment of the tip electrode voltages. The first Airy minimum is located $7\ \mu\text{m}$ from the maximum of the Gaussian intensity profile. For addressing one of two ions, the addressing error can be minimized by positioning the target ion at the slope of the intensity profile and the second ion at the Airy minimum. In order to characterize the addressing error, we drive one of the quadrupole transitions through the objective. For the addressed ion, we measure a Rabi frequency which is 50 times higher than for the neighboring ion. By applying a combination of laser pulses with the addressed

and global beam that illuminates both ions, we are now able to control which of the two ions couples to the cavity. This control enables the realization of schemes like proposed in [107], in which two or more ions sequentially couple to the cavity to produce a stream of photonic cluster states.

4.8 Magnetic field

A magnetic field is applied to the ion in order to lift the degeneracy between the Zeeman substates of each manifold of $^{40}\text{Ca}^+$. This splitting avoids coherent population trapping during cooling and detection periods. Moreover, it enables the addressing of individual states via the laser frequencies. Additionally, a stationary magnetic field B suppresses the influence of magnetic-field fluctuations ΔB perpendicular to B on the atomic coherence time [30].

In our setup, a magnetic field of 3–5 G is applied via three pairs of coils in a Helmholtz configuration. One pair of coils is mounted in the direction of the cavity axis (z-axis in fig. 4.5) and conducts a current of 312 mA in order to compensate the earth’s magnetic field. Two additional pairs of coils (along the x- and y-axis of fig. 4.5) generate a magnetic field with direction orthogonal to the cavity axis and at an angle of about 45° to the trap axis. The direction of the field was changed compared to [65, 85] to obtain higher Raman transition strengths, as explained in detail in sec. 7.1. For this purpose, a new coil was installed at the bottom of the chamber.

The absolute value of the field is chosen in order to separate carriers from motional sidebands of neighboring transitions in the Raman spectrum (sec. 7.2) as well as in the $S_{1/2} \leftrightarrow D_{5/2}$ spectrum. For ion-photon entanglement, a field of 2.96 G is set by currents of 606 mA in the coil pair in the x-direction and 274 mA in the y-direction (fig. 4.5). For ion-photon state mapping, the optimum situation is realized at a field of 4.50 G, with the direction of the field rotated by 90° around the cavity axis. Here we used a current of 1055 mA in the coil pair in x-direction and a current of 351 mA in the coil pair in y-direction.

The currents applied to the coils are actively stabilized to an accuracy of 10^{-5} by a servo loop integrated in a home-built circuit. However, external magnetic field noise at 50 Hz present in the lab at a peak-to-peak amplitude of 10–100 mG presents a much larger source of magnetic-field fluctuations. The origin of this noise was identified to be the main power line of the laboratory: we measured an amplitude of 20 mG of this 50 Hz component around the vacuum chamber with a flux-gate sensor and a battery-driven oscilloscope. At the position of the ion, we measured a peak-peak amplitude of 6 mG from the shift of a quadrupole transition as a function of the starting time of the experiment in the phase of the AC-power cycle.

As this magnetic field instability limited the qubit’s coherence time (sec. 5.7) and the efficiency of sideband cooling, we installed a commercial system (Spicer) that partially compensates the 50 Hz noise component. This system consists of three flux-gate

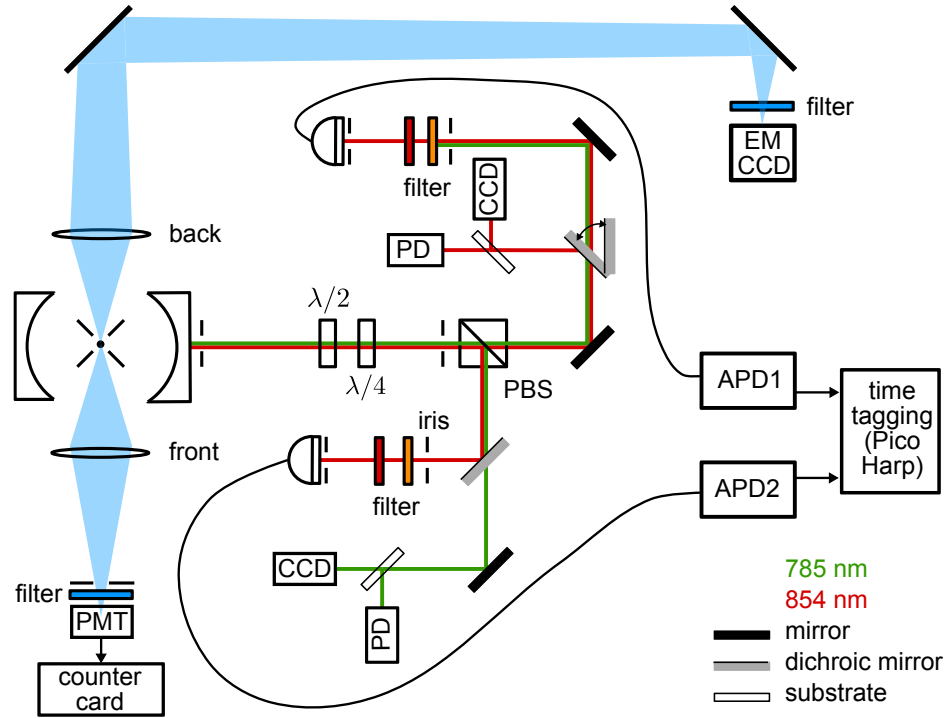


Figure 4.6: Detection of atomic fluorescence and cavity-photon polarization. Two objectives at the front and back side of the chamber collect the ion's fluorescence photons at 397 nm. At the back side, an image is produced on an EM-CCD camera. On the front side, the light is detected by a PMT, used for atomic state detection. Asymmetric cavity mirror transmissions define an output port of the trap cavity for photons at 854 nm produced in the Raman process. The polarization detection setup consists of a half-, a quarter-waveplate and a polarizing beamsplitter (PBS). After the PBS, photons are coupled to multi-mode fibers and detected by two APDs. Two filters and irises before each fiber block light at 785 nm used for the cavity lock and ambient stray light. Two pairs of CCD cameras and photodiodes (PD) monitor the cavity's spatial modes and transmission of the 854 nm and 785 nm light.

sensors measuring the 50 Hz noise component outside of the vacuum chamber in three dimensions. Feedback currents are provided to three cables mounted in a cube configuration around the entire setup. This compensation system decreases the magnetic field fluctuations at the position of the ion to 1.3 mG, increasing both coherence times and sideband cooling efficiencies (sec. 5.6).

4.9 Atomic fluorescence detection

The ion's fluorescence at 397 nm and 393 nm is detected by a photomultiplier tube (PMT) and an electron-multiplying charged-coupled device camera (EM-CCD). Only the PMT signal is used for state detection of a single ion (sec. 5.4).

Two objectives collect fluorescence photons from the ion at two large viewports at the front and back side of the vacuum chamber (fig. 4.6). On the front side, a photographic Nikon objective with an aperture diameter of 50 mm and a working distance of about 55 mm produces an image of the ion with a magnification of around 7. A slit aperture consisting of four adjustable blades blocks stray light caused by scatter of the laser off the trap electrodes. Background light at all wavelengths is attenuated by an interference filter⁵ after the aperture.

Assuming a uniform spatial distribution, the objective collects maximally 6.6% of the scattered light from the ion. Taking into account the PMT quantum efficiency of 26.5%, the overall maximum detection efficiency is 1.8% at 397 nm [65].

On the back side of the chamber, we use a custom-made objective (Sill Optics) with an aperture diameter of 38 mm at a working distance of 58 mm that images the ion on the EMCCD camera⁶ with a magnification of about 23. Background light again is attenuated by an interference filter⁷. We use the CCD camera for adjusting the cavity position with respect to the ion, for measuring the cavity waist in which we translate a single ion through the waist of the cavity mode (sec. 6.2), and for monitoring ion number during loading.

4.10 Photon state detection

This thesis describes a quantum interface employing the ion's electronic state as stationary qubit and the photon's polarization degree of freedom as flying qubit. To readout the flying qubit, we measure the photon's polarization state via quantum state tomography [108]. For this purpose, we use a half-waveplate, a quarter-waveplate and a polarizing beamsplitter (PBS) at the cavity output.

In previous work on our experimental setup [65, 85], experiments did not rely on a precise distinction of the cavity-photon polarization. The detection setup for cavity photons then employed dichroic mirrors at 45°, angles in order to separate the few photons emitted by the ion at 854 or 866 nm from the many photons sent through the cavity at 785 nm for its stabilization (sec. 4.5). We observe that these dichroic mirrors exhibit birefringence and polarization-dependent losses of about 4% at 854 nm at an angle of 45°, equivalent to non-unitary (and thus unwanted) operations on the photonic qubit. For the ion-photon entanglement and state mapping experiments, polarization

⁵Semrock FF01-377/50-25

⁶Andor iXon DV860AC-BV, pixel size $24\mu\text{m} \times 24\mu\text{m}$

⁷Semrock FF01-390/18-25

has to be measured with high precision so as not to limit state and process fidelities. We have therefore changed the cavity output path setup such that the waveplates and the PBS are the first optical elements in the cavity output path (fig. 4.6), allowing for precise polarization analysis. After the PBS, however, dichroic mirrors can be placed without drawbacks in order to monitor the cavity spatial modes at 854 nm and 785 nm on a CCD camera. Here, any losses in the dichroic mirror may at most result in slightly different PBS output-path efficiencies. Asymmetric path efficiencies, however, do not affect state fidelities as we compensate for this in the measurements (sec. 8.4).

The basis of photon detection is set by the angles of the half- and quarter-waveplates, mounted on motorized rotation stages⁸. The precision of polarization detection depends on the alignment of the angles under which waveplates and PBS are mounted with respect to the incoming beam. These angles are determined in the following calibration measurement.

In order to define a linear polarization, we use a Glan-Thompson polarizer (GTP) at the output of the cavity. We send an alignment beam at 854 nm through the trap cavity and align the PBS with respect to this beam in a first step. In a second step, we place the half-waveplate in front of the PBS and determine the rotation angles that correspond to a certain measurement basis (table 8.1). For the half-waveplate at 0° and 45° , the probe light is polarized along one of the axes of the PBS, and all light is expected to be either transmitted or reflected by PBS. In this case, we obtain an extinction of $2.7 \cdot 10^{-4}$ in transmission and $2.2 \cdot 10^{-3}$ in reflection from the PBS. At angles of $\pm 22.5^\circ$, the probe light should have diagonal/anti-diagonal polarization, and the ratio of transmission and reflection should be one. Here, the ratio of the two output ports is measured to be 99.0%. In a third step, we introduce the quarter-waveplate in front of the PBS and calibrate its angles. At an angle of 0° , we again expect no change to the polarization and measure an extinction of $3.2 \cdot 10^{-3}$.

At this stage, the polarization analysis setup is calibrated with respect to the GTP. In order to analyze the polarization of photons emitted in the cavity by the ion, we drive a Raman transition that generates photons of known polarization (sec. 7.2) with respect to the magnetic field that defines our quantization axis. We then adjust the offset angle of the half-waveplate such that we detect photons only at one output of the PBS. Now both waveplates and the PBS are calibrated with respect to the trap cavity and the quantization axis.

At both output ports of the PBS, photons are coupled to multi-mode fibers and detected by fiber-coupled avalanche photodiodes (APDs). In order to filter cavity photons at 854 nm from the transfer-lock light at 785 nm and ambient stray light at all wavelengths, we use a combination of a 30 nm narrow-bandpass interference filter⁹

⁸OWIS PS10-SM

⁹AHF Analysetechnik ET 850/30: center wavelength of 850 nm with a measured transmission of 98.3% at 854 nm.

and a long-pass edge filter¹⁰ at both fiber inputs. The efficiency of the optical paths from the PBS to the APDs is measured to be $\eta_{\text{path}} = (80 \pm 5)\%$.

Until last year, we used two APD modules from Perkin-Elmer (SPCM-AQR-15), exhibiting a dark count rate of about 30 Hz and a detection efficiency of $\eta_{\text{APD}_1} = (46 \pm 4)\%$. As the signal count rate for the ion-photon entanglement and state mapping experiments is about 40 Hz, dark counts of the detectors on the same order of magnitude present a limitation to the fidelities of these schemes. For the ion-photon entanglement experiment, we therefore exchanged one of the APDs with a new module from Laser-Components (COUNT-20C-FC), featuring a measured dark count rate of only 1.5 Hz and a detection efficiency of $\eta_{\text{APD}_2} = (34 \pm 3)\%$. The temporal resolution of the module is specified to 800 ps and its dead time to (62 ± 2) ns. As the parameters of this new module proved to be stable over time, we acquired a second module, which currently has a dark count rate of 3 Hz. At a time delay of 50 ns after photon impact, the APD module sends a 25 ns wide TTL signal of 3 V at 50 Ω load, recorded with a time tag by dedicated hardware (Picoquant PicoHarp) with a temporal resolution of 4 ps.

The detection probability of cavity photons is composed of the probabilities to leave the cavity (p_{out}), to traverse all optical elements to the APD (η_{path}), and to produce a photoelectric detection event at the APD (η_{APD}). We measure these components individually via a probe laser beam at 854 nm. The optical path efficiency $\eta_{\text{path}} = (80 \pm 2)\%$ is measured via coupling the probe beam to the cavity and measuring the beam's intensity directly after the cavity and after the multi-mode fibers with the same photodiode. The detection efficiency η_{APD} of both APDs is determined via overlapping the probe beam with the cavity-output mode and measuring its intensity with a calibrated power-meter. The beam is then attenuated by a stack of calibrated neutral density filters reducing the intensity by $3 \cdot 10^{-8}$. The resulting count rate of the APDs in the 10 – 100 kHz range reveals their detection efficiencies η_{APD} . The probability to detect a photon that has left the cavity is given by

$$\eta_{\text{det}} = \eta_{\text{path}} \cdot \frac{\eta_{\text{APD}_1} + \eta_{\text{APD}_2}}{2} = (32 \pm 3)\% \quad (4.5)$$

if we neglect absorption in the vacuum window, the waveplates and the PBS. The probability that a photon leaves the cavity through the output coupling mirror is given by

$$p_{\text{out}} = \frac{\mathcal{T}_2}{\mathcal{T}_1 + \mathcal{T}_2 + \mathcal{L}} = \mathcal{T}_1 \cdot \frac{\mathcal{F}}{2\pi}, \quad (4.6)$$

where \mathcal{L} are the combined losses due to scattering and absorption in the mirror coatings. Inserting the values of [65] into eq. 4.6, the output coupling probability is $(16 \pm 1)\%$. The probability p_{det} to detect a photon that the ion emits into the cavity, given by $p_{\text{det}} = p_{\text{out}} \cdot \eta_{\text{det}}$, is $(5.1 \pm 0.5)\%$. In our experiments, in which single photons

¹⁰Semrock Edge Basic 785 LP: 99.2% transmission at 854 nm, OD 6 at 610-790 nm

are generated with near-unit efficiency (as confirmed by simulations), we measure a detection probability of $(6.1 \pm 0.7)\%$. We therefore conclude that the value for p_{out} given in [65] is too small since it corresponds to a photon generation efficiency greater than one (where we confirm in separate measurements that we generate at most one photon at a time). From the measured detection probability of $(6.1 \pm 0.7)\%$, we instead calculate a value of the output coupling probability of $p_{\text{out}} = (19 \pm 3)\%$.

4.11 Radiofrequency generation and data acquisition

Coherent manipulation of the atomic qubit relies on the application of laser pulses with well controlled amplitude, length and phase. As laser pulses are generated with AOMs, control over all parameters of the laser pulses is obtained via the parameters of the radio frequency (RF) applied to the AOMs. For the generation of phase-coherent RF pulses with controlled phase and amplitude, a pulse sequencer was developed by Paul Pham and Philipp Schindler [109, 110]. It uses a field-programmable gate array (FPGA) to control direct digital synthesizer (DDS) boards that each generate up to 16 different frequencies in the range of 0-300 MHz with resolution of 0.2 Hz. The DDS allows for switching the phase of each pulse within one sequence, while the shape of the pulse is controlled by a variable gain amplifier. In our experiment, all pulses at 393 nm and 729 nm are generated by a pulse sequencer containing two DDS boards. To ensure phase coherence of these pulses, all DDS boards and additional RF sources are referenced to a 10 MHz quartz oscillator connected to the global positioning system (GPS).

Laser pulses at the other wavelengths, where no phase coherence is needed, are controlled with high timing precision by the FPGA that switches 16 logic channels (TTL) within the sequence. Two of these channels are used to trigger the PMT for atomic state detection and the APDs for photon detection. The FPGA is connected to a control PC via an ethernet connection and is programmed via a Python server. The execution of an experimental sequence is triggered via one of 8 input channels of the FPGA. This trigger signal and further analog signals controlling power and frequency of the remaining lasers are generated by two National Instruments cards of the control PC.

While the PMT signal is acquired on a counter card of the control PC, the signals from the APDs are time tagged by the PicoHarp module connected to the control PC via a universal serial bus. Additionally, a TTL trigger signal from the FPGA to the PicoHarp module is time-tagged during the same sequence. In this way, the time duration between the start of an experimental sequence and a single-photon event can be calculated, allowing for time-resolved analysis of the single-photon data, as explained in sec. 8.6.

Furthermore, the control computer is connected via a controller-area network bus to the high-voltage source that controls the voltages of tip and micromotion compensation

electrodes (sec. 4.2).

4.12 Technical considerations for a new setup

The design of the vacuum chamber containing ion trap and cavity has proven to be successful in a number of measurements that have been carried out since its construction. In most aspects, the setup was well arranged and leaves a lot of scope for new developments outside the vacuum chamber. Nevertheless, we have noted a few minor design flaws that should be considered in the construction of any new experimental apparatus.

As already mentioned in [65], the biggest limitation of the apparatus is the instability of the oven. Its thermal contact with the cavity mount prevents loading of ions when the cavity is adjusted to the best position with respect to the trap. In order to load an ion, we thus have to displace the cavity to break the thermal contact. This translation via the slip-stick piezo stages is not reproducible, so that we have to realign the cavity position after each loading procedure. Moreover, the cavity mount is heated during loading due to a residual thermal contact with the oven. After the loading procedure, the cavity thus thermally drifts both in length and position with respect to the ion while cooling and can only be realigned about one hour after loading. Fortunately, the mean trapping time of an ion is around one day, leaving enough time for measurements after loading and cavity alignment.

The time-intensive cavity-alignment procedure is described in [65]. In order to simplify this procedure, one could measure the absolute displacement of the cavity with a laser interferometer. Additionally, we could then calibrate the cavity translation in the direction orthogonal both to trap and cavity axis. Such calibration would allow for a measurement of the cavity waist in this direction, analogous to the measurement in the trap axis direction presented in sec. 6.2. In an attempt with a commercial interferometer (SIOS), however, it turned out that the metallic surfaces of the cavity holder do not reflect enough light for the interferometer to work reliably. Small metallic mirrors placed on the side of the cavity mount could enable this approach.

Although the slow piezo is mounted at a distance of about 1 cm from the ion, a change of its voltage by more than 10 V results in a measurable increase of excess micromotion. As we have experienced that excess micromotion can lead to reduced ion-cavity coupling, we avoid changing the voltage of the slow piezo. Instead, we position the cavity standing wave with respect to the ion via the slip-stick piezo translation stage that displaces the entire cavity mount. Although the cavity frequency typically stays in lock for small translations of the slip-stick piezo, this procedure only places the ion at an antinode after a time-intensive optimization process of random displacement steps. A more direct and precise positioning via the slow piezo is desirable, but would require better shielding of the electric fields emerging from the slow and fast piezos.

5 Atomic qubit

An ion-photon interface requires a number of experimental techniques to control the atomic qubit. Besides laser cooling of the ion, these techniques include the initialization, coherent manipulation and detection of the atomic qubit's quantum state. While first steps towards coherent control over the atomic qubit in our setup have been described in the thesis of Helena Barros [85], these techniques have been further improved over the past few years. Additionally, the magnetic field stability has been enhanced such that the atomic coherence time is large compared to the time required for the state transfer between atom and photon.

This chapter reports on these improved techniques that are fundamental for the ion-photon entanglement and ion-photon state mapping. Here, we focus on specific aspects in our setup, while a detailed review of the techniques for state control and measurement of ions can be found in [42, 43, 104].

5.1 Experimental sequence

All experiments described in this thesis are performed via the repetition of a sequence of laser pulses. Such a sequence consists of pulses for state initialization, the specific experiment and state detection, as sketched in fig. 5.1. For example, the specific experiment consists of a Raman pulse at 393 nm if the aim of the experiment is to generate a photon in the cavity. For other purposes, such as spectroscopy on the $S_{1/2} \leftrightarrow D_{5/2}$ transition, a sequence 729 nm laser pulses takes the place of the 393 nm pulse. In an experiment where we only read out the state of the ion, the whole sequence (1-8 in fig. 5.1) is typically repeated 50-250 times. If we have to read out the state of the photon, many more repetitions are necessary as only $(6.1 \pm 0.7)\%$ of the photons are detected (see sec. 8.4). The experimental details of all sequence steps such as Doppler cooling, state initialization, coherent manipulation and state detection will be discussed in the following sections.

5.2 Doppler cooling

Laser cooling of atoms and ions is a well established experimental tool in atomic physics today [111–113]. A laser that is red-detuned with respect to an atom's resonance provides a cooling force acting on the atom because of the Doppler effect. At steady state, this cooling process is counteracted by spontaneously emitted photons which lead to diffusion, resulting in a cooling limit. At the optimal laser detuning of $\Delta =$

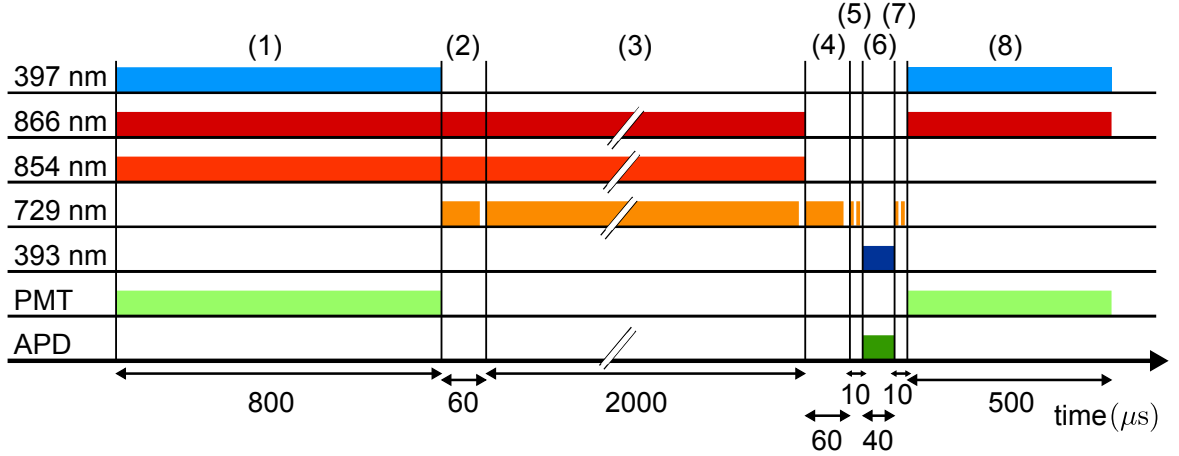


Figure 5.1: Typical sequence of pulses for each realization of the experiment (time not to scale). (1) Doppler cooling at 397 nm and 866 nm. The 854 nm laser repumps the $D_{5/2}$ population of the previous run of the sequence. (2) Optical pumping with the 729 nm laser. (3) Sideband cooling (optional). (4) Additional optical pumping (during sideband cooling, population may be transferred to the wrong $S_{1/2}$ state). (5) State initialization. A sequence of 729 nm pulses typically prepares $|S_{1/2, +\frac{1}{2}}\rangle$, $|S_{1/2, -\frac{1}{2}}\rangle$ or a superposition of both. (6) The specific experiment (see text). (7) Coherent rotations with the 729 nm laser set the measurement basis of the ion. (8) Fluorescence detection at 397 nm and 866 nm.

$-\Gamma/2$, this Doppler limit for a two-level atom is given by [104]

$$k_B T_{\min} = \frac{\hbar\Gamma}{2}. \quad (5.1)$$

In $^{40}\text{Ca}^+$, the linewidth of the $S_{1/2} \leftrightarrow P_{1/2}$ transition of $\Gamma = 20.7$ MHz [76, 78] results in a Doppler limit of $T_{\min} = 0.8$ mK, where the influence of the $P_{1/2} \leftrightarrow D_{3/2}$ transition to the cooling process has been neglected due to the low branching ratio of 7.5% [78].

To achieve a low Doppler limit in $^{40}\text{Ca}^+$, the Rabi frequency of the 397 nm beam is set to half of the value at saturation [104]. It is red-detuned from resonance by half the linewidth. A repump beam at 866 nm with σ^+/σ^- -polarization repumps all $D_{3/2}$ states. The power of this repump beam is set below saturation in order to avoid power broadening, which would increase the temperature of the Doppler limit. The repump beam is blue-detuned by ~ 1 MHz to avoid coherent population trapping [114].

In order to cool all three normal modes of the ion in the trap, the propagation axis of the cooling beam has to have a non-vanishing projection along all normal modes. Although the cooling beam installed in the early stage of our experimental setup was intended to fulfill this requirement (see fig 4.5, cooling beam in the x-y plane), the temperature of the ion along the direction of the cavity axis was found to be higher (well above the Doppler limit) than the temperature orthogonal to the cavity axis after Doppler cooling.

As the cooling beam has very similar projections on all trap electrodes, this asymmetry in cooling of the radial modes can only be explained by a rotation of the radial modes with respect to the electrodes. We therefore investigate the Doppler cooling of the radial modes and their direction by a detailed measurement of their mean phonon number. For this measurement, we apply two cooling beams at 397 nm and two analysis beams at 729 nm in the x-y and x-z plane (fig. 4.5). A first measurement of Rabi oscillations on one selected carrier calibrates the Rabi frequencies Ω_0^i of the two 729 nm beams. We then measure the onset of excitation on the blue sidebands for each of the four combinations of cooling and analysis beams. For short times, we approximate the excited state population ρ_{DD} of [104] for $\Omega_0 t \ll 1$

$$\rho_{DD}(t) = \sum_{n=0}^{\infty} p_n \sin^2(\eta\sqrt{n+1}\Omega_0 t) \approx (\bar{n} + 1)(\eta\Omega_0 t)^2, \quad (5.2)$$

with p_n the population of the harmonic oscillator state with phonon number n , Ω_0 the Rabi frequency of the carrier, and the Lamb-Dicke parameter η . From a quadratic fit of the excitation in all four measurements, we extract the Lamb-Dicke parameters η_i of the analysis beams and the mean phonon numbers \bar{n}_i of all three modes for each cooling beam. From the Lamb-Dicke parameters, we extract a rotation angle of 20-25° between the radial modes and the trap electrodes.

The small projection of the primary 397 nm beam on the radial mode along the cavity axis explains the weak direct cooling efficiency of this mode. In principle, both radial modes should be cooled equally if they exchange energy many times during the cooling interval. Although the frequency splitting of the two radial modes in our trap of 46 kHz (at an RF drive power of 5 W) is much larger than the inverse of the typical Doppler cooling time of 500 μ s, this process does not result in effective cooling of both modes.

We have therefore installed a second beam at 397 nm (fig. 4.5, cooling beam in the x-z plane) whose \vec{k} -vector has a large projection along the second radial mode. As the two cooling beams originate from the same laser and the same order of an AOM, they have the same frequency and interfere at the position of the ion. Interferometric stability between the two optical paths to the ion would thus be required for a stable cooling rate. We circumvent this requirement by setting the polarization of the two beams to be orthogonal in order to avoid interference. With this setting, all three modes of motion are cooled near the Doppler limit.

The improved Doppler cooling represents a substantial advance for our experiment. Not only did the imperfect cooling limit the fidelity of the coherent manipulation on the $S_{1/2} \leftrightarrow D_{5/2}$ transition in the past, but also does the temperature of the ion determine its localization in the cavity's standing wave and therefore the effective coupling g between ion and the cavity mode. The improvement of this localization gained with the new Doppler cooling setting will be described in detail in sec. 6.1.

5.3 State initialization

After the Doppler cooling interval (sec. 5.2), all population is distributed across both states of the $S_{1/2}$ manifold. Optical pumping is then applied in order to transfer all population into one of the $S_{1/2}$ states. Two methods for optical pumping are used in our setup.

In the first method, a σ^+ -polarized beam at 397 nm, propagating along the magnetic field axis, continuously transfers population from the $|S_{1/2}, -\frac{1}{2}\rangle$ to the $|P_{1/2}, +\frac{1}{2}\rangle$ state, while a repump laser at 866 nm repumps all $D_{3/2}$ states. As a consequence, all population is collected in the $|S_{1/2}, +\frac{1}{2}\rangle$ state, which is not coupled to any field. This first method provides fast optical pumping with an efficiency greater than 99% in 50 μ s. However, it relies on a beam along the magnetic field axis. This beam thus has to be realigned every time the magnetic field axis is changed as for the measurement of ion-photon state mapping described in chapter 9. Furthermore, the quality of this polarization-selective method is limited by the degree of circular polarization at 397 nm one is able to obtain.

As an alternative approach that does not rely on a beam along the magnetic field direction and is insensitive against polarization imperfections, we perform frequency-selective optical pumping on the narrow quadrupole transition. In this second method, we drive the transition from $|S_{1/2}, -\frac{1}{2}\rangle$ to $|D_{5/2}, +\frac{3}{2}\rangle$ in order to pump out the $|S_{1/2}, -\frac{1}{2}\rangle$ state. Subsequently, the $P_{3/2} \leftrightarrow D_{5/2}$ transition is used to pump out the $|D_{5/2}, +\frac{3}{2}\rangle$ state to the $P_{3/2}$ manifold, from which the population decays to both $S_{1/2}$ states. Population again accumulates in the $|S_{1/2}, +\frac{1}{2}\rangle$ state, which remains uncoupled. In this method, both fields can be applied either continuously or in a pulsed manner, in which a pulse at 729 nm is followed by a pulse at 854 nm and 866 nm, a sequence that is repeated several times. In the continuous scheme, the Rabi frequency of the repump on the $P_{3/2} \leftrightarrow D_{5/2}$ transition has to match the Rabi frequency of the drive field on the quadrupole transition in order to efficiently depopulate the $D_{5/2}$ state. In contrast, the pulsed scheme reaches a similar pumping rate but allows for an independent repump intensity and is therefore more robust to intensity fluctuations. With this second method, the efficiency of optical pumping exceeds 99% after 5 repetitions lasting in total 60 μ s. In our setup, we typically use the pulsed scheme of the frequency-resolved optical pumping on the quadrupole transition as it results in an efficient and robust situation independent of the magnetic field direction. This frequency-resolved method is only limited by off-resonant excitations and the pumping time. Keeping the Rabi frequency sufficiently low and applying the optical pumping for 1 ms, initialization fidelities exceeding 99.9% have been observed [72].

After optical pumping into either of the two $S_{1/2}$ Zeeman states, additional pulses on $S_{1/2} \leftrightarrow D_{5/2}$ transitions may be applied in order to generate a superposition of the two $S_{1/2}$ states, e.g., for ion-photon state mapping (chapter 9).

5.4 State detection

In contrast with single photons, single atoms can be detected with very high efficiencies as they scatter many fluorescence photons. For neutral atoms, however, scattered photons can induce heating on the order of the trap depth [44]. Reloading of atoms then decreases the repetition rate of the experiment. State of the art fidelities for nondestructive fluorescence methods of neutral atoms are 95% in an optical lattice [44] and 98.6% in an optical tweezer [45], both with loss rates on the order of 1%.

Ions, in contrast, can be measured without losses due to the large trap depths. In $^{40}\text{Ca}^+$, the fluorescence technique enables discrimination between the $S_{1/2}$ and $D_{5/2}$ states with fidelities exceeding 99% [43]. During the detection interval, both lasers at 397 nm and 866 nm illuminate the ion. The intensity of the 397 nm beam is set at saturation while the detuning and intensity of the 866 nm beam are the same as for Doppler cooling (sec. 5.2). If the ion is projected to the $S_{1/2}$ state, fluorescence photons at 397 nm are detected, while only background photons due to stray light and dark counts are detected if it is projected to the $D_{5/2}$ state. As all measurements in this thesis are carried out with a single ion, state detection is implemented via the PMT signal. Both fluorescence and dark counts follow a Poissonian photon count distribution; we discriminate between the two cases by defining a detection threshold. In fig. 5.2, the photon count distribution is shown for the results of the entanglement data of chapter 8. Here, the qubit is initially comprised of a superposition of two $D_{5/2}$ states, which is transferred to a superposition between $S_{1/2}$ and $D_{5/2}$ via a π pulse on the $S_{1/2} \leftrightarrow D_{5/2}$ transition as described in section 8.5.

The error rate of state readout depends on the overlap of the two count distributions and the probability of decay from $D_{5/2}$ to $S_{1/2}$. For a given signal to noise ratio, this overlap vanishes with increasing detection time. If the finite lifetime of the $D_{5/2}$ state is neglected, one could thus obtain an arbitrarily small detection error by simply increasing the detection time. In such a simplified model, the error is estimated by integrating the probabilities of detecting a number of counts below (above) the threshold although the ion was bright (dark) respectively: $\int_0^{n_t} \frac{\lambda_{\text{bright}}}{k!} e^{-\lambda_{\text{bright}}} dk + \int_{n_t}^{\infty} \frac{\lambda_{\text{dark}}}{k!} e^{-\lambda_{\text{dark}}} dk$, where $\lambda_{\text{bright,dark}}$ is the mean number of counts of the Poissonian probability distributions and n_t is the detection threshold. In our setup, we typically obtain a mean fluorescence rate of 50 kHz on the PMT, while the dark count rate remains below 1 kHz. At this signal to noise ratio, with a detection time of 500 μs and the detection threshold at 6.5 counts, the detection error would yield a value on the order of 10^{-5} . On this scale, however, the $D_{5/2}$ state's finite lifetime of 1.168 s has to be taken into account. For the detection time of 500 μs , we then estimate a detection error below $1 \cdot 10^{-3}$. This error is limited by events in which the initial $D_{5/2}$ state decays to the $S_{1/2}$ state during the detection time of 500 μs . This error could be reduced by making use of the arrival time information of the photons at the PMT [115]. For our purpose, however, the photon-count histogram method is sufficient as the detection error of $1 \cdot 10^{-3}$ falls below other experimental imperfections of ion-photon entanglement and state-mapping

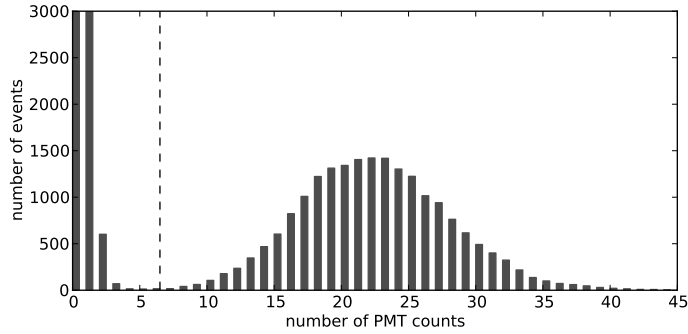


Figure 5.2: Histogram of PMT counts containing $\sim 40,000$ events of one complete state tomography for ion-photon entanglement measurement (chapter 8). Here, we chose a detection time of $500 \mu\text{s}$ and a detection threshold at 6 counts. The number of events in the first two bins are 15,000 and 4,000 (the y-axis is truncated at 3,000).

and does not limit its fidelities.

5.5 Coherent manipulation of the atomic qubit

In order to demonstrate coherent transfer between one $S_{1/2}$ state and one $D_{5/2}$ state, we drive Rabi oscillations between states $|S_{1/2}, +\frac{1}{2}\rangle$ and $|D_{5/2}, +\frac{5}{2}\rangle$. In fig. 5.3a, Doppler cooling is applied before the excitation of the quadrupole transition, while in fig. 5.3b, sideband cooling in all three dimensions is performed in addition to Doppler cooling. As the Rabi frequency on the carrier depends on the phonon number n to second order in the Lamb-Dicke parameter, a range of Rabi frequencies contributes to the oscillations [104]:

$$\rho_{DD}(t) = \frac{1}{2} \left[1 - \sum_{n=0}^{\infty} p_n \cos(\Omega_0(1 - \eta^2 n)t) \right]. \quad (5.3)$$

After Doppler cooling, states with a range of n values are occupied and the oscillations are damped. In contrast, after sideband cooling of all three vibrational modes ($\bar{n}_a = 0.04 \pm 0.03$, $\bar{n}_{r1} = 0.1 \pm 0.1$, $\bar{n}_{r2} = 1.0 \pm 0.4$), the oscillations have only one frequency component.

By a Rabi-frequency calibration of the required $S_{1/2} \leftrightarrow D_{5/2}$ transitions, the respective times for π and $\pi/2$ rotations are determined. Any optical $S - D$ qubit can then be transferred to any $S - S'$ or $D - D'$ spin qubit and vice-versa via π and $\pi/2$ pulses.

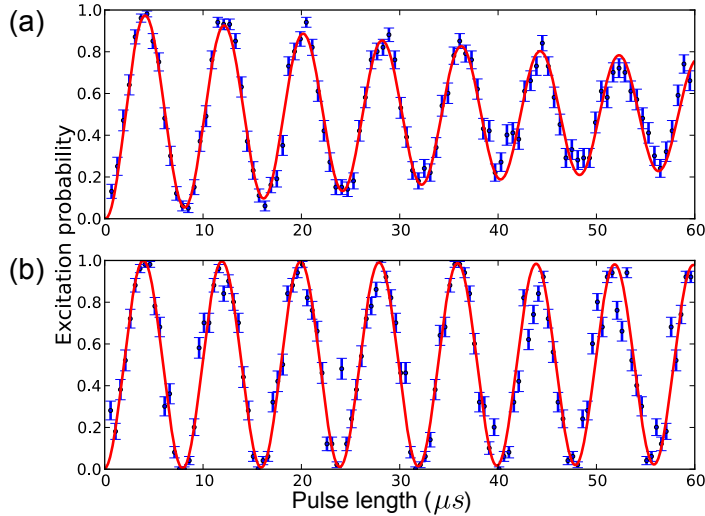


Figure 5.3: Rabi oscillations on the $S_{1/2} \leftrightarrow D_{5/2}$ quadrupole transition, driven at 729 nm. We plot the excitation probability of the $D_{5/2}$ state as a function of pulse length. **(a)** After Doppler cooling, a range of phonon number states are occupied. Different frequencies result in a damped oscillation. **(b)** Following axial and radial sideband cooling, only one frequency component contributes to the oscillation.

5.6 Sideband cooling

After Doppler cooling, the mean phonon numbers of the axial and radial modes are $\bar{n}_{\text{axial}} = 9.4$ and $\bar{n}_{\text{radial}} = 3.5$ at trap frequencies of $\omega_{\text{axial}} = (2\pi) 1.1$ MHz and $\omega_{\text{radial}} = (2\pi) 3$ MHz. In some experiments that use one common motional mode of the ion string as a bus for the Cirac-Zoller entangling gate [116], operation near the ground state of this mode is necessary. Although this requirement no longer holds for the Mølmer-Sørensen entangling gate [117], operation near the ground state still improves fidelities [118, 119]. In order to cool an ion's motion to the ground state, sideband cooling techniques are necessary [42].

In our setup, sideband cooling of a single ion is beneficial for several reasons. First of all, sideband cooling maximizes the Raman coupling of an individual ion on a carrier transition while reducing off-resonant scattering on sidebands, as will be described in sec. 7.3. Furthermore, experiments involving entangling gates between two ions are planned in the near future (chapter 10). For these experiments, operation near the ground state of the axial common mode will be advantageous both for entanglement and for cavity-driven Raman transitions. Sideband cooling could in principle also be used to improve the coupling of the ion to the cavity mode by decreasing the spread of the ion's spatial wavefunction. However, the localization of the ion in the cavity's standing wave in our setup is limited by relative motion between the trap and cavity mount instead of the motion of the ion in the trap, as demonstrated in chapter 6. Finally, sideband cooling allows for a measurement of the heating rate of the ion trap,

an important characterization of the experimental setup.

Initial experiments involving sideband cooling in our setup are described in Helena Barros's thesis [85], in which a spectrum of one carrier with neighboring sidebands is shown in order to demonstrate the resolution and identification of all motional sidebands. Since the experiments in [85], the following technical advances have significantly improved both the sideband-cooling rate and the temperature after cooling in our setup: Doppler cooling as described in sec. 5.2, optical pumping with the 729 nm laser (sec. 5.3), improved current stabilization for the static magnetic field (sec. 4.8), and the installation of a commercial compensation system for AC magnetic field noise (5.7). We take advantage of these technical advances to cool to the ground state, investigate a pulsed scheme, and measure the heating rate of the trap.

For sideband cooling of $^{40}\text{Ca}^+$, a closed cooling cycle can be achieved by tuning the 729 nm laser to the red sideband of the $|S_{1/2}, +\frac{1}{2}\rangle$ to $|D_{5/2}, +\frac{5}{2}\rangle$ transition. Due to the long lifetime of the $D_{5/2}$ state, a repump laser at 854 nm continuously transfers population to the $|P_{3/2}, +\frac{3}{2}\rangle$ state, from which it decays to the initial state $|S_{1/2}, +\frac{1}{2}\rangle$, closing the cooling cycle. As the $P_{3/2}$ state also decays to the $D_{3/2}$ state with a small branching ratio of 0.7%, its population is repumped by the 866 nm laser to the $P_{1/2}$ state. Due to this repumping via the $P_{1/2}$ state, population can escape the cooling cycle into the $|S_{1/2}, -\frac{1}{2}\rangle$ state. Therefore, sideband cooling is interleaved with short optical pumping cycles, returning all population back to the cooling cycle.

The Rabi frequencies on the red and blue sideband are given by $\Omega_{\text{redSB}} = \Omega\eta\sqrt{\bar{n}}$ and $\Omega_{\text{blueSB}} = \Omega\eta\sqrt{\bar{n} + 1}$ [42], where the Lamb-Dicke parameter $\eta = \vec{k} \cdot \vec{e}_z \sqrt{\frac{\hbar}{2m\omega_z}}$ describes the ability of the field with wave-vector \vec{k} to couple to the harmonic motion of a particle with mass m along \vec{e}_z with frequency ω_z . Assuming a thermal distribution, the particle's mean phonon number \bar{n} can be deduced by a measurement of excitation probabilities p_{redSB} on the red and p_{blueSB} on the blue sideband of any motional mode [120]:

$$\bar{n} = \frac{p_{\text{redSB}}}{p_{\text{blueSB}} - p_{\text{redSB}}}. \quad (5.4)$$

Using this formula, we extract a mean phonon number of the axial mode of $\bar{n}_{\text{ax}} = 0.022 \pm 0.001$ after 6 ms of sideband cooling. Cooling this close to the ground state ($\bar{n} \ll 1$) is manifested by a vanishing red sideband as presented in [85] and by the ability to drive coherent Rabi oscillations on the blue sideband with one dominant Rabi frequency $\Omega_{\text{blueSB}} = \Omega\eta$ (fig. 5.4a).

Additionally, we investigate a pulsed sideband-cooling scheme in which the 729 nm laser and the 854 nm laser drive π -pulses instead of being applied continuously as described above. This pulsed scheme proves to be less sensitive to the Rabi frequency of the 854 nm laser but nevertheless results in the same cooling rate and final temperature as the continuous scheme. The pulsed scheme therefore presents itself as a robust cooling scheme for an experiment in which the 854 nm Rabi frequency has to be set for a different step in the sequence, e.g., the continuous drive of the Raman transition

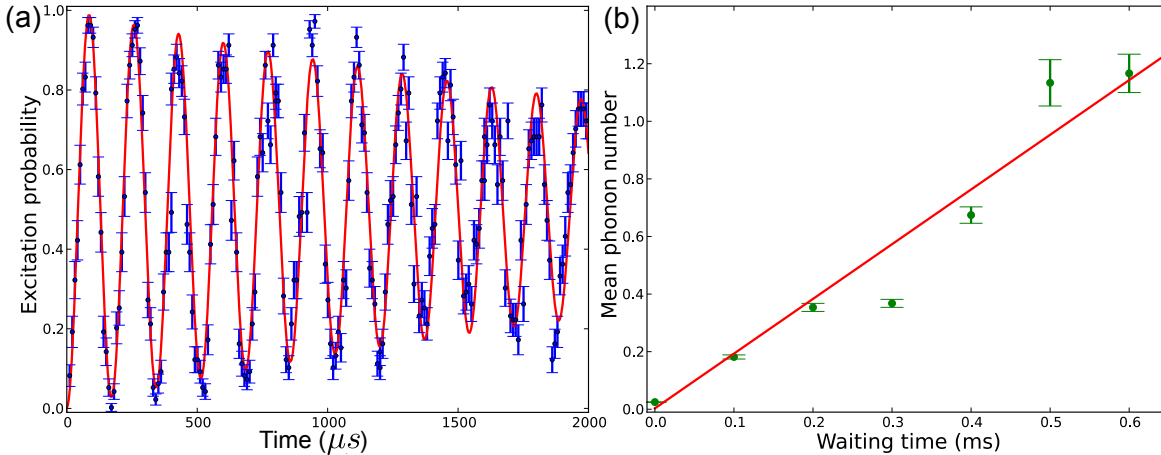


Figure 5.4: (a) Rabi oscillations on the blue axial sideband after 6 ms of sideband cooling. The dominant frequency is $\Omega\eta$, while the coherence of these oscillations is limited by the temperature of the radial modes, which are not sideband-cooled. (b) Heating rate measurement of the axial mode at $\omega_{\text{axial}} = (2\pi) 1.1$ MHz. After sideband cooling to a mean phonon number of $\bar{n}_{\text{axial}} = 0.022 \pm 0.001$, we vary the waiting time before a measurement of the excitation on the red and blue sidebands which allows us to extract the mean phonon number \bar{n} via eq. 5.4. Error bars represent one standard deviation based on projection noise in the excitation measurement. The fit reveals a heating rate of 1.9(2) motional quanta per second.

(sec. 7.2). Alternatively, using a continuous scheme, the 854 nm intensity must be switched between different values within the experimental sequence.

Finally, we take advantage of sideband cooling to measure the heating rate of our ion trap possessing an ion-electrode separation of 0.8 mm. For this purpose, we add a variable waiting time between sideband cooling and an excitation measurement on the sidebands and measure the mean phonon number for six different waiting times (fig 5.4b). A linear fit reveals a heating rate of one motional quantum in 500 ms. This value is very similar to the one observed in [56] for a similar trap architecture and represents one of the lowest ion-trap heating rates measured [90].

5.7 Atomic coherence time: Ramsey spectroscopy

As an atom in a cavity can act as a quantum memory in a network, it is essential to store information within it for extended times. We therefore investigate the coherence time of the atomic qubit via Ramsey spectroscopy [121].

As described in sec. 2.1.2, the length of a laser pulse on the quadrupole transition determines the angle of rotation on the Bloch sphere of the qubit. The phase of the pulse, on the other hand, determines the direction of the rotation axis, as demonstrated by a sequence of two $\pi/2$ pulses with different phase on the transi-

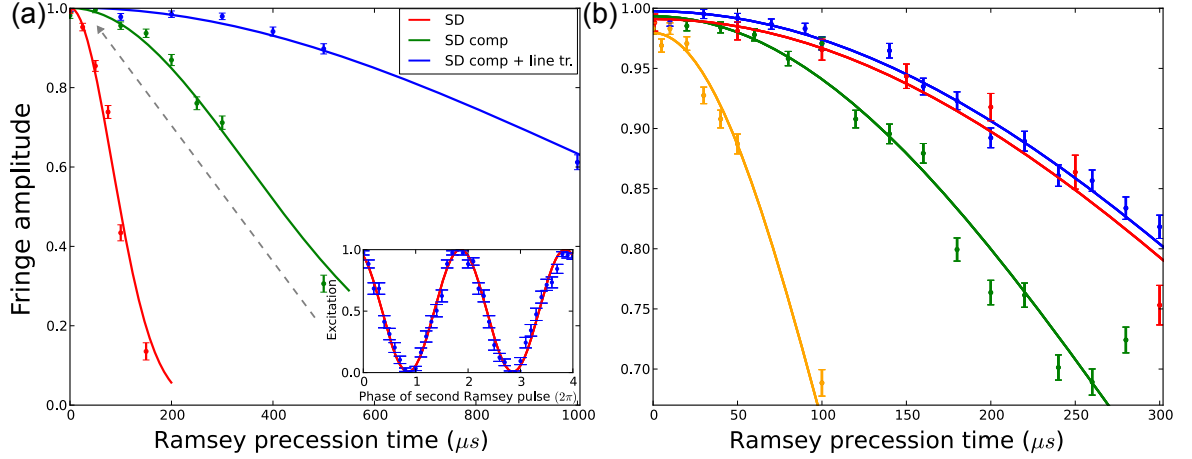


Figure 5.5: Atomic coherence time. **(a)** Ramsey spectroscopy demonstrating the AC magnetic field noise compensation. Red curve (SD): bare laboratory environment, coherence time $\tau_{\text{coh}} = 80 \mu\text{s}$. Green curve (SD comp): with active AC magnetic field noise compensation, $\tau_{\text{coh}} = 350 \mu\text{s}$. Blue curve (SD comp + line tr.): in addition to active compensation, each realization of the sequence is started at the same phase of the AC power cycle, $\tau_{\text{coh}} = 1 \text{ ms}$. All graphs represent measurements of an $|S_{1/2}, +\frac{1}{2}\rangle - |D_{5/2}, +\frac{3}{2}\rangle$ superposition. Each data point corresponds to a fitted Ramsey fringe as shown in the inset for a Ramsey time of $50 \mu\text{s}$. **(b)** Ramsey spectroscopy demonstrating the coherence time of different atomic qubits relevant for this thesis. Note that the fringe amplitude is plotted between 0.67 and 1. Green (yellow) curve: $S - S'$ spin qubit: $|D_{5/2}, -\frac{5}{2}\rangle, |D_{5/2}, -\frac{3}{2}\rangle$ with $\tau_{\text{coh}} = 110 \mu\text{s}$ ($D - D'$ spin qubit: $|S_{1/2}, +\frac{1}{2}\rangle, |S_{1/2}, -\frac{1}{2}\rangle$ with $\tau_{\text{coh}} = 300 \mu\text{s}$) for ion-photon entanglement (state mapping) and magnetic field in the diagonal (anti-diagonal) direction (orientation: see fig. 4.5). Red (blue) curve: $S - D$ optical qubit $|S_{1/2}, +\frac{1}{2}\rangle, |D_{5/2}, +\frac{3}{2}\rangle$, magnetic field in the diagonal (anti-diagonal) direction, both yielding a coherence time of $\tau_{\text{coh}} = 450 \mu\text{s}$. All experiments in this graph have been performed with active AC magnetic field noise compensation but without a trigger synchronized to the AC power cycle. This setting represents the typical measurement scenario in our setup. All curves of both plots are fitted with a Gaussian decay (see text).

tion $|S_{1/2}, +\frac{1}{2}\rangle \leftrightarrow |D_{5/2}, +\frac{3}{2}\rangle$. While the first $\pi/2$ pulse with phase ϕ_1 generates a superposition $\frac{1}{\sqrt{2}} (|S_{1/2}, +\frac{1}{2}\rangle + e^{i\phi_1} |D_{5/2}, +\frac{3}{2}\rangle)$, the phase ϕ_2 of the second $\pi/2$ pulse determines the axis of the second rotation with respect to the first one. A detection period at the end of the sequence discriminates between the states $|S_{1/2}, +\frac{1}{2}\rangle$ and $|D_{5/2}, +\frac{3}{2}\rangle$. In the ideal case, a scan of the phase ϕ_2 over a range 0 to 2π results in a Ramsey fringe with amplitude of 1, i.e., sinusoidal excitation of $|D_{5/2}, +\frac{3}{2}\rangle$ from 0 to 1. In the experiment, imperfections in optical pumping, intensity fluctuations, and the residual temperature of the ion slightly reduce the fringe amplitude. In our setup, a scan of the Ramsey phase ϕ_2 of two $\pi/2$ pulses separated by $50 \mu\text{s}$ reveals a fringe amplitude of $98.9 \pm 0.4\%$ (inset of fig. 5.5a).

During the time interval between the two pulses, the atom freely precesses at the frequency of the energy splitting $\omega = \Delta E/\hbar$ between the relevant states. As this energy splitting depends linearly on the magnetic field, a change in the field strength will cause a different precession frequency. Magnetic field fluctuations on the time scale of the 100-250 repetitions of the sequence (over which we average for a single data point) or faster will thus lead to a reduced fringe amplitude. The atomic decoherence mechanisms thus depend on the correlation time τ_c of the magnetic field fluctuations ΔB . Assuming the fluctuations to be a Gaussian process, the atomic coherence decays exponentially if τ_c is much smaller than the duration of a single realization of the sequence t_s , i.e., in the so-called Markovian regime ($\tau_c/t_s \ll 1$) [122]. In the static regime, where $\tau_c/t_s \gg 1$, however, the time dependence of the atomic coherence is described by a Gaussian decay.

We investigate the atomic coherence time and the time scale of magnetic field fluctuations by varying the time between the two Ramsey pulses. For each value of the precession time, a fringe is recorded and its amplitude fitted. In fig. 5.5a, the resulting fringe amplitude is plotted as a function of the precession time for different laboratory settings. For all curves, the initial decrease of the Ramsey contrast follows a Gaussian rather than an exponential decay. In our setup, the magnetic field thus fluctuates on a time scale of all 100-250 realizations of the sequence but stays rather constant during a single realization. Following the model for the fidelity of a state in the stationary regime [122], we fit the following function to the Ramsey amplitude A in order to extract a coherence time τ_{coh} for each curve of fig. 5.5:

$$A = A_0 \exp\left(-\frac{t^2}{2\tau_{\text{coh}}^2}\right), \quad (5.5)$$

where A_0 is the amplitude at precession time $t = 0$. For the bare laboratory environment, this fit yields a coherence time of only $80 \mu\text{s}$. With the active AC magnetic field noise compensation described in sec. 4.8, the coherence time is improved to $350 \mu\text{s}$. In addition, if we start the pulse sequence of each repetition of the measurement at the same phase of the AC power cycle, the coherence time reaches a value above 1 ms. This improvement demonstrates that 50 Hz fluctuations of the magnetic field, quanti-

fied by independent measurements with a fluxgate sensor (sec. 4.8), limit the atomic coherence time.

A typical sequence of ion-photon entanglement or ion-photon state mapping lasts 1.5-2 ms. Performing these experiments synchronized to the AC power cycle would reduce the experiment rate by one order of magnitude. As photon generation takes place on the time scale of 10-40 μs , over which the atomic coherence time remains high, it is not necessary to use this AC-power-cycle trigger in the ion-photon entanglement and state mapping experiments.

After identifying the main source of atomic decoherence via Ramsey spectroscopy on the $S - D$ optical qubit between $|S_{1/2}, +\frac{1}{2}\rangle$ and $|D_{5/2}, +\frac{3}{2}\rangle$, we now quantify the coherence time of the $D - D'$ spin qubit between $|D_{5/2}, -\frac{5}{2}\rangle$ and $|D_{5/2}, -\frac{3}{2}\rangle$ for ion-photon entanglement and the $S - S'$ spin qubit between $|S_{1/2}, +\frac{1}{2}\rangle$ and $|S_{1/2}, -\frac{1}{2}\rangle$ for ion-photon state mapping. We expect different coherence times of these qubits for two reasons. First, the different Landé factors of $g_{D_{5/2}} = 6/5$ and $g_{S_{1/2}} = 2$ result in different sensitivities to magnetic field fluctuations. Second, we apply different magnetic fields for the two experiments, differing both in amplitude and direction. In order to perform a Ramsey measurement on the spin qubits, we first prepare an equal superposition via a $\pi/2$ pulse on the $|S_{1/2}, -\frac{1}{2}\rangle \leftrightarrow |D_{5/2}, -\frac{3}{2}\rangle$ transition. Subsequently, we transfer one state to a different subspace via a π pulse on a second $S_{1/2} \leftrightarrow D_{5/2}$ transition. For the $S - S'$ spin qubit, we choose the $|S_{1/2}, -\frac{1}{2}\rangle \leftrightarrow |D_{5/2}, -\frac{3}{2}\rangle$ transition for the π pulse, while we choose $|S_{1/2}, +\frac{1}{2}\rangle \leftrightarrow |D_{5/2}, -\frac{5}{2}\rangle$ transition for the $D - D'$ spin qubit. After a variable precession time, the same pulse sequence is applied in the reverse order before state detection.

In fig. 5.5b, we plot the resulting Ramsey fringe amplitudes as a function of the waiting time. For the $D - D'$ qubit, we measure a coherence time of 300 μs . The initial contrast of $98.4 \pm 0.5\%$ stays constant within error bars for 40 μs , which is the time necessary for photon generation and setting the measurement basis of the atom (sec. 8.5). The $S - S'$ qubit, most sensitive to magnetic field noise, exhibits a coherence time of 110 μs . Here, the contrast starts at $98.3 \pm 0.5\%$ and decreases to $92.7 \pm 0.7\%$ within 30 μs , the maximum photon integration time for state mapping. For both qubits, the contrast at zero precession time is limited by imperfect pulses due to the residual temperature of the ion after Doppler cooling. With sideband cooling, the initial contrast approaches unity.

According to the ratio of Landé factors of $S_{1/2}$ and $D_{5/2}$, we expect a coherence time ratio of the two spin qubits of $(6/5)/2 = 0.6$. Instead, we measure a ratio of $\sim 1/3$. A possible reason for this discrepancy could be the different direction of the main magnetic field if the field fluctuations have a preferred direction. To investigate this hypothesis, we additionally determine the coherence time of the optical qubit for the two field orientations (fig. 5.5b). For the entanglement configuration, this measurement was taken on the same day as the measurement of the spin qubit. For the mapping configuration, the measurements were taken on different days. Although the initial Ramsey contrast is slightly higher for the entanglement setting (caused by

a different Lamb-Dicke parameter of the 729 nm beam (4.6)), we measure the same coherence time of 450 μs for both settings. The different field orientations thus do not result in different coherence times. Comparing the coherence times of the $D - D'$ and the $S - D$ qubit for the entanglement setting, measured at the same day, we obtain a ratio of $(304 \pm 3)/(457 \pm 9) = 0.67 \pm 0.01$, exactly matching the expected value of $(6/5 \cdot 3/2 - 1/2 \cdot 2)/(6/5) = 2/3$. We thus conclude that the difference in the measured coherence times indeed corresponds to the theoretically expected value and extract an amplitude of the fluctuations of $\sqrt{\Delta B^2} = 1/(\tau_{\text{coh}}\mu_B(g_D \cdot m_D - g_S \cdot m_S)) \approx 1.6$ mG. From the coherence time of the $S - S'$ qubit, measured on a day close to the state mapping measurement of chapter 9, we conclude that the magnetic field noise differed by a factor of 1.5 between the entanglement and the state mapping measurements. This change is probably caused by devices in neighboring laboratories connected to the same power line as observed with the magnetic-field fluxgate sensor (sec. 4.8).

Additional to magnetic field fluctuations, frequency noise of the laser can reduce the fringe contrast as it leads to a fluctuation of the rotation axis of the second pulse. In our experimental setup, however, the influence of laser frequency noise on the atomic coherence time is negligible as the linewidth of the 729 nm laser is smaller than 100 Hz, more than one order of magnitude below the corresponding frequency noise of the magnetic field of $\mu_B\sqrt{\Delta B^2} \approx 2$ kHz.

In conclusion, the atomic coherence time in our apparatus is limited by 50 Hz field noise present in the laboratory. The installation of a magnetic field noise cancellation system has increased the atomic coherence time in our setup by a factor of 4, sufficient to not limit the fidelity of the ion-photon entanglement and ion-photon state mapping experiments. The coherence time could be further improved by triggering each repetition of the sequence to the AC power cycle, but this would slow down the overall rate of photon generation. In other work, long coherence times in $^{40}\text{Ca}^+$ ions have been achieved by installing a μ -metal shield around the vacuum setup [122], by defining a qubit in the decoherence-free subspace of two entangled ions [71, 72, 123] or by defining a field-insensitive hyperfine qubit in the $^{43}\text{Ca}^+$ isotope [74].

5.8 Minimization of micromotion

Geometric imperfections of the Paul trap and stray charges on trap electrodes may cause an ion position different from the node of the AC field, resulting in an oscillation of the ion in the trap at the trap drive frequency. Such an oscillation is called micromotion and may cause first- and second- order Doppler shifts leading to decreased cooling efficiencies, AC Stark shifts in atomic transitions and reduced trapping times [124]. Micromotion can be compensated by applying static potentials to compensation electrodes [91]. For the detection of micromotion, various methods are described in [91, 104, 124].

In our setup, micromotion was minimized by several of these methods in previous

work [65, 85]. The most sensitive of these methods is frequency resolved sideband spectroscopy on the narrow $|S_{1/2}, -\frac{1}{2}\rangle \leftrightarrow |D_{5/2}, -\frac{5}{2}\rangle$ transition. Via a measurement of the Rabi frequency of the first order micromotion sideband Ω_1 with respect to the Rabi frequency Ω_0 of the carrier, one directly determines the modulation index β via $J_1(\beta)/J_0(\beta) = \Omega_1/\Omega_0$ in the low intensity limit [124]. Although most sensitive, this resolved sideband method requires three non-collinear beams for a compensation in all three directions. In the past, only one beam was used, which was sufficient in combination with the other methods for the experiments described in [65, 85]. At that stage, no particular source of micromotion for fixed trap settings was identified.

Only recently, we found that a change of the cavity-mirror's slow piezo voltage by more than 10 V may lead to a change of the ion's position in the trap and thus a measurable increase of micromotion. For the experiments reported in this work, we found that micromotion has to be minimized for controlling the position of the ion with respect to the standing wave of the cavity (sec. 6.1). Furthermore, in the case of uncompensated excess micromotion, micromotion sidebands appear in the Raman spectrum, as described in sec. 7.3. Those sidebands might overlap with carrier transitions and should be suppressed.

We have therefore installed three non-collinear beams at 729 nm (fig. 4.5) enabling micromotion detection in all directions. We adjust the voltage applied to the compensation electrodes in order to compensate micromotion in the radial plane. To compensate micromotion in the direction of the trap axis, we change the difference between the voltages applied to the two tip electrodes. Typical values of the compensation electrodes are 170 V and 240 V, while the tip electrodes at $V_{\text{top}} = 934$ V and $V_{\text{bottom}} = 866$ V. We typically obtain a ratio of the Rabi frequencies of the first-order micromotion sideband with respect to the carrier of $\Omega_1/\Omega_0 = 1/100$, corresponding to a modulation index of $\beta = 0.02$. The corresponding amplitude of micromotion is $\Delta_x = \beta(\lambda/2\pi) = 2.3$ nm [104], much smaller than the wavelength of the standing wave of the cavity field.

Unfortunately, every time an ion is loaded into the trap, the cavity has to be moved due to a thermal contact between the oven and the cavity holder (sec. 4.12). We thus have to realign the cavity position every time an ion is loaded. As the voltage of the piezos may change during this procedure, compensation of micromotion may also be necessary. If the ion position with minimal excess micromotion has changed, the height of the cavity has to be adjusted via the feedthrough [65] such that the center of the cavity mode overlaps with the ion position.

In summary, we have achieved Doppler and sideband cooling of all three motional modes of a single $^{40}\text{Ca}^+$ ion. We have demonstrated efficient initialization, coherent manipulation and detection of the atomic quantum state. Additionally, we have increased the atomic coherence time of the ion via active stabilization of the magnetic

field. The achieved coherence time is now long enough to not limit the measurements of ion-photon entanglement and state mapping. We have thus provided all necessary tools for the control of the stationary, atomic qubit. In the next two chapters, we discuss its coupling to the cavity, the second necessary element of an ion-photon interface.

6 Controlling the ion-cavity coupling

At the heart of our experiment lies the coupling of the ion to the cavity. In order to maximize the coupling strength, it is not enough to build a resonator with small mode volume. In addition, the ion's position in the resonator mode has to be controlled to a precision much better than the optical wavelength λ of the resonator mode. Although the spread of a laser-cooled ion's wavefunction is much smaller than λ due to the deep trapping potential of the Paul trap, it remains a technical challenge to control the relative position between ion and cavity mode on the same nanometer length scale.

A single ion has been used to probe the transverse-mode structure in a linear trap [46] and the longitudinal standing wave in a ring trap [47]. In this chapter, we present precise control over the ion-cavity position both in the direction of the standing wave and in the transverse direction, taking advantage of various displacement methods of the cavity and the ion in the linear Paul trap. These measurements were published in [52].

6.1 Localization in the standing wave

The maximum ion-cavity coupling strength g_0 given by the geometry of the cavity mode was discussed in sec. 4.3. Experimentally, one observes a value of the coupling strength $g_{\text{obs}} \leq g_0$ depending on the position of the ion with respect to the standing wave of the resonator [47]. We are able to adjust this relative position in all three dimensions by means of in-vacuum piezo stages and a feedthrough [48]. However, the position may vary on fast time scales due to both the temperature of the ion in the trap and center-of-mass vibrations of the cavity with respect to the trap. These relative vibrations can occur because cavity and trap are mounted separately and rigidly to the vacuum chamber [65]. In order to quantify the extent of relative motion, we perform two measurements.

In the first measurement, we observe the localization of the ion in the standing wave of the cavity by translating the cavity with respect to the ion. We tune the drive laser and the frequency-stabilized cavity to satisfy the Raman resonance condition for one of the transitions described in sec. 7.2, 400 MHz red-detuned from the $P_{3/2}$ excited state. After 2 ms of Doppler cooling the single ion, we apply the drive and repump laser simultaneously for 300 μs while detecting cavity photons at the APDs. By scanning the voltage on one cavity mirror's piezo stack while sending a Pound-Drever-Hall feedback signal to the other stack, we shift the cavity along its axis while keeping its length fixed. The range of this second piezo stack is approximately one cavity standing wave. As the position of the ion moves from an antinode to a node of

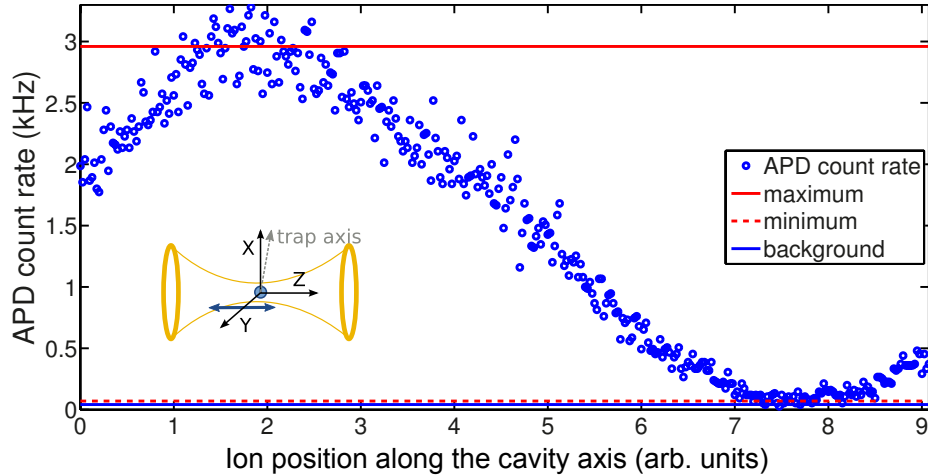


Figure 6.1: Translation of the cavity standing wave with respect to the ion. The ion-cavity system is driven on Raman resonance with the cavity, 400 MHz red-detuned from the transition at 393 nm; the number of 854 nm photons generated in the cavity depends on the ion-cavity coupling, which varies from maximum to minimum across the standing wave. The measurement sequence described in the text is recorded 250 times for each data point.

the cavity standing wave, the Raman coupling between the S and D states and thus the number of photons in the cavity changes from maximum to minimum, as seen in fig. 6.1. The visibility of this modulation, observed on the APDs, is $(98 \pm 2)\%$, corresponding to a localization of (13 ± 7) nm [125].

In comparison to our previously measured visibility of 60% [48], this result shows that we have been able to decrease the residual motion of the ion along the cavity axis to the point where our minimum signal is just above background. In [48], we incorrectly blamed an oscillation of the cavity mount with respect to the ion trap for the previously limited visibility. Instead, the improvement was accomplished by optimized Doppler cooling (sec. 5.2). We estimate the ion's spatial extension after Doppler cooling by $\sqrt{\bar{n}}x_0 \approx 17$ nm [125], where $x_0 = \sqrt{\frac{\hbar}{2m\omega_{\text{radial}}}} = 6.5$ nm is the spread of the ground state. As the measured localization of (13 ± 7) nm is on the order of this Doppler-cooling limit, we conclude that any relative motion of the cavity with respect to the trap in the direction of the standing wave is negligible.

6.2 Probing the radial structure of the cavity mode

In the second measurement, we translate the ion by changing the relative voltage of the tip electrodes, which shifts the trap minimum along the trap axis of symmetry. In this way, we can probe the radial structure of the TEM_{00} cavity mode, which we expect to have waist $w_0 = (13.2 \pm 0.8)$ μm (sec. 4.3). If relative motion orthogonal

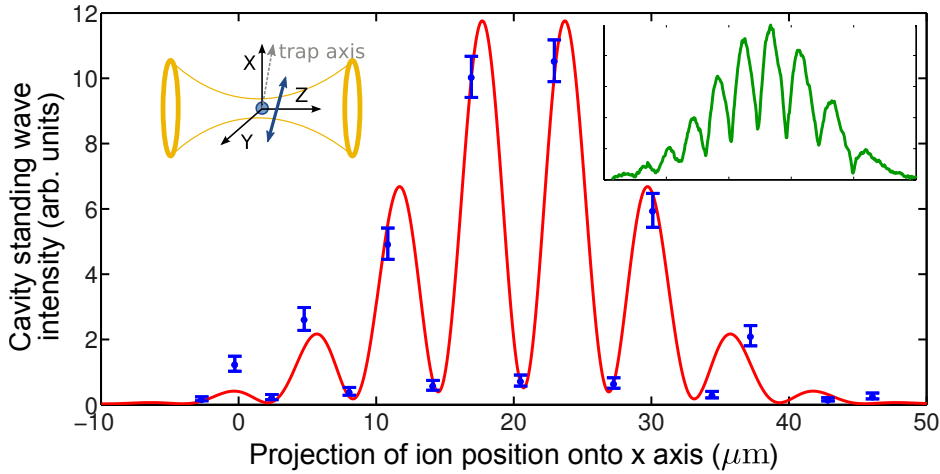


Figure 6.2: Translation of the ion along the trap axis of symmetry, which is nearly orthogonal to the cavity. The ion is driven with the cooling beam near resonance at 397 nm and is repumped by a classical standing wave within the cavity at 866 nm. The Gaussian envelope of the intensity at 866 nm, extracted from the resonance fluorescence, is determined by the convolution of the cavity waist w_0 and relative ion-cavity motion. The inset shows a full scan for a fixed position of the cooling beam, while for the data in the central plot, the cooling beam is re-centered on the ion at each data point. (The inset displays the count rate on the CCD camera vs. the ion position in arbitrary units.)

to the cavity on the μm scale is present, we expect to measure a broadened waist, representing the convolution of the motion and the mode structure.

We drive the cavity with the repump laser at 866 nm in order to generate a classical standing wave field. The ion is then driven near resonance at 397 nm with the cooling laser. Because the repump is below saturation, ion fluorescence is position-dependent and can be used to extract the 866 nm intensity as a function of position. Both fluorescence and position are measured on the CCD camera. The resulting position-dependent intensity reveals a periodically modulated Gaussian mode (right inset in fig. 6.2) instead of the simple Gaussian that one expects.

We can explain this modulation by assuming that the trap axis of symmetry is not completely orthogonal to the cavity, due to imperfect alignment in assembly of the experiment. Therefore, as the ion is translated along the trap axis, it also intersects the standing wave of the cavity mode. From the number of fringes visible and the wavelength of the standing wave field, we extract the deviation of this angle from perpendicular to be 4° . (We observe a similar structure when we tune the relative ion-cavity position along the axis perpendicular to both cavity and trap, but we are unable to calibrate the length scale in this direction.) We note that these deviations do not affect the cavity-QED experiments described in this text, which are carried out for a fixed ion position.

For the data shown in the right inset of fig. 6.2, the ion is continuously displaced by $60 \mu\text{m}$ along the trap axis. Although the periodic intensity modulation is visible, the intensity of the cooling beam varies significantly along the path of the ion, resulting in a nonuniform ion temperature. In a more accurate measurement, shown in the main part of fig. 6.2, we align the cooling beam to the ion position for every data point, recorded at maxima and minima of the modulated Gaussian field.

In order to extract any motion $\sigma_{x,y,z}$ which broadens our measured waist, we model the structure of the data in fig. 6.2 by assuming a Gaussian localization of the ion wavepacket

$$|\psi(x, y, z)|^2 = \frac{1}{(2\pi)^{3/2}\sigma_x\sigma_y\sigma_z} e^{-\frac{x^2}{2\sigma_x^2}} e^{-\frac{y^2}{2\sigma_y^2}} e^{-\frac{z^2}{2\sigma_z^2}}. \quad (6.1)$$

We define a coordinate system in which the z -axis is oriented along the cavity axis and the trap axis lies in the xz -plane (i.e., the trap axis is situated at an angle of 4° to the x -axis in this plane). The intensity of the cavity field is given by

$$I(x, y, z) = I_0 e^{-\frac{2x^2}{w_0^2}} e^{-\frac{2y^2}{w_0^2}} \sin^2\left(\frac{2\pi}{\lambda}z\right), \quad (6.2)$$

where $\lambda = 866 \text{ nm}$. We have approximated the waist of the TEM_{00} mode as w_0 , since the range of travel in the z direction is much smaller than the Rayleigh range of $640 \mu\text{m}$. The expected intensity profile I_{eff} seen by the ion is then given by the convolution of $|\psi(x, y, z)|^2$ with $I(x, y, z)$. We solve for $I_{\text{eff}}(x, y, z)$ analytically and set $y = 0, z = x \tan 4^\circ$ to parameterize I as a function of x , as in the measurement of fig. 6.2:

$$I(x) \propto e^{-2x^2/(4\sigma_x^2+w_0^2)} \left(1 - \cos\left(\frac{4\pi x \tan 4^\circ}{\lambda}\right) e^{-8\pi^2\sigma_z^2/\lambda^2}\right). \quad (6.3)$$

We fit this function to the data of fig. 6.2 and obtain values $\sigma_x = 4.7 \pm 2.2 \mu\text{m}$ and $\sigma_z = 48 \pm 46 \text{ nm}$. The value for σ_z is consistent with the localization of the previous measurement. Concerning σ_x , it is surprising that micron-scale motion is only orthogonal to the cavity axis; we hypothesize that this motion is due to a vibration of the cavity mount with respect to the trap along the axis of the cavity mount, coupled into the chamber via the translational feedthrough.

The effect of σ_x on the ion-cavity coupling is given by

$$g_{\text{obs}} = \frac{1}{\sqrt{2\pi}\sigma_x} \int_{-\infty}^{\infty} dx e^{-\frac{x^2}{2\sigma_x^2}} g_0 e^{-\frac{x^2}{w_0^2}} = (0.89 \pm 0.06)g_0. \quad (6.4)$$

Thus, the observed coupling along the x axis is only slightly reduced from its maximal value, and we have shown in the previous measurement that a reduction along the z axis is negligible. Although we are not able to quantify the extent of

motion along the y axis, the agreement of our data with simulations in which $g = g_{\text{obs}}$ (sec. 7.2) suggests that it does not contribute significantly.

For experiments involving two ions, the observed modulation in the coupling along the trap axis allows for precise control of the ions' individual coupling to the mode of the cavity. As the typical spacing between two ions is on the order of $\sim 5 \mu\text{m}$, we have the ability to place the ions at neighboring anti-nodes by adjusting the voltage of the tip electrodes; in this case, both ions couple with similar, near-maximal strength. Conversely, we can position one ion at a node and the other at an antinode, thus coupling only one ion to the cavity.

7 Cavity-assisted Raman spectroscopy

We have previously shown that with our ion-cavity system, single photons can be generated both with high efficiency and high two-photon suppression [27]. For a quantum interface, we now use the polarization of the photon to encode the flying qubit. We therefore have to select two Raman transitions in which the polarization of the generated photon is controlled by the atomic qubit state that is addressed.

In this chapter, we first identify suitable states and transitions in $^{40}\text{Ca}^+$ for ion-photon interface protocols. We then perform spectroscopy on all $S_{1/2} \leftrightarrow P_{3/2} \leftrightarrow D_{5/2}$ Raman transitions and demonstrate that we can address specific qubit states generating cavity photons with the desired polarization. These results were published in [52].

7.1 Geometry of beams and magnetic field

Each of the manifolds involved in the $S_{1/2} \leftrightarrow P_{3/2} \leftrightarrow D_{5/2}$ Raman transition offers a rich Zeeman structure, which can be exploited for realizing quantum interface schemes. For the purpose of encoding a photonic qubit in its polarization degree of freedom, one can imagine a model in which two and only two cavity-assisted Raman transitions are possible. That is, the two transition paths could either share an initial state but not a final state, or they could connect different initial states to the same final state. In the first case, we identify the two final states as an atomic qubit, whereas in the second case, the initial states constitute the atomic qubit. If these two Raman transitions produce photons with orthogonal polarizations, then each state of the atomic qubit can be identified with one transition and thus one polarization state of the photon.

In this section, we focus on the case in which two transition paths begin in the same state and identify a favorable experimental configuration. This case corresponds to the generation of atom-photon entanglement, described in chapter 8. The inverse case, which corresponds to a mapping of the atomic qubit to the photonic one, will be discussed in chapter 9.

In $^{40}\text{Ca}^+$, starting in one of the $S_{1/2}$ states, we apply a drive laser at 393 nm on the $S_{1/2} \leftrightarrow P_{3/2}$ transitions in order to turn on the Raman coupling. For every possible polarization (σ^+ , π or σ^-) of this laser, there exist three Raman transitions, each coupling to a different state of the $D_{5/2}$ manifold as shown in fig. 7.1. At zero magnetic field, all Zeeman substates of one manifold are degenerate, and therefore all Raman transitions overlap in frequency, resulting in an unfavorable situation: three transitions are possible instead of two. The number of allowed Raman transitions thus has to be reduced by one.

One option to disable one of the three Raman transitions at zero magnetic field is realized in neutral atom experiments [21, 126]. If the cavity axis is chosen as the quantization axis, we see that the polarization of π photons lies along the cavity axis and that therefore only circularly polarized photons are emitted into the cavity. For the case of a drive laser with propagation orthogonal to the cavity axis and linear polarization along the cavity axis, the initial state is coupled to only one of the $P_{3/2}$ states. As a consequence, only two Raman transitions are driven, which generate σ^+ - and σ^- -polarized photons in the cavity, as in our model system.

Alternatively, one can apply a magnetic field B , which lifts the degeneracy between Zeeman substates and splits Raman transitions as given by eq. 3.2. This splitting enables individual addressing of all Raman transitions via the detuning of the drive laser δ_{drv} or the cavity δ_{cav} and the polarization of the drive laser. Since for an atom-photon interface, it is advantageous to have the polarization and frequency degrees of freedom of the photon uncorrelated, the individual transitions should be addressed by the frequency and polarization of the drive laser only, while the cavity detuning remains fixed. Thus, photons generated by all Raman transitions have the same frequency. In this case, our model can be realized by driving two Raman transitions at two distinct drive-laser frequencies simultaneously. For a proper definition of the photonic qubit, two transitions have to be chosen so as to generate photons in orthogonal polarization modes of the cavity.

As the individual addressing of the $S_{1/2} \leftrightarrow D_{5/2}$ transitions required for atomic qubit manipulation and detection relies on a nonzero magnetic field, we opt for the second scenario, as it avoids a change of the magnetic field during the experiment.

Out of the nine $S_{1/2} \leftrightarrow P_{3/2} \leftrightarrow D_{5/2}$ Raman transitions available from each S state (fig. 7.1), we now select two according to the following considerations. (In the discussion that follows, we assume that the Raman resonance condition is satisfied, that is, that δ_{drv} exactly balances the sum of δ_{cav} and all Zeeman and Stark shifts of the initial and final states.) First, the coherence of photon generation in our system is determined by the ratio of the effective Raman coupling strength Ω_{eff} to the effective spontaneous emission rate of the atom γ_{eff} [27]. The effective Raman coupling comprised of the $S_{1/2} \leftrightarrow P_{3/2}$ transition i and the $P_{3/2} \leftrightarrow D_{5/2}$ transition j has an amplitude of

$$\Omega_{i,j}^{\text{eff}} \approx \frac{\alpha_i \Omega_{\text{drv}} \beta_j 2 g_0}{2|\delta_{\text{drv}}|}, \quad (7.1)$$

where Ω_{drv} is the drive-laser Rabi frequency, δ_{drv} is the drive-laser detuning, and g_0 is the strength of the ion-cavity coupling to the $P_{3/2} \leftrightarrow D_{5/2}$ transition. The coefficient α_i is the product of the projection of the drive laser polarization onto the dipole moment of transition i with the Clebsch-Gordon coefficient of this transition. Analogously, β_j is the product of the projection of the polarization plane of the cavity mode to the atomic dipole moment of transition j with the Clebsch-Gordon coefficient of this

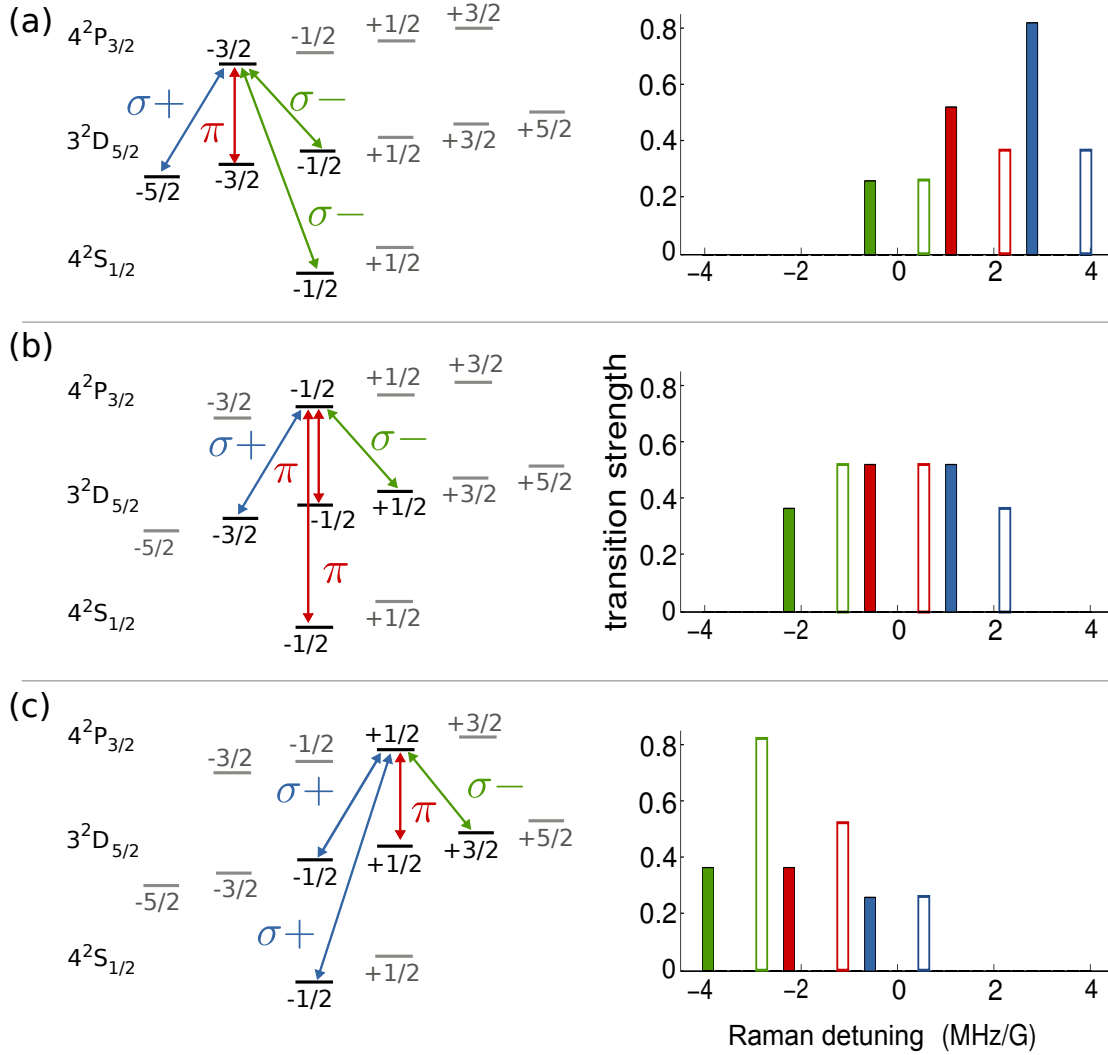


Figure 7.1: $S_{1/2} \leftrightarrow P_{3/2} \leftrightarrow D_{5/2}$ Raman transition strengths. **(Left)** Simplified level scheme showing all electronic states available for Raman transitions at nonzero magnetic field. We consider three drive laser polarizations, **(a)** σ^- , **(b)** π and **(c)** σ^+ . For each drive laser polarization, three Raman transitions are possible from each $S_{1/2}$ state. The polarization of the photons emitted on these transitions are σ^+ , π and σ^- . **(Right)** Schematic plot of the relative strengths of the Raman transitions corresponding to these drive laser polarizations. The filled (unfilled) bars represent the transitions that couple to the $|S_{1/2}, -\frac{1}{2}\rangle$ ($|S_{1/2}, +\frac{1}{2}\rangle$) state. The Raman detuning is the detuning of the drive laser or the cavity at nonzero magnetic field. Note: the relative transition strengths in the experiment also depend on the projection of the emitted photons' polarization onto the plane in which cavity photons are polarized.

transition. The effective spontaneous emission rate of the atom is given by

$$\gamma_{\text{eff}} \approx \gamma \left(\frac{\Omega_{\text{drv}}}{2|\delta_{\text{drv}}|} \right)^2, \quad (7.2)$$

which becomes independent of transition i, j when the detuning δ_{drv} is much larger than the Zeeman splittings ΔE given by Eq. 3.2. For a fixed ratio $\Omega_{\text{drv}}/|\delta_{\text{drv}}|$ and g_0 determined by the cavity geometry, in order to maximize the ratio $\Omega_{\text{eff}}/\gamma_{\text{eff}}$, one should maximize the product $\alpha_i \cdot \beta_j$.

A second criterion for selection is that the two transitions should have similar strengths, since then mapping of both components of an arbitrary atomic superposition to the photonic one occurs at the same rate.

In order to meet both criteria, i.e., both high and similar coupling strengths, two scenarios emerge as attractive. In the first scenario, the magnetic field is oriented along the cavity axis. If we choose the magnetic field axis as the quantization axis, the possible polarization states of photons in the cavity are then σ^+ and σ^- . If we choose the initial state to be $|S_{1/2}, -\frac{1}{2}\rangle$, then the optimal transition pair is $|S_{1/2}, -\frac{1}{2}\rangle \leftrightarrow |P_{3/2}, -\frac{1}{2}\rangle \leftrightarrow |D_{5/2}, -\frac{3}{2}\rangle$ and $|S_{1/2}, -\frac{1}{2}\rangle \leftrightarrow |P_{3/2}, -\frac{1}{2}\rangle \leftrightarrow |D_{5/2}, +\frac{1}{2}\rangle$, with transition strengths $(\alpha_i \cdot \beta_j, \alpha'_i \cdot \beta'_j) = (0.52, 0.37)$. The corresponding transitions from $|S_{1/2}, +\frac{1}{2}\rangle$ have identical transition strengths.

In the second scenario, the direction of the magnetic field is orthogonal to the cavity axis. We again identify the magnetic field axis as the quantization axis; photons emitted by the atom with circular polarization are now projected to horizontally-polarized (H) cavity photons, while linearly-polarized π photons are projected to vertically-polarized (V) cavity photons, where this assignment defines H and V . Again, we assume initial state $|S_{1/2}, -\frac{1}{2}\rangle$. The optimal transition pair is given by $|S_{1/2}, -\frac{1}{2}\rangle \leftrightarrow |P_{3/2}, -\frac{3}{2}\rangle \leftrightarrow |D_{5/2}, -\frac{5}{2}\rangle$ and $|S_{1/2}, -\frac{1}{2}\rangle \leftrightarrow |P_{3/2}, -\frac{3}{2}\rangle \leftrightarrow |D_{5/2}, -\frac{3}{2}\rangle$, with strengths $(\alpha_i \cdot \beta_j, \alpha'_i \cdot \beta'_j) = (0.58, 0.52)$, where the drive beam is circularly polarized. (The corresponding transitions from $|S_{1/2}, +\frac{1}{2}\rangle$ again have identical strengths.) As these transition strengths are both larger and more similar than in the first scenario, this pair is the most suitable for the generation of atom-photon entanglement.

In order to realize this geometry for atom-photon entanglement, the magnetic field orientation was changed to be both orthogonal to the cavity axis and at an angle of 45° to the trap axis. With this magnetic field orientation, a new σ^- polarized beam (called beam B in the following) was installed with propagation direction along the magnetic field axis (fig. 4.5). All measurements reported in earlier theses [65, 85] on this experiment were carried out with a linearly polarized drive beam (beam A, fig. 4.5). Its linear polarization can be rotated with a half-waveplate in order to drive π transitions, simultaneous σ^+ and σ^- transitions, or a combination of all three.

We note that this choice of a magnetic field aligned orthogonally to the cavity axis should be preferred in any setup in which state initialization is performed via optical pumping with a circularly polarized beam at 397 nm. If the magnetic field

were aligned along the cavity axis, it would be technically challenging to optimize the polarization of a circularly polarized beam at 397 nm propagating through the cavity mirrors and optical elements, such as waveplates and dichroic mirrors, optimized for 854 nm and 785 nm.

7.2 Raman spectra for different geometries

In order to locate specific cavity-mediated Raman transitions, we first probe the spectrum of Raman transitions between the $S_{1/2}$ and $D_{5/2}$ manifolds by scanning the detuning of the drive laser δ_{drv} ; the cavity detuning $\delta_{\text{cav}} \approx 2\pi \times 400$ MHz remains fixed.

The experimental sequence is as follows: after Doppler cooling the ion for 2 ms, we apply the drive laser simultaneously with the near-resonant 854 nm and 866 nm repump lasers for 300 μs . During this interval, we record photons emitted from the cavity at the APDs, where the waveplates in front of the PBS at the cavity output have been set to measure photons in the (H, V) basis. We repeat this sequence 250 times for each value of δ_{drv} . The observed spectrum depends on the polarization of the drive laser beam. The frequencies of the spectrum peaks are Stark-shifted by the drive laser field. Rabi frequencies Ω_{drv} are thus calibrated by measuring the spectrum frequency shift due to a known fractional change in the drive intensity.

Beam A drives the $S_{1/2} \leftrightarrow P_{3/2}$ transition with σ^+ and σ^- polarization, resulting in 12 possible Raman transitions, indicated in the center of fig. 7.2. However, transitions which share the same initial and final states but are driven via a different virtual state of the $P_{3/2}$ manifold are resonant at the same drive laser frequency. We therefore expect ten peaks in the spectrum, all of which are identified in fig. 7.3. Moreover, for each peak, we are able to resolve sidebands corresponding to the ion's secular motion at frequencies ω_{axial} and $\omega_{\text{radial1,radial2}}$. The Rabi frequency of the drive laser is given by $\Omega_{\text{drv}} = 2\pi \times 88$ MHz. This frequency corresponds to values $\Omega_{i,j}^{\text{eff}} = 2\pi \times \alpha_i \beta_j \times 0.31$ MHz and $\Gamma_{\text{eff}} = 2\gamma_{\text{eff}} = 2\pi \times 0.25$ MHz.

Beam B propagates along the magnetic field axis with σ^- polarization, driving six Raman transitions, indicated in the right part of fig. 7.2. Due to its polarization, beam B depopulates the $|S_{1/2}, +\frac{1}{2}\rangle$ state via optical pumping. Although the state can be repopulated by the repumping beams, its steady-state population in simulations is on the order of 5%. We thus expect three central peaks in the Raman spectrum, which can be identified in fig. 7.3(b) ($\Omega_{\text{drv}} = 2\pi \times 99$ MHz, $\Omega_{i,j}^{\text{eff}} = 2\pi \times \alpha_i \beta_j \times 0.35$ MHz, $\Gamma_{\text{eff}} = 2\pi \times 0.32$ MHz). The difference in maximum count rate between the spectra of beams A and B is due primarily to optical pumping: the Raman transition and the repump laser drive a nearly closed cycle, efficiently generating cavity photons. The two strongest transitions driven by beam B are the ones selected in Section 7.1 as optimal for atom-photon entanglement.

For both drive beams, the relative heights of the spectrum peaks correspond

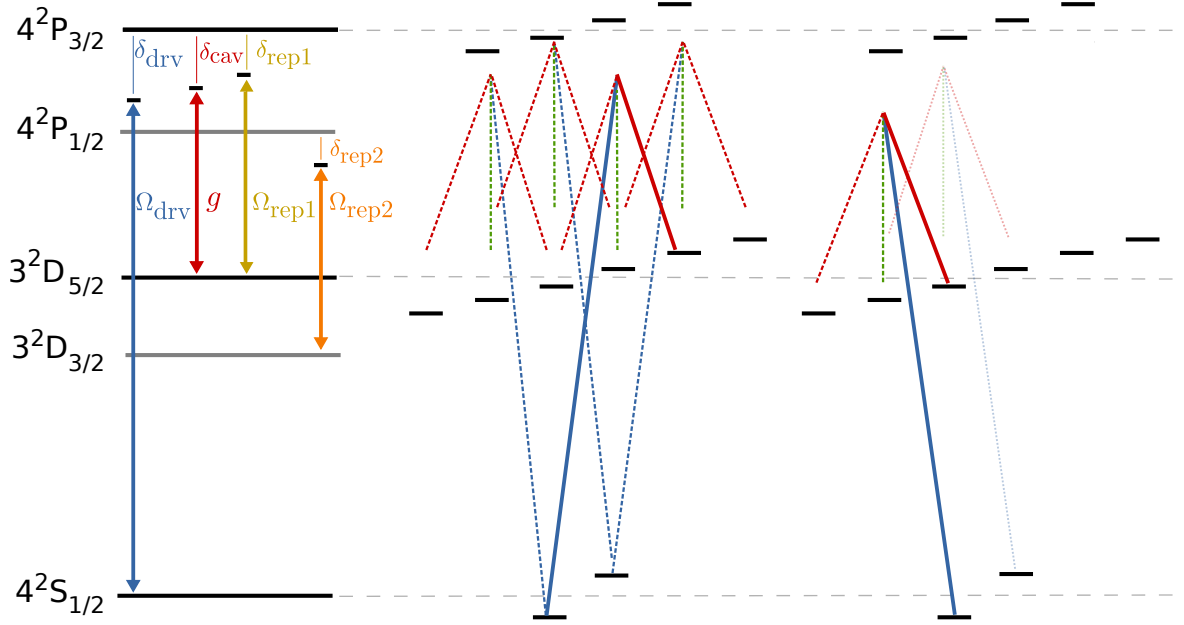


Figure 7.2: Driving schemes for the $S_{1/2} \leftrightarrow P_{3/2} \leftrightarrow D_{5/2}$ Raman transitions. **(Left)** Simplified level scheme of $^{40}\text{Ca}^+$ with relevant ion-field couplings: $\Omega_{\text{drv}}, \Omega_{\text{rep1}}, \Omega_{\text{rep2}}$ are the Rabi frequencies of the drive and the two repump lasers, respectively, and $\delta_{\text{drv}}, \delta_{\text{rep1}}, \delta_{\text{rep2}}$ are the detunings of these lasers from resonance. The Rabi frequency of the ion-cavity coupling is $2g$, where the cavity is detuned by δ_{cav} from the $D_{5/2} \leftrightarrow P_{3/2}$ transition. **(Center)** Due to its linear polarization orthogonal to the magnetic field, beam A drives σ^+ and σ^- transitions (blue arrows). Photons emitted into the cavity have horizontal (red) or vertical polarization (green). For the value of δ_{drv} indicated here, only the transition illustrated with a solid line is resonant. **(Right)** Beam B has σ^- polarization and thus provides optical pumping, suppressing three of the six possible Raman transitions (transparent lines).

roughly to the calculated transition strengths (see sec. 7.1). The full dynamics of the 18-level system with two orthogonal cavity modes, driven by three lasers, are described by master-equation simulations, also plotted in fig. 7.3 and fig. 7.3(b). For example, one would expect the spectrum of fig. 7.3 to be symmetric, as corresponding transitions from the two $S_{1/2}$ states have equal strengths, but the asymmetry in height from left to right is due to a detuning of the repump laser at 854 nm. The peak width is primarily determined by the Rabi frequency Ω_{drv} ; the background signal is entirely due to dark counts of the APD. The frequency splitting between peaks is determined by the magnetic field of 4.77 G, which we have selected in order to avoid overlap of sidebands from neighboring transitions. The simulation amplitudes correspond to a cavity output path efficiency of 8.0%, consistent with the measured path efficiencies of $(8.1 \pm 1.5, 7.6 \pm 1.5)\%$.

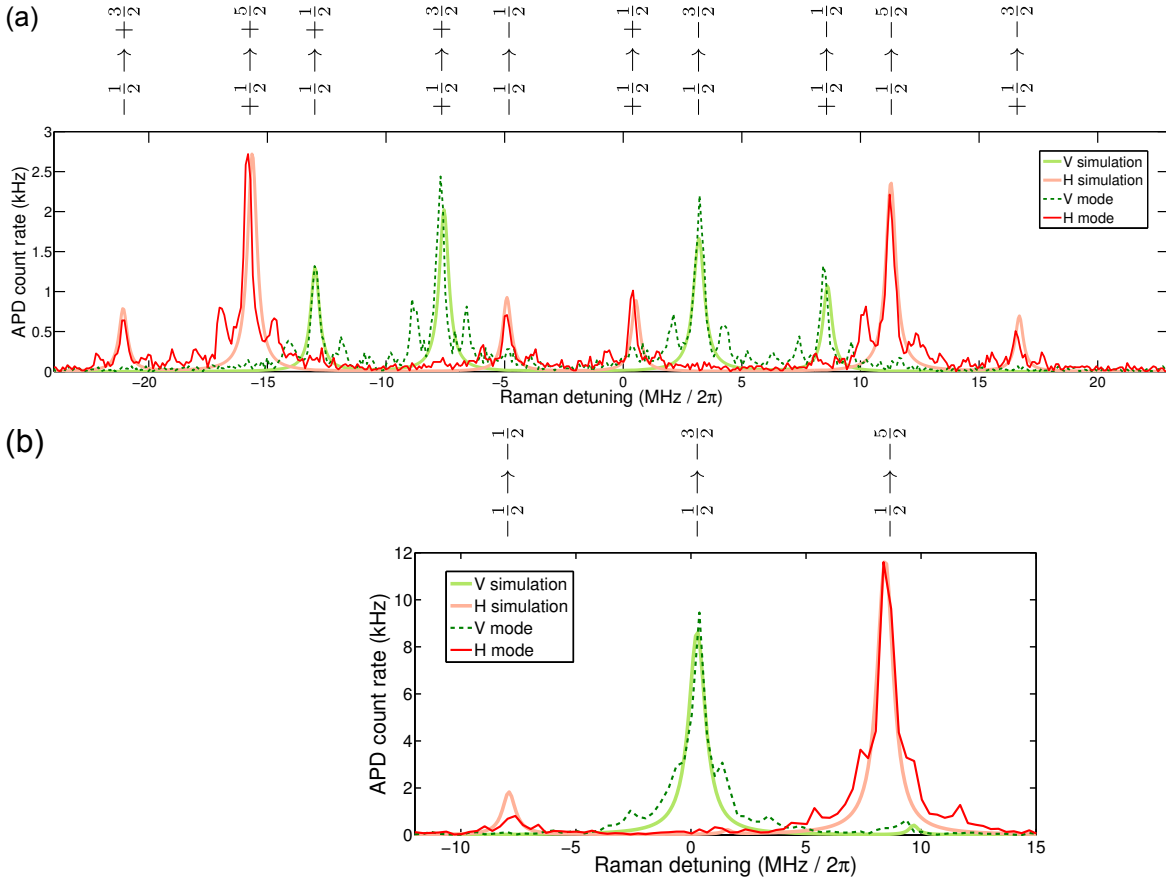


Figure 7.3: Raman spectroscopy of the $S_{1/2} \leftrightarrow P_{3/2} \leftrightarrow D_{5/2}$ transition. One arm of the Raman transition is provided by the cavity; the other arm is provided by (a) drive beam A with σ^+/σ^- polarization, or (b) drive beam B σ^- polarization. APD count rates are plotted as a function of the drive laser detuning; photons from the H (red) and V (green) cavity modes are recorded on separate APDs. The quantum states of each transition are noted above the individual peaks. A steady-state solution of the master equation, taking into account both cavity modes and 18 levels of $^{40}\text{Ca}^+$, agrees well with the data. The master-equation simulation does not include motion of the ion and thus does not reproduce the sidebands that are visible at secular frequencies ω_{axial} and $\omega_{\text{radial1,radial2}}$. Note the different scale of the APD count rate in (b). The two transitions in the middle and on the right of (b) are the ones employed for ion-photon entanglement.

7.3 Motional sidebands

Motional sidebands are driven by beams A and B due to the nonzero projection of their \vec{k} -vector to all three motional axes. The axial and radial Lamb-Dicke parameters for both beams are given by $\eta_a = 0.12$ and $\eta_r = 0.05$. In fig. 7.4a, we plot the spectrum of beam B in a narrow scan of δ_{drv} across the $|S_{1/2}, -\frac{1}{2}\rangle \leftrightarrow |P_{3/2}, -\frac{3}{2}\rangle \leftrightarrow |D_{5/2}, -\frac{5}{2}\rangle$ transition. If the ion is sideband-cooled to the axial ground state before the drive laser is applied, the axial red sideband is suppressed. As the blue sideband height is proportional to $\sqrt{n_a + 1}\eta_a$, where n_a is the ion's axial phonon number, the height of the blue sideband also decreases by a factor of $\frac{1}{\sqrt{n_a+1}}$ [42].

Moreover, we are able to drive micromotion sidebands at frequencies shifted by $\omega_{\text{trap}} = 2\pi \times 23.4$ MHz from those of the primary spectrum. Typically, micromotion is compensated in the experiment so as to suppress sidebands on the quadrupole transition, which also results in suppression on the cavity Raman transition. For comparison, however, the Raman spectrum of beam B is shown in fig. 7.4b also for the case in which micromotion has not been properly compensated.

Evidence of motional sidebands is intriguing because of prospects for using the motional states of the ion to construct a quantum interface [127]. However, since the effective Raman coupling Ω_{eff} depends on the Lamb-Dicke parameter η to first order, but γ_{eff} depends on η to second order, the ratio $\Omega_{\text{eff}}/\gamma_{\text{eff}}$ is reduced by η for motional sidebands. Employing the motional sidebands for photon generation would thus imply a weak effective Raman coupling.

In conclusion, we employ the frequency of the drive laser at the $S_{1/2} \leftrightarrow P_{3/2}$ transition to address individual $S_{1/2} \leftrightarrow P_{3/2} \leftrightarrow D_{5/2}$ Raman transitions in which photons are generated in the cavity resonant with the $P_{3/2} \leftrightarrow D_{5/2}$ transition. We have implemented a configuration of magnetic field orientation, driving beam polarization, and cavity photon polarization suitable for ion-photon entanglement. This configuration offers two Raman transitions with similar strength that address the two qubit states and generate photons with orthogonal polarization. Driving these two transitions simultaneously allows for generating ion-photon entanglement which we demonstrate in the next chapter.

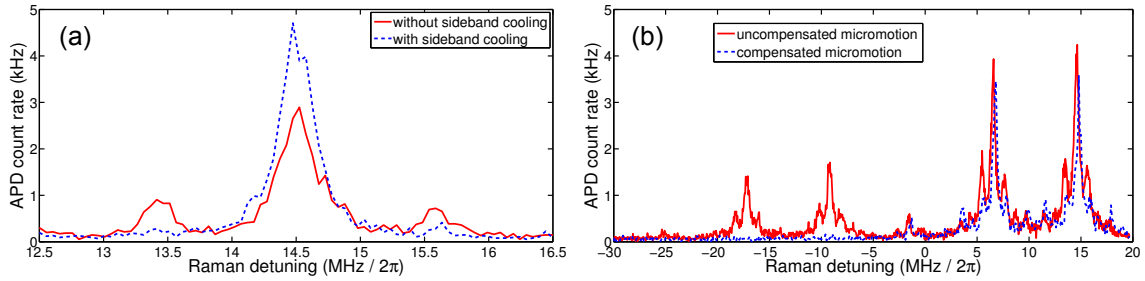


Figure 7.4: Motional sidebands resolved by Raman spectroscopy. We drive cavity-assisted transitions using beam B and plot the APD count rate as a function of drive laser detuning. **(a)** We drive the $|S_{1/2}, -\frac{1}{2}\rangle \leftrightarrow |P_{3/2}, -\frac{3}{2}\rangle \leftrightarrow |D_{5/2}, -\frac{5}{2}\rangle$ transition (also the rightmost transition of fig. 7.3(b)) and plot the count rate after Doppler cooling (red solid line) and axial sideband cooling (blue dashed line) of the ion. The Rabi frequency is $\Omega_{\text{drv}} = 2\pi \times 33$ MHz. Note the suppression of the red axial sideband and the reduction of the blue axial sideband after sideband cooling. **(b)** Micromotion sidebands, offset from the primary spectrum by the trap drive radio frequency of 23.4 MHz, are observable (red line) but can be suppressed (blue line) by applying DC voltages to compensation electrodes. The different height of the carrier is due to a different position in the standing wave. For this data, $\Omega_{\text{drv}} = 2\pi \times 92$ MHz.

8 Tunable ion-photon entanglement

We have now identified all Raman transitions between the $S_{1/2}$, $P_{3/2}$, $D_{5/2}$ manifolds and demonstrated the ability to generate single photons with controlled polarization [52]. Together with the coherent initialization, manipulation and read out of the electronic state of the ion, we have all the necessary tools in hand for the realization of atom-photon interface protocols. One fundamental building block of such an interface is the generation of atom-photon entanglement. This chapter provides a detailed description of the generation and verification of atom-photon entanglement in our setup via a bichromatic excitation. Furthermore, the tunable character of the ion-photon interaction as well as the time-independence of the resulting entangled state is demonstrated. These results were published in [53].

8.1 Motivation

Proposed quantum networks require both a quantum interface between light and matter and the coherent control of quantum states [14, 41]. A quantum interface can be realized by entangling the state of a single photon with the state of an atomic or solid-state quantum memory, as demonstrated in recent experiments with trapped ions [25, 31], neutral atoms [21, 126], atomic ensembles [33, 34], and nitrogen-vacancy spins [35]. The entangling interaction couples an initial quantum memory state to two possible light-matter states, and the atomic level structure of the memory determines the available coupling paths. In previous work, these paths' transition parameters determine the phase and amplitude of the final entangled state, unless the memory is initially prepared in a superposition state [31], a step that requires coherent control. Here we report the fully tunable entanglement of a single $^{40}\text{Ca}^+$ ion and the polarization state of a single photon within an optical resonator. Our method, based on a bichromatic, cavity-mediated Raman transition, allows us to select two coupling paths and adjust their relative phase and amplitude. The cavity setting enables intrinsically deterministic, high-fidelity generation of any two-qubit entangled state. This approach is applicable to a broad range of candidate systems and thus presents itself as a promising method for distributing information within quantum networks.

Optical cavities are often proposed as a means to improve the efficiency of atom-photon entanglement generation. Experiments using single emitters [21, 25, 31, 35] collect photons over a limited solid angle, with only a small fraction of entanglement events detected. However, by placing the emitter inside a low-loss cavity, it is possible to generate photons with near-unit efficiency in the cavity mode [41, 128]. Neutral atoms in a resonator have been used to generate polarization-entangled photon pairs

[126, 129], but this has not yet been combined with coherent operations on the atomic state. Trapped ions have the advantage of well-developed methods for coherent state manipulation and readout [42, 43]. Using a single trapped ion integrated with a high-finesse cavity, we implement full tomography of the joint atom-photon state and generate maximally entangled states with fidelities up to $(97.4 \pm 0.2)\%$.

In earlier demonstrations of atom-photon entanglement, the amplitudes of the resulting state are fixed by atomic transition amplitudes [21, 25, 35, 126, 129]. If the final atomic states are not degenerate, as in the case of a Zeeman splitting, the phase of the atomic state after photon detection is determined by the time at which detection occurs. In contrast, we control both amplitude and phase via two simultaneous cavity-mediated Raman transitions. The bichromatic Raman fields ensure the independence of the atomic state from the photon-detection time; their relative amplitude and phase determine the state parameters. Within a quantum network, such a tunable state could be matched to any second state at a remote node, generating optimal long-distance entanglement in a quantum-repeater architecture [40].

A tunable state has previously been employed as the building block for teleportation [31] and a heralded gate between remote qubits [130]. In this case, tunability of the entangled state is inherited from control over the initial state of the atom. The photonic qubit is encoded in frequency, and as a result, integration with a cavity would be technically challenging. The entangling process is intrinsically probabilistic, with efficiency limited to 50% even if all emitted photons could be collected. In the scheme presented here, the entangling interaction itself is tunable, and no coherent manipulation of the input state is required. For atomic systems with a complex level scheme in which several transition paths are possible, the two most suitable paths can be selected.

8.2 Entanglement and Bell inequalities

Entanglement is one of the most fascinating properties of quantum mechanics in which two remote, entangled quantum objects show non-classical correlations without interaction. While nowadays entanglement is regarded as a key resource for quantum communication and computing, in the history of quantum mechanics its implications have caused fundamental debates on the correct constitution of a physical theory [131–133]. Experiments have confirmed the predictions of quantum mechanics, but its limits remain to be clarified: why can we entangle quantum objects as atoms and photons but not classical objects [132]?

Mathematically, the global state of a composite system $\rho_{A,B}$ is entangled if it cannot be separated into a product of the states ρ_A and ρ_B of the individual subsystems A and B: $\rho_{A,B} \neq \rho_A \otimes \rho_B$. If one wants to describe the state of subsystem A (or B) alone by tracing out the other subsystem B (or A) of $\rho_{A,B}$, one obtains a completely mixed state ρ_A . A mixed ensemble is entangled if its state cannot be decomposed into

a mixture of factorisable pure states.

A quantitative characterization of entanglement is possible via entanglement measures. For a pure state, the entanglement is given by the entropy of subsystem A (or B). For mixed states, this measure can be generalized to the entanglement of formation, which can in turn be expressed as an explicit function of the density matrix ρ via the concurrence [39]. The concurrence is an entanglement measure itself, ranging from 0 to 1 [134]:

$$C(\rho) = \max\{0, \lambda_1 - \lambda_2 - \lambda_3 - \lambda_4\}, \quad (8.1)$$

where λ_i are the eigenvalues, in decreasing order, of the concurrence matrix $R(\rho) = \sqrt{\sqrt{\rho}\tilde{\rho}\sqrt{\rho}}$, with $\tilde{\rho} = (\sigma_y \otimes \sigma_y)\rho^*(\sigma_y \otimes \sigma_y)$ and σ_y the y -Pauli operator.

Unsatisfied with the probabilistic structure of quantum mechanics, Einstein, Podolsky and Rosen argued in 1935 that “the wavefunction does not provide a complete description of the physical reality” [131]. Theories that do fulfill such a classical description and imply realism (objects have certain properties independent of a measurement) and locality (the properties of spatially separated objects are independent from each other) can be summarized as local hidden-variable models (LHVMs). In 1964 John Bell introduced a quantitative version of the so-called “EPR-paradox,” an inequality capable of testing quantum mechanics against LHVMs [133]. A generalized inequality has been derived by Clauser, Horne, Shimony and Holt (CHSH), accessible in experimental tests [135]. The first experiments showing a violation of a CHSH-Bell inequality were performed with photons [136–139], followed by experiments with massive particles [140, 141]. With this work, we add one more experiment that shows the violation of a CHSH-Bell inequality, using the entanglement of the hybrid atom-photon system [129, 142].

Although all experimental tests of Bell-type inequalities to date confirm the predictions of quantum mechanics, they suffer from at least one loophole [143]. While photon experiments have been able to close the locality loophole [144], they suffer from the detection loophole. Experiments with atoms, on the other hand, have closed the detection loophole [140] but continue to be subject to the locality loophole.

The possibility of a loophole-free test of Bell-type inequalities with a hybrid atom-photon system like the one studied in this work has been analyzed in [143]. Although the proposed generation of non-maximally entangled states between atom and photon can be realized in our setup, not all requirements can be fulfilled. First, the overall photon detection efficiency would have to be increased from 6% to $\sim 43\%$, which could only be achieved by using better cavity mirrors (see section 8.10). Second, in order to enforce locality of the measurements, the photon would have to be measured at a distance from the atom large enough to circumvent information transfer of measurement results between atom and photon via classical communication. Given the minimum time of $\sim 170 \mu\text{s}$ needed in our setup for complete detection of the atom at an error $\leq 1\%$, the separation needs to be on the order of $c \cdot 170 \mu\text{s} = 50 \text{ km}$. Even if the detection time could be decreased by an order of magnitude, e.g., by using higher NA

objectives and additional detectors, the losses in an optical fiber at the wavelength of 854 nm would be on the order of 30 % [145], making this method very challenging.

A loophole-free test of a Bell-type inequality appears more promising via simultaneous measurement of two remote, entangled atoms [146]. Long-distance entanglement of remote atoms can be achieved via atom-photon entanglement [36]. In order to avoid the locality loophole, the time required for atomic detection sets the necessary distance between the two atoms. With two ion-trap cavity systems capable of generating atom-photon entanglement as described in this work, a minimum separation of 5 km is necessary with the current atom-detection method. In this case, photon absorption in the optical path only determines the rate at which entanglement between the atoms can be generated but does not influence the detection loophole, if the entanglement of the atoms can be heralded.

8.3 Bichromatic Raman transition

In most of the reported atom-photon entanglement experiments, a monochromatic excitation initiates a process in which exactly two transitions are driven simultaneously, resulting in entanglement between the electronic state of the atom and the polarization of the photon [21, 25, 35, 126]. Here, the structure of the atomic level scheme has to ensure that exactly two transitions are possible. The means by which entanglement is generated is thus fixed by the level scheme of the chosen species. An exception to those monochromatic schemes is the experiment of [31], in which a short pulse with a broad frequency spectrum is used in order to map an atomic superposition state to an atom-photon entangled state. However, the application of this method is restricted to the particular level scheme of the atom employed.

Given the level structure of $^{40}\text{Ca}^+$, making use of a cavity resonant with the $D - P$ transition, neither of these methods can be applied. In this work, we have therefore developed a new driving scheme, in which we select exactly two appropriate transitions in the level scheme of $^{40}\text{Ca}^+$ via bichromatic excitation. This bichromatic driving scheme not only enables the generation of atom-photon entanglement but also allows for the tunability of the atom-photon interaction. Due to this tunable interaction, all parameters of the entangled state can be controlled, as demonstrated in sections 8.7 and 8.8. Moreover, the scheme we have developed also results in a time-independence of both the entangled atom-photon state as well as the atomic superposition state after photon detection, as demonstrated in section 8.6. By starting in a superposition state of the atom, the bichromatic scheme also enables various additional protocols such as state mapping, as described in chapter 9. This tunable interaction could in principle be applied to any atomic species, as it allows one to freely choose two appropriate transitions in a system with a complex level structure.

The choice of transitions in $^{40}\text{Ca}^+$ for atom-photon entanglement has been discussed in section 7.1. As indicated in fig. 8.1(a), the magnetic field is oriented orthogonally

to the cavity axis, while the drive beam propagates along the magnetic field axis with σ^- polarization.

The entangling process is illustrated in fig. 8.1(b). Following a Doppler cooling interval, the ion is initialized via optical pumping in the state $|S\rangle \equiv |S_{1/2}, -\frac{1}{2}\rangle$. In order to couple $|S\rangle$ simultaneously to the two states $|D\rangle \equiv |D_{5/2}, -\frac{3}{2}\rangle$ and $|D'\rangle \equiv |D_{5/2}, -\frac{5}{2}\rangle$, we apply a phase-stable bichromatic Raman field, detuned by Δ_{l_1} and Δ_{l_2} from the $|S\rangle - |P\rangle$ transition. Here, the intermediate state $|P\rangle \equiv |P_{3/2}, -\frac{3}{2}\rangle$ is used. The cavity is stabilized at detuning $\Delta_1^c \approx -400$ MHz from the $|P\rangle - |D\rangle$ transition and $\Delta_2^c = \Delta_1^c + \Delta_{D,D'}$ from the $|P\rangle - |D'\rangle$ transition, where $\Delta_{D,D'}$ is the Zeeman splitting between $|D\rangle$ and $|D'\rangle$. When Δ_i^c and Δ_i satisfy the Raman resonance condition for both $i = (1, 2)$, population is transferred coherently from $|S\rangle$ to both $|D\rangle$ and $|D'\rangle$, and a single photon is generated in the cavity [26, 27, 95, 147].

The effective coupling strength of each of the two transitions is given by Ω_i^{eff} as defined in eq. 7.1. In free space, these two pathways generate π - and σ^+ -polarized photons, respectively. Within the cavity, the π photon is projected onto the horizontally (H) polarized mode and the σ^+ photon onto the vertically (V) polarized mode of the cavity [48, 52].

Ideally, the bichromatic field $\Omega_1 e^{i\omega_{l_1} t} + \Omega_2 e^{i(\omega_{l_2} t + \varphi_{\text{Raman}})}$ generates any state of the form

$$|\psi\rangle = \cos \alpha |DH\rangle + e^{i\varphi} \sin \alpha |D'V\rangle, \quad (8.2)$$

where $\alpha \equiv \tan^{-1} (\Omega_2^{\text{eff}} / \Omega_1^{\text{eff}})$ and φ is determined by the relative phase of the Raman fields φ_{Raman} .

For the generation of entanglement, the bichromatic fields have to be classical, described by coherent states $|\alpha\rangle$ [66]. Only then can the two paths not be distinguished via the absorption of a photon from either of the two fields, since a coherent state remains constant after annihilation of a single photon $\hat{a}|\alpha\rangle = |\alpha\rangle$.

Finally, it should be noted that the chosen geometry with a σ^- drive beam optimizes the efficiency of the entanglement in two ways. On the one hand, it maximizes the strengths of the Raman transitions with respect to off-resonant scattering. On the other hand, it also provides optical pumping. While a linearly polarized beam that drives π and/or σ^+/σ^- transitions could off-resonantly excite more than one Zeeman substate of the $P_{3/2}$ manifold, the σ^- drive beam can only populate the state $|P_{3/2}, -\frac{3}{2}\rangle$. While decay on the $P_{3/2} \leftrightarrow S_{1/2}$ transition in general thus populates both $S_{1/2}$ states, out of which one is uncoupled in the case of the σ^- drive beam, the decay automatically re-initializes the $|S_{1/2}, -\frac{1}{2}\rangle$ state. As no initial phase information can be lost, this re-initialization hence increases the efficiency compared to the use of a linearly polarized drive beam. The only process that still reduces the efficiency of photon generation is decay on the $P_{3/2} \leftrightarrow D_{5/2}$ transition. One could therefore argue that for this particular geometry, only the decay rate of the $P_{3/2} \leftrightarrow D_{5/2}$ state, $\gamma_{P_{3/2} \leftrightarrow D_{5/2}} = 2\pi \times 0.85$ MHz has to be considered for the relevant cavity-QED parameters (g, κ, γ) .

8.4 Experimental sequence and temporal pulse-shape overlap

In order to realize the bichromatic Raman transition described above, we have to identify the two target Raman transitions and generate the required optical frequencies. For the phase of the atomic state to be independent of the photon detection time, we set the frequencies of the Raman fields at 393 nm to be resonant with the atomic levels (sec. 8.6). Furthermore, the state detection of the atom at 729 nm has to be phase coherent with the entanglement generation at 393 nm. Therefore, we generate these fields via AOMs driven by RF signals which are in turn generated by DDS boards referenced to the same clock signal (sec. 4.11).

In a first step, we identify all Raman transitions via monochromatic spectroscopy (fig. 7.3), continuously driving the ion with a Raman beam at 393 nm and repump beams at 854 nm and 866 nm as described in sec. 7.2. At this stage, the single-pass AOM (sec. 4.4) is driven at 80 MHz creating a monochromatic field. Having identified the target transitions, we set the radio frequency of the double-pass AOM at 393 nm (sec. 4.4) in order to generate a field centered between the two target transitions.

In a second step, we measure the frequencies of the quadrupole carrier transitions $|S_{1/2}, -\frac{1}{2}\rangle \leftrightarrow |D_{5/2}, -\frac{5}{2}\rangle$ and $|S_{1/2}, -\frac{1}{2}\rangle \leftrightarrow |D_{5/2}, -\frac{3}{2}\rangle$ at 729 nm required for the atomic state detection (sec. 8.5) to a precision of ~ 100 Hz. From the frequency difference $\delta\nu$ of these two transitions, we extract the level splitting between the D and D' states of $\Delta E_{D,D'} = h\delta\nu$. In the experiment, we obtain a value of $\Delta E_{D,D'} = h \cdot 4.9740(1)$ MHz, corresponding to a magnetic field amplitude of $B = 2.9615(5)$ G. Finally, we generate a bichromatic Raman field by driving the single-pass AOM (sec. 4.4) at the two distinct radio frequencies $80 \text{ MHz} \pm \delta\nu$.

In order to simultaneously generate single photons on both transitions, we repeat the following sequence: after $800 \mu\text{s}$ of Doppler cooling the ion, optical pumping for $60 \mu\text{s}$ prepares the ion in the $|S_{1/2}, -\frac{1}{2}\rangle$ state. After $3 \mu\text{s}$ of waiting time, a bichromatic Raman pulse of $37 \mu\text{s}$ duration generates a single photon. For the atomic state detection, explained in more detail in sec. 8.5 and 5.4, we apply a $4 \mu\text{s}$ mapping pulse, an optional $4.3 \mu\text{s}$ rotation, and $500 \mu\text{s}$ of fluorescence detection. The repump lasers transfer all population back to the S manifold during the next Doppler cooling interval. In total, each sequence lasts 1.5 ms.

While the atom is measured in all attempts, the probability that a photon is detected on one of the APDs when the sequence is run is 5.7%. This overall efficiency is distributed over the efficiency of generating a photon (90%), the cavity output coupling of 20% (sec. 4.3), the optical path transmission of 80% and the mean APD detection efficiency of 40%.

The mean rate at which single photons are detected is 40.5 events/s. A faster detection rate could be achieved by triggering ion-state readout on the detection of a photon. In the case of no photon detection, unnecessary heating due to detection settings of laser frequencies and intensities could be avoided and thus the Doppler cooling time could be reduced.

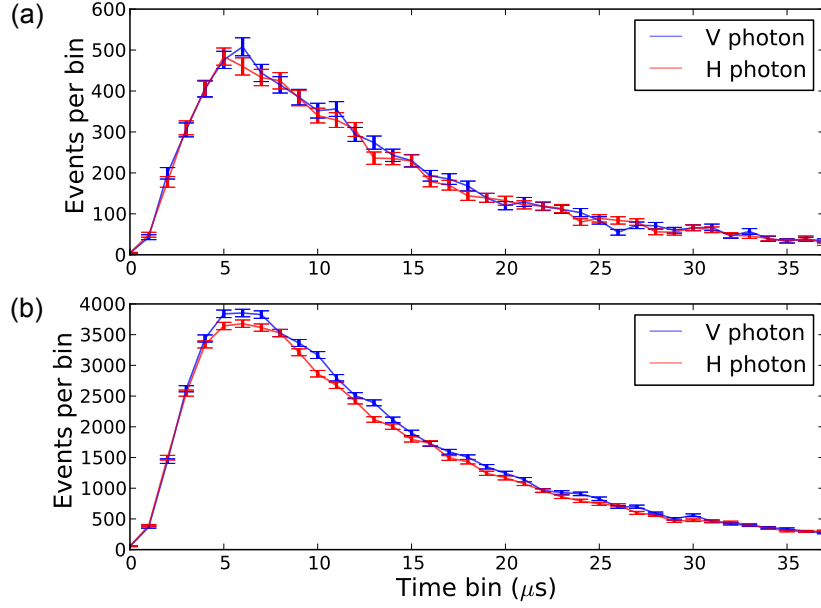


Figure 8.2: Temporal pulse shape of H and V cavity photons for simultaneous drive of the two Raman transitions. **(a)**, H, V photons for Raman phase 0.25π , containing $\sim 13,000$ events. The relative difference of the integrated curves is 1.4%. **(b)**, H, V photons for all eight measured Raman phases, containing $\sim 112,000$ events. The relative difference of the integrated curves is 2.4%.

In order to circumvent entanglement of the photon's polarization degree of freedom with its time-bin degree of freedom, it is necessary to overlap the two temporal pulse shapes of H and V photons. As discussed in sec. 8.6, only the Rabi frequencies Ω_1, Ω_2 should be used for this purpose, while the detunings Δ_1, Δ_2 should be fixed. In principle, the Rabi frequencies should be set according to the ratio of the transition strengths of $\sqrt{\frac{4/15}{2/3 \cdot 1/2}} \approx 0.9$ in order to drive both transitions with the same probability (sec. 7.1). In the experiment, however, we found the best overlap of the pulse shapes for the values $\Omega_{1,2}^{\text{drv}} = 2\pi \times (40, 50)$ MHz, resulting in a ratio of 0.8. The Rabi frequencies were calibrated via a measurement of the AC Stark shift of the Raman transition as a function of the Rabi frequency of the drive laser.

For a comparison of the probabilities of generating an H or V photon, the detection path efficiencies of the two output paths after the PBS have to be known. As these might change on the percent level from day to day in the lab, an easier and more robust alternative to daily measurement is to swap the paths between two measurements and add the events from corresponding channels. We thus perform two measurements for every photon polarization detection setting.

Fig. 8.2 demonstrates the identical pulse shapes of H and V photons resulting from the optimized ratio of Rabi frequencies. The data plotted here contain the subset of

the data further analyzed in sec. 8.5 and 8.7, in which photons were measured in the H/V basis. The data of fig. 8.2 (a) contain $\sim 13,000$ events, measured over the course of ~ 40 minutes. Here, the probability to generate an H photon is 1.4% smaller than to detect a V photon. For the data of fig. 8.2 (b), containing $\sim 112,000$ events measured over the course of six hours, the corresponding difference in probability is 2.4%. The causes and implications of this minor imbalance will be discussed in sec. 8.9.

In conclusion, we can accurately overlap the temporal pulse shapes of the orthogonally polarized photons on both transitions by optimizing the ratio of Rabi frequencies.

8.5 Quantum state tomography

Quantum systems are difficult to measure. This difficulty is based on the complex state space on the one hand and the change of a quantum state depending on how it is measured on the other hand. State tomography is a method which completely characterizes an ensemble of equally prepared quantum systems. It measures and reconstructs the density matrix of the system, from which all observables of interest can be calculated. As the density matrix can be decomposed into an operator basis, as can be seen in eq. 2.4 for a single qubit, the state can be reconstructed by measuring the expectation values of these operators, e.g., $(\sigma_x, \sigma_y, \sigma_z)$.

In a single-qubit experiment, however, one typically measures the expectation values of projectors \mathcal{P}_i onto the possible eigenstates of the Pauli operators, $\mathcal{P}_i \in \{|0\rangle\langle 0|, |1\rangle\langle 1|, |+_x\rangle\langle +_x|, |-_x\rangle\langle -_x|, |+_y\rangle\langle +_y|, |-_y\rangle\langle -_y|\}$, with $|\pm_x\rangle = \frac{1}{\sqrt{2}}(|0\rangle \pm |1\rangle)$ and $|\pm_y\rangle = \frac{1}{\sqrt{2}}(|0\rangle \pm i|1\rangle)$. The expectation values $\langle \sigma_i \rangle$ of eq. 2.4 can then be inferred from the expectation values of the projectors [108]. The density matrix describing a single qubit (eq. 2.3) has three free real parameters due to the requirement that ρ is hermitian and normalized (see section 2.1.2). If the expectation values of both projectors for each measurement setting are accessible, then three measurement settings, e.g. $(\sigma_x, \sigma_y, \sigma_z)$, are enough to completely determine ρ . For a system consisting of n qubits, access to expectation values of all projectors corresponding to all combinations of observables $\prod_{i,j,\dots} \mathcal{A}_i \mathcal{A}_j \dots$ must be available. In this case, 3^n measurement settings are necessary in order to determine the $4^n - 1$ free real parameters of ρ .

Provided the measurements have no noise or uncertainties, the expectation values $\langle \sigma_i \rangle$ to be inserted in eq. 2.4 can be obtained from a set of linear equations containing the projectors \mathcal{P}_i and the observables σ_i [148]. This *linear reconstruction* method has notable disadvantages. First, the density matrix obtained is not necessarily physical; solutions to this problem are discussed in [148]. Second, even for measurements without experimental imperfections, error estimation can be misleading as measurements are directly interpreted as probabilities rather than frequencies of occurrence [149]. Both problems are circumvented by using the *maximum likelihood* method [150]. Here, the density matrix that maximizes a likelihood functional is found in an opti-

setting	$\lambda/2$ angle (deg)	$\lambda/4$ angle (deg)
H/V	0	0
D/A	22.5	0
R/L	0	45
V/H	45	0
A/D	-22.5	0
L/R	0	-45

Table 8.1: Waveplate angles for the six polarization measurement settings.

mization routine. Constraints on the properties of ρ are contained in the functional, and renormalization can be applied after every optimization step, resulting in the physical density matrix which is most likely consistent with the measured data. Error bars are obtained by non-parametric bootstrapping [151, 152]. Assuming a multinomial distribution, Monte-Carlo simulations are used to simulate sets of data, for which new density matrices are reconstructed. From these matrices, standard deviations of any observable can be calculated.

In order to perform state tomography of the entangled ion-photon state, we have to measure the electronic state of the ion (section 5.4) and the polarization state of the photon. For these measurements, expectation values of all projectors are accessible in every setting. For the atom, both probabilities of being in the S or D state are obtained; for the photon, both outputs of the PBS are measured in each setting. It is therefore sufficient to measure ion and photon in all nine combinations of ion Pauli-operators $\{\sigma_x, \sigma_y, \sigma_z\}$ and photon polarization bases {horizontal/vertical (H/V), diagonal/anti-diagonal (D/A), right/left circular (R/L)} [108]. In order to measure the ion in all three bases, we first map the superposition of $\{D', D\}$ onto the $\{S, D\}$ states with a π pulse on the $S - D'$ transition [42, 43]. We then perform an optional $\pi/2$ pulse on the $S - D$ transition to select the measurement basis. Finally, states S and D are discriminated via fluorescence detection [75]. In order to measure the polarization of the photon, the cavity output path branches at a polarizing beamsplitter into two measurement paths. The angles of the half- and quarter-waveplate before the PBS determine the polarization basis, as documented in table 8.1. For each of these settings, we measure the ion in three bases, yielding $6 \times 3 = 18$ measurement settings for the full tomography. For given values of α and φ of eq. 8.2, we perform the full state tomography in order to obtain ρ . The fidelity with respect to a target state $|\psi\rangle$ is then calculated by the overlap $F \equiv \langle\psi|\rho|\psi\rangle$.

In a first set of measurements, we choose the case $\alpha = \pi/4$, corresponding to a maximally entangled state $|\psi\rangle$. For each of the 18 measurement settings, we record on average 4722 events in which a single photon has been detected. From the tomographic data, the density matrix is obtained via maximum likelihood reconstruction; we gratefully acknowledge the development of a computational toolbox in our group by

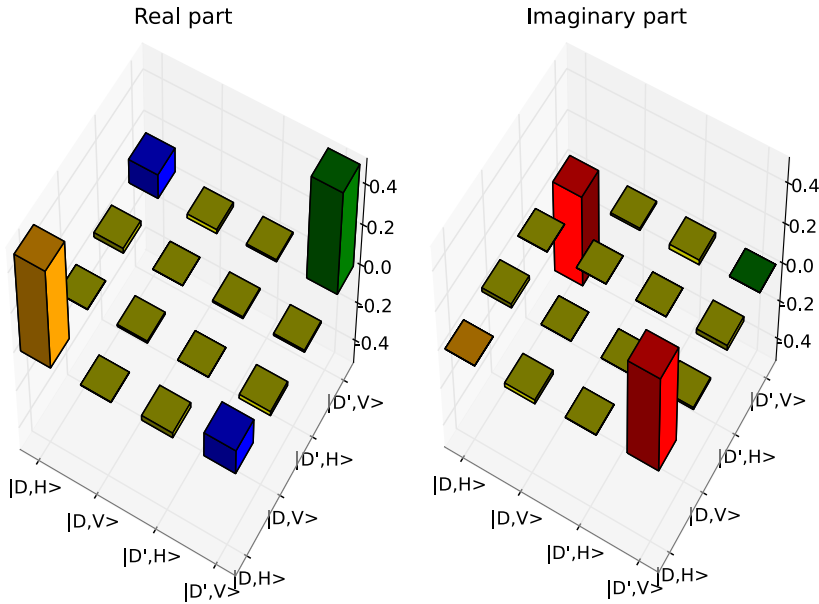


Figure 8.3: Quantum state tomography of the joint ion-photon state, containing $\sim 40,000$ events. Real and imaginary parts of all density matrix elements for Raman phase $\varphi = 0.25$, from which a fidelity $F = (97.4 \pm 0.2)\%$ is calculated. Colors for the density matrix elements correspond to those used in fig. 8.6.

Thomas Monz and Philipp Schindler [149]. The resulting density matrix is shown in fig. 8.3(a). In the ideal case, only populations at $|H, H\rangle$ and $|D', V\rangle$ are expected on the diagonal; the coherences between these two populations should be the only nonzero off-diagonal elements. The density matrix that we obtain almost perfectly resembles the ideal case. The relative size of the real and imaginary part of the coherences is determined by the phase φ of the state.

The fidelity yields a value of $F \equiv \langle \psi | \rho | \psi \rangle = (97.4 \pm 0.2)\%$ with respect to the maximally entangled state, placing our system definitively in the non-classical regime $F > 50\%$. The concurrence (eq. 8.1) is calculated to be $(95.2 \pm 0.5)\%$. We also use ion-photon entanglement to test a CHSH Bell-inequality, as described in section 8.2. While LHVMs require the Bell observable of the CHSH-inequality to be less than 2, we measure a value $(2.75 \pm 0.01) > 2$, where quantum mechanics provides an upper bound of $2\sqrt{2}$. The measurement thus violates the inequality by 75 standard deviations. The error bars of the stated values correspond to one standard deviation of the results obtained from Monte-Carlo simulations taking into account the number of measurements for each setting.

Time-resolved detection of the photons at both APDs allows for analysis of the entangled state as a function of photon detection time. This will be used in the following section in order to investigate phase evolution during the drive pulse. For

the results presented here, we have taken into account data from all time bins until the end of the 37 μs long drive pulse.

8.6 Time independence of the entangled state

The phase of the entangled atom-photon state is inferred from the measurements of photon polarization and atomic-state phase. In the experiments of refs. [25, 35, 126], although the phase of the entangled state is time-independent before photon detection, the phase of the atomic state after photon detection evolves due to Larmor precession. It is thus necessary to fix the time between photon detection and atomic state readout in order to measure the same φ for all realizations of the experiment. In contrast, for the case of Raman fields $\Omega_1 e^{i\omega_{l_1} t}$ and $\Omega_2 e^{i\omega_{l_2} t}$, the correct choice of frequency $\omega_{l_1} - \omega_{l_2} = \Delta E_{D,D'}/\hbar$ means that both the phase of the entangled atom-photon state before photon detection and the phase of the atomic state after photon detection are independent of photon-detection time. This result is explained here in two different approaches using the mathematical description introduced in sec. 2.3.

We define a model system with bases $\{|S, n\rangle, |P, n\rangle, |D, n\rangle, |D', n\rangle\}$, where $n = 0, 1$ is the photon number in either of the two degenerate cavity modes. The energies of the bare atomic states are $E_{S,P,D,D'} = \hbar\omega_{S,P,D,D'}$. As the cavity supports two degenerate polarization modes, the energy of a cavity photon of either mode is $E_c = \hbar\omega_c$. As shown in fig. 8.4, the $|S, n\rangle \leftrightarrow |P, n\rangle$ transition is driven by two fields $\Omega_i e^{i\omega_{l_i} t}$, ($i = 1, 2$) at detunings $\Delta_{l_i} = \omega_S - \omega_P - \omega_{l_i}$.

In the first approach, we choose the unitary transformation into a rotating frame

$$U = e^{-i\omega_{l_1} t |S\rangle\langle S|}. \quad (8.3)$$

After adiabatic elimination of the state $|P, n\rangle$ (see section 2.3), the Hamiltonian reads

$$\begin{aligned} \mathcal{H}/\hbar = & (\omega_S - \omega_P + \omega_{l_1}) |S\rangle\langle S| + (\omega_D - \omega_P) |D\rangle\langle D| + (\omega_{D'} - \omega_P) |D'\rangle\langle D'| \\ & + \omega_c |1\rangle\langle 1| + (g_1^{\text{eff}} |D, 1\rangle\langle S, 0| + g_2^{\text{eff}} |D', 1\rangle\langle S, 0| + \text{h.c.}), \end{aligned} \quad (8.4)$$

where the energy reference is the P state. If both Raman conditions hold, i.e., $\omega_S + \omega_{l_1} = \omega_D + \omega_c$ and $\omega_S + \omega_{l_2} = \omega_{D'} + \omega_c$, the states $|S, 0\rangle$ and $|D, 1\rangle$ are degenerate in this frame, and the couplings are

$$g_i^{\text{eff}} = \frac{(\Omega_1 + \Omega_2 e^{i(\omega_{l_2} - \omega_{l_1})t}) \cdot g}{2\Delta_{l_i}}. \quad (8.5)$$

The coupling between $|S, 0\rangle$ and $|D, 1\rangle$ has one constant and one time-dependent term. In the rotating-wave approximation, terms rotating much faster than the coupling are omitted [59]. As $|g_i^{\text{eff}}/(2\pi)| \approx \frac{30\text{MHz} \cdot 1.4\text{MHz}}{2 \cdot 400\text{MHz}} \approx 50 \text{ kHz} \ll |\omega_{l_1} - \omega_{l_2}| \approx 5 \text{ MHz}$, the time-dependent coupling between $|S, 0\rangle$ and $|D, 1\rangle$, which corresponds to off-resonant Raman coupling, is neglected. The coupling g_1^{eff} is then given by the time-independent

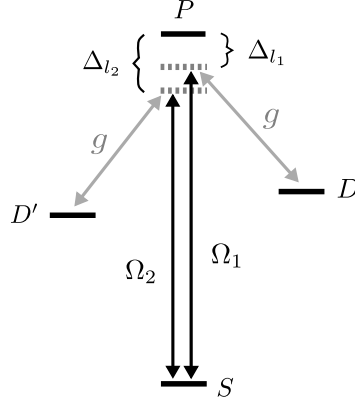


Figure 8.4: Model scheme of the entanglement protocol. Indicated are the relevant levels S, P, D, D' , the two driving fields with Rabi frequencies Ω_1, Ω_2 and detunings $\Delta_{l_1}, \Delta_{l_2}$, and the vacuum field of the cavity with coupling strength g . In the case shown, both Raman conditions $\Delta_{l_1} = (\omega_D - \omega_P) - \omega_c$ and $\Delta_{l_2} = (\omega_{D'} - \omega_P) - \omega_c$ are fulfilled. See text for the definition of $\omega_{S,P,D,D'}$ and ω_c .

term $\frac{\Omega_1 g}{2\Delta_{l_1}}$. The states $|S, 0\rangle$ and $|D', 1\rangle$ are split by $\hbar(\omega_{l_1} - \omega_{l_2})$ in this frame. Because of this energy splitting, the time-dependent term in g_2^{eff} resonantly drives the transition between $|S, 0\rangle$ and $|D', 1\rangle$, whereas the time-independent term is off-resonant. As a result, a Larmor precession of the entangled atom-photon state at frequency $\omega_{l_1} - \omega_{l_2}$ occurs during the Raman transition. The detection of a photon corresponds to a quantum jump and projects the system into a superposition of $|D, 0\rangle$ and $|D', 0\rangle$ [64]. Due to the energy splitting between the states $|D, 0\rangle$ and $|D', 0\rangle$ of $\Delta E = \hbar(\omega_D - \omega_{D'})$, a Larmor precession of the atomic superposition at frequency $\omega_D - \omega_{D'}$ is also present after photon detection. However, for the frequency choice $\omega_{l_1} - \omega_{l_2} = \omega_D - \omega_{D'}$, the frequencies of Larmor precession before and after photon detection are equal. As a result, the atomic superposition state does not depend on the photon detection time.

The Larmor precession during the entire time evolution of the system, both during Raman transfer and after photon detection, motivates a second approach. Here, a transformation into the rotating frame

$$U = e^{-i\omega_{l_1} t} |S\rangle\langle S| e^{-i(\omega_{l_1} - \omega_{l_2}) t} |D'\rangle\langle D'| \quad (8.6)$$

takes this precession into account. After adiabatic elimination of the state $|P, n\rangle$ (see section 2.3), the Hamiltonian now reads

$$\begin{aligned} \mathcal{H}/\hbar = & (\omega_S - \omega_P + \omega_{l_1}) |S\rangle\langle S| + (\omega_D - \omega_P) |D\rangle\langle D| \\ & + (\omega_{D'} - \omega_P + (\omega_{l_1} - \omega_{l_2})) |D'\rangle\langle D'| + \omega_c |1\rangle\langle 1| \\ & + (g_1^{\text{eff}} |D, 1\rangle\langle S, 0| + g_2^{\text{eff}} |D', 1\rangle\langle S, 0| + \text{h.c.}), \end{aligned} \quad (8.7)$$

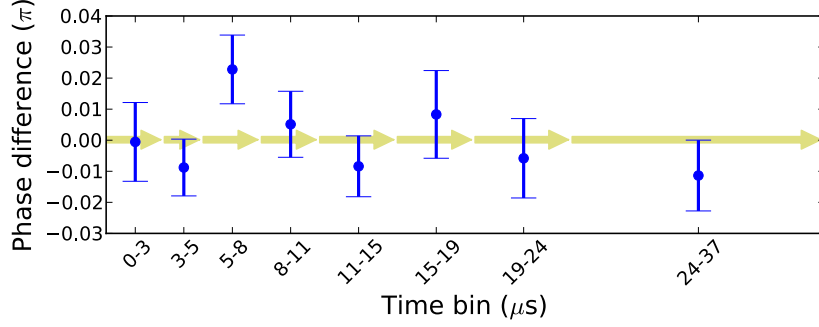


Figure 8.5: Phase of the ion-photon state vs. photon detection time. Arrows indicate time-bin intervals of the tomography data. Within error bars, the phase remains constant over the entire photon pulse shape.

where the energy reference is again the P state. If both Raman conditions hold, i.e., $\omega_S + \omega_{l_1} = \omega_D + \omega_c$ and $\omega_S + \omega_{l_2} = \omega_{D'} + \omega_c$, all three states $|S, 0\rangle$, $|D, 1\rangle$ and $|D', 1\rangle$ are degenerate in this frame, and the couplings are

$$g_1^{\text{eff}} = \frac{(\Omega_1 + \Omega_2 e^{i(\omega_{l_2} - \omega_{l_1})t}) \cdot g}{2\Delta_{l_1}}, \quad g_2^{\text{eff}} = \frac{(\Omega_2 + \Omega_1 e^{i(\omega_{l_1} - \omega_{l_2})t}) \cdot g}{2\Delta_{l_2}}. \quad (8.8)$$

In the rotating-wave approximation, time dependent terms in eq. 8.8 can be neglected, resulting in time-independent couplings between both $|S, 0\rangle$ and $|D, 1\rangle$ and $|S, 0\rangle$ and $|D', 1\rangle$. In this frame, there is thus no Larmor precession of the entangled atom-photon state during the Raman transfer. Since the states $|D, 0\rangle$ and $|D', 0\rangle$ are degenerate in this frame, there is also no Larmor precession of the atomic superposition state after photon detection. As a result, φ remains fixed both during Raman transfer and after photon detection.

In summary, the frequency difference $\omega_{l_1} - \omega_{l_2}$ of the two Raman fields should be set equal to the energy splitting $\omega_D - \omega_{D'}$ in order to obtain a constant phase φ for all photon detection times. Only the amplitudes Ω_1 and Ω_2 can thus be tuned in order to adjust the probabilities of the two Raman transitions with respect to each other.

In order to demonstrate that the photon detection time does not determine the phase φ of the state in the experiment, we extract this phase as a function of the photon detection time. For this purpose, we have defined photon time bins, each containing a similar number of detection events. For each bin, we extract the phase φ from state tomography of this data subset. As can be seen in fig. 8.5, the phase φ of the entangled state remains constant across all time bins, that is, during the entire drive pulse.

8.7 Tunable phase of the entangled state

The ability to tune the entangled atom-photon state is a valuable resource for various schemes in quantum communication. A tunable state has for example been employed for teleportation [31] and a heralded gate between remote qubits [130]. In quantum computation, the tunability of controlled phase shift gates between multiple qubits reduces the required number of gates in the quantum Fourier transform [153]. It thus may also be very useful to be able to control all parameters of the entangled atom-photon state for future applications in which multiple nodes of a quantum network are connected.

We first establish that we can control the phase φ of the final entangled state $|\psi\rangle$ over the full range from 0 to 2π via tuning the Raman phase φ_{Raman} . For this measurement, we set the amplitudes of $|\psi\rangle$ to $\alpha = \pi/4$, corresponding to a maximally entangled state.

The phase φ of the resulting state depends on the definition of the basis in the data analysis. The Raman phase φ_{Raman} , on the other hand, is set by the phase between the two radio frequencies generated by the DDS (sec. 4.11). In order to find the relation between φ and φ_{Raman} , we perform a full state tomography for each value of φ_{Raman} and find the phase φ that optimizes the overlap with a maximally entangled state. The linear relation obtained is then used for the calculation of the fidelity as a calibration measurement.

For eight different values of φ_{Raman} , we perform full state tomography. The real and imaginary parts of the coherence $\rho_{14} = \langle D, H | \rho | D', V \rangle$ vary sinusoidally as a function of φ_{Raman} (fig. 8.6(a)). Both curves are fitted simultaneously, with the phase offset constrained to $\pi/2$. The amplitude fit parameter yields a value of $(94.2 \pm 0.3)\%$ for the real part and $(97.5 \pm 0.5)\%$ for the imaginary part. The fidelity has a mean value of $(96.9 \pm 0.1)\%$ and varies only slightly within error bars (fig. 8.6(b)). These error bars correspond to one standard deviation of the values obtained by parametric bootstrapping (sec.8.5) and thus contain only the statistical errors given by the finite number of measured events. As the data for the eight settings of the Raman phase contains $\sim 340,000$ events measured with the same ion over the course of ~ 6 hours, transition probabilities slightly fluctuate on the timescale between measurements (sec. 8.9), resulting in an additional error of $\sim 0.5\%$. Considering both error sources, all target states have been generated with high fidelity independent of the Raman phase.

8.8 Tunable amplitudes of the entangled state

The fact that the entangled state amplitudes are tunable opens up new possibilities in quantum networks as well as for fundamental studies of quantum mechanics. In a quantum network, a tunable state at one quantum node could be used to match the amplitudes of a state at a second node for which transition amplitudes are fixed

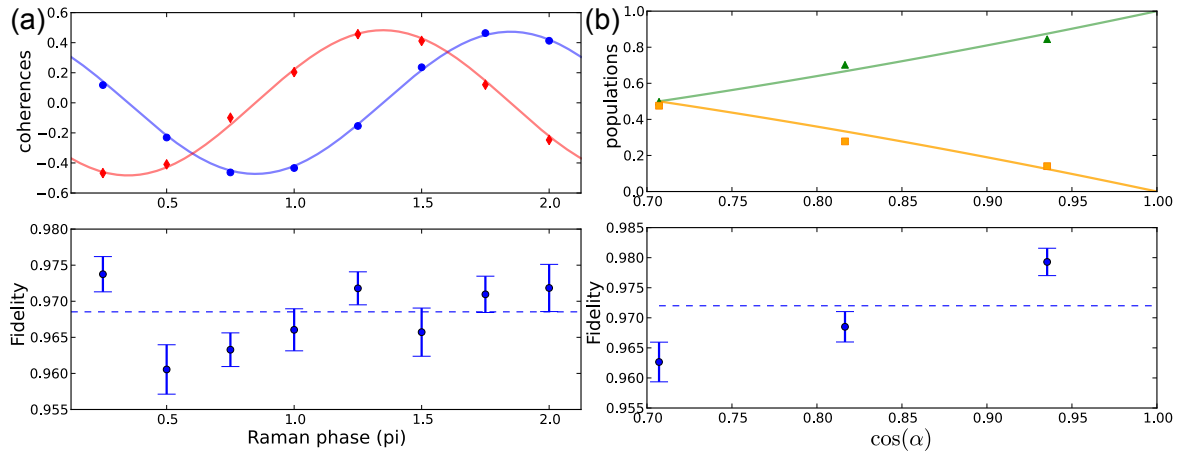


Figure 8.6: (a) State tomography as a function of Raman phase ($\sim 340,000$ events). Upper graph: $\text{Re}(\rho_{14})$ (blue circles) and $\text{Im}(\rho_{14})$ (red diamonds) as a function of Raman phase. Error bars are smaller than the size of the symbols. Each value is extracted from a full state tomography of ρ as in fig 8.3a. Both curves are fitted simultaneously, with phase offset constrained to $\pi/2$. The fit contrast is 95.6(4)%. Lower graph: fidelities of the eight states, with a dashed line indicating the mean value. (b) State tomography for three values of amplitude $\cos \alpha$. Upper graph: the density matrix elements ρ_{11} (orange squares) and ρ_{44} (green triangles) are plotted for the three target amplitudes $\cos \alpha = \{1/\sqrt{2}, 1/\sqrt{3}, 1/\sqrt{8}\}$. Error bars are smaller than the size of the symbols. Solid lines represent the amplitudes of the target states. Lower graph: the corresponding fidelities are $F = \{96.3(3), 96.8(3), 98.0(4)\}$. A dashed line indicates the mean value.

by atomic transition strengths and/or geometry factors [25]. For a loophole-free test of Bell inequalities, an asymmetric, non-maximally entangled atom-photon state has been proposed to reduce the detection-efficiency threshold necessary for closing the detection loophole [143].

A second measurement set demonstrates control over the amplitudes $\cos \alpha$ and $\sin \alpha$ of the entangled ion-photon state. After selecting three target amplitudes $\cos \alpha = \{1/\sqrt{2}, 1/\sqrt{3}, 1/\sqrt{8}\}$, we generate each corresponding state by adjusting the Raman field amplitudes, since α is a function of the ratio Ω_2/Ω_1 . The density matrix for each state is then measured via tomography. In the upper graph of fig. 8.6(b), the populations $\rho_{11} \equiv \langle DH | \rho | DH \rangle$ and $\rho_{44} \equiv \langle D'V | \rho | D'V \rangle$ for the three target amplitudes agree well with theoretical values. The fidelities of the asymmetric states, plotted in the lower graph of fig. 8.6(b), are as high as those of the maximally entangled states and are limited by the populations, that is, by errors in tuning the Raman fields to match the target values.

8.9 Experimental imperfections

In previous atom-photon entanglement experiments, typical error sources include imperfect atomic state detection [21, 146], atomic decoherence [129] and multiple excitations of the atom [25]. These sources play a minor role in the experiment presented here. For atomic state discrimination, a signal-to-noise ratio above 100 is obtained at a fluorescence rate of 50 kHz and a background rate below 0.5 kHz. With the chosen detection time of 500 μs , the atom detection error is less than 10^{-3} (sec. 5.4). The measurement of the atomic coherence time for a superposition of the D and D' states was described in sec. 5.7. For the relevant time scale of this experiment, i.e., the 40 μs interval between the start of the drive pulse and atomic state detection, the measured Ramsey contrast remains constant at the value of 98.4%, exhibiting no loss in atomic coherence during this interval. Multiple excitations of the atom can only occur if the atom decays from the metastable $D_{5/2}$ manifold back to the $S_{1/2}$ manifold during the drive pulse. Given the lifetime $\tau = 1.168$ s of the metastable $D_{5/2}$ manifold [77], this process occurs with probability $1 - \exp(-\frac{0.04\text{ms}}{1168\text{ms}}) \approx 3 \cdot 10^{-5}$ and can thus be neglected. This small probability for multiple excitations also manifests itself in the excellent, dark-count-limited two-photon suppression of $3 \cdot 10^{-4}$ in the single-photon source [27].

Misalignment of the measurement axes and the drive beam propagation axis with respect to the cavity axes also constitute a minor error $\ll 1\%$ (sec. 4.10).

Another possible error source is the process where the ion stays in the $|S_{1/2}, -\frac{1}{2}\rangle$ state during Raman excitation without producing a photon. In this case, the $|S_{1/2}, -\frac{1}{2}\rangle$ population is transferred to the $|D_{5/2}, -\frac{5}{2}\rangle$ state during state detection, leading to false events in the case of a dark ion, interpreted as the ion being in the $|D_{5/2}, -\frac{3}{2}\rangle$ state. This process could be avoided by shelving all remaining $|S_{1/2}, -\frac{1}{2}\rangle$ population

to another $D_{5/2}$ state before state detection and further analysis pulses. However, the remaining $|S_{1/2}, -\frac{1}{2}\rangle$ state population in the experiment is negligible after Raman excitation. We conclude that all of these error sources reduce the fidelity by less than 1%.

The largest error source which limits the fidelity is caused by dark counts of the APDs at a rate of 36 Hz. In a test analysis, we assume that dark counts contribute to APD detection events in a way uncorrelated with the atom. Only for the purpose of an error estimation, we subtract dark counts from the measured atom-photon correlations and obtain a fidelity of the reconstructed state of 98.9% for the data of fig. 8.3. The dark counts thus limit the fidelity by 1.5%.

The second-largest reduction in fidelity is due to the imperfect ratio of driving probabilities of the two Raman transitions, resulting in unequal populations of the ideal maximally entangled state ($\cos \alpha$ and $\sin \alpha$ in eq. 8.2). The transition probabilities are given by the Rabi frequencies and the detuning of each field from Raman resonance. The Rabi frequencies are set by variable RF-attenuators (sec. 4.4), which might drift with temperature over the hour-long timescales of data acquisition. The Raman detunings are set via the radio frequencies generated by the DDS. However, as the two Raman transitions do not perfectly overlap in frequency due to a differential AC stark shift, the transition probabilities might change if the laser frequency drifts by ~ 5 kHz due to a temperature change of the locking cavity. For the data of fig. 8.3, which were taken over the course of 40 minutes, the relative difference in total counts of H and V photons is 1.4% (fig. 8.2(a)). As populations in ρ contribute to one-half the fidelity, while the other half is given by the coherences, this imbalance results in a reduction of the fidelity of 0.7%. The relative wavepacket mismatch of H and V photons of the data from all eight Raman phase measurements (fig. 8.6), taken over the course of six hours, is 2.4% (fig. 8.2(b)), and corresponds to a fidelity reduction of 1.2%.

As apparent in the offset of the Ramsey fringe amplitude at zero waiting time (sec. 5.7), imperfect initialization and manipulation of the ion due to its finite temperature and laser intensity fluctuations decrease the fidelity by $\sim 0.8\%$.

8.10 Conclusion

To our knowledge, this measurement represents both the highest fidelity and the fastest rate of entanglement detection to date between a photon and a single-emitter quantum memory. This detection rate is limited by the fact that most cavity photons are absorbed or scattered by the mirror coatings, and only 16% enter the output mode. The cavity mirrors in this setup have transmission $T_1 = 13$ ppm and $T_2 = 1.3$ ppm, with combined losses of 68 ppm. State-of-the-art combined losses at this wavelength are $L = 4$ ppm [154]. In our cavity, these losses would correspond to an output coupling efficiency of $T_1/(T_1 + T_2 + L) = 71\%$. To improve this efficiency, an output mirror

with higher transmission T_1 could be used; for example, $T_1 = 500$ ppm corresponds to an efficiency of 99%. The cavity decay rate κ would also increase, but single-photon generation with near-unit efficiency is still valid in the bad-cavity regime [128].

In contrast, without a cavity, using a lens of numerical aperture 0.5 to collect photons, the efficiency would be 6.7%. In addition, the infrared wavelength of the output photons is well-suited to fiber distribution, enabling long-distance quantum networks. We note that a faster detection rate could be achieved by triggering ion-state readout on the detection of a photon.

We have demonstrated full control of the phase and amplitude of an entangled ion-photon state, which opens up new possibilities for quantum communication schemes. In contrast to monochromatic schemes, evolution of the relative phase of the atomic state after photon detection is determined only by the start time of the experiment and not by the photon-detection time. The state $|\psi\rangle$ is in this sense predetermined and can be stored in, or extracted from, a quantum memory in a time-independent manner.

9 Ion-photon state mapping

Alternatively to atom-photon entanglement, direct state transfer is a second protocol that enables quantum communication between distant nodes of a quantum network. Such direct state transfer makes use of state mapping between atom and photon. In this chapter, we demonstrate the faithful mapping of a quantum state from a single ion onto a single photon within an optical cavity. The mapping process is time-independent, allowing us to characterize the interplay between efficiency and fidelity. As the techniques for coherent manipulation and storage of multiple ions at a single quantum node are well established [42, 43], this process offers a promising route toward networks between ion-based quantum computers. The results of this chapter are submitted for publication [54].

9.1 Description of the protocol

In the original proposal for quantum-state transfer [41], a photonic qubit comprises the number states $|0\rangle$ and $|1\rangle$. Such a qubit was subsequently employed for the cavity-based mapping of a coherent state onto an atom [29]. However, due to losses in a realistic optical path, it is advantageous instead to encode the qubit within a degree of freedom of a single photon. As a frequency qubit [31] would be challenging to realize reversibly within a cavity, we choose the polarization degree of freedom, as for ion-photon entanglement in the previous chapter. The target process then maps an electronic superposition of atomic states $|S\rangle$ and $|S'\rangle$ to the polarization state $|H\rangle$ and $|V\rangle$ of a photon,

$$(\cos \alpha |S\rangle + e^{i\varphi} \sin \alpha |S'\rangle) \otimes |0\rangle \longrightarrow |D\rangle \otimes (\cos \alpha |H\rangle + e^{i\varphi} \sin \alpha |V\rangle), \quad (9.1)$$

preserving the superposition's phase and amplitude, defined by φ and α ; $|D\rangle$ is a third atomic state.

9.2 Implementation of the protocol

For the implementation of state mapping protocol, just as for the entanglement protocol previously, we again employ two phase-stable driving fields. In contrast to the entanglement protocol, here, by coupling two initial atomic states to one final state, the ion's electronic state is transferred coherently to the photon, and no information remains in the ion. The crux of this mapping problem is to maintain amplitude and phase relationships during the transfer process.

As the coherence of the mapping process will be destroyed by any off-resonant scattering, two atomic transitions should be chosen that maximize the coherent ion-cavity interaction (sec. 7.1). For the ion-photon entanglement, the choice of a σ^- -polarized driving beam at 393 nm resulted in a robust situation: the Clebsch-Gordan coefficients of the $S_{1/2} \leftrightarrow P_{3/2}$ transition were maximal, and any scattering from the $P_{3/2}$ state automatically re-initialized the correct $S_{1/2}$ state. Experimentally, we were able to accurately adjust the polarization of this beam via the fluorescence signal of the ion.

For state mapping, it at first appeared straightforward to keep the experimental geometry for entanglement, i.e., the orientation of the magnetic field axis, the orientation of the drive laser beam, and the polarization of this beam with respect to the cavity and trap axes. In this scenario, the protocol could be realized by transferring the initial superposition of $|S\rangle \equiv |S_{1/2}, -\frac{1}{2}\rangle$ and $|S'\rangle \equiv |S_{1/2}, +\frac{1}{2}\rangle$ to the final atomic target state $|D_{5/2}, -\frac{3}{2}\rangle$ via two distinct Raman transitions (fig. 9.1(a)), as we proposed in [52]. If the initial state was $|S\rangle$, the photon would be in a vertically polarized state $|H\rangle$; if the initial state was $|S'\rangle$, a horizontally polarized photon $|V\rangle$ would be generated. As the polarization modes of the cavity are degenerate, entanglement of the polarization with the frequency degree of freedom is avoided. The geometric factors that enter the transition strengths of the two Raman transitions involved, as introduced in eq. (7.1), are:

$$\text{for } |S_{1/2}, -\frac{1}{2}\rangle \leftrightarrow |P_{3/2}, -\frac{3}{2}\rangle \leftrightarrow |D_{5/2}, -\frac{3}{2}\rangle : \quad \alpha_i \cdot \beta_j = \sqrt{\frac{4}{15}} \approx 0.52 \quad (9.2)$$

$$\text{for } |S_{1/2}, +\frac{1}{2}\rangle \leftrightarrow |P_{3/2}, -\frac{1}{2}\rangle \leftrightarrow |D_{5/2}, -\frac{3}{2}\rangle : \quad \alpha_i \cdot \beta_j = \sqrt{\frac{1}{3} \cdot \frac{2}{5} \cdot \frac{1}{2}} \approx 0.26 \quad (9.3)$$

On the one hand, the selected transitions fulfill the requirement of strong and similar coupling strengths (compared to other transitions indicated in fig. 7.1); in order to preserve the amplitudes of the initial state during mapping, the difference in transition strengths by a factor of two can be compensated for using the Rabi frequencies of the bichromatic field.

On the other hand, a problem arises with the time independence of the mapping process. This time independence was of fundamental importance for the entanglement scheme: by choosing the difference frequency of the lasers to match the energy splitting of the target states, the phase evolution of the entangled state over time vanished and the state could be read out at any time. For the proposed state-mapping scheme, the following problem arises: due to the different Clebsch-Gordan coefficients of the $S_{1/2} \leftrightarrow P_{3/2}$ transitions (indicated in fig. 9.1), a differential AC-Stark shift between the initial states $S = |S_{1/2}, -\frac{1}{2}\rangle$ and $S' = |S_{1/2}, +\frac{1}{2}\rangle$ would be introduced. This differential AC-Stark shift is calculated via eq. (2.28) and corresponds to a frequency difference

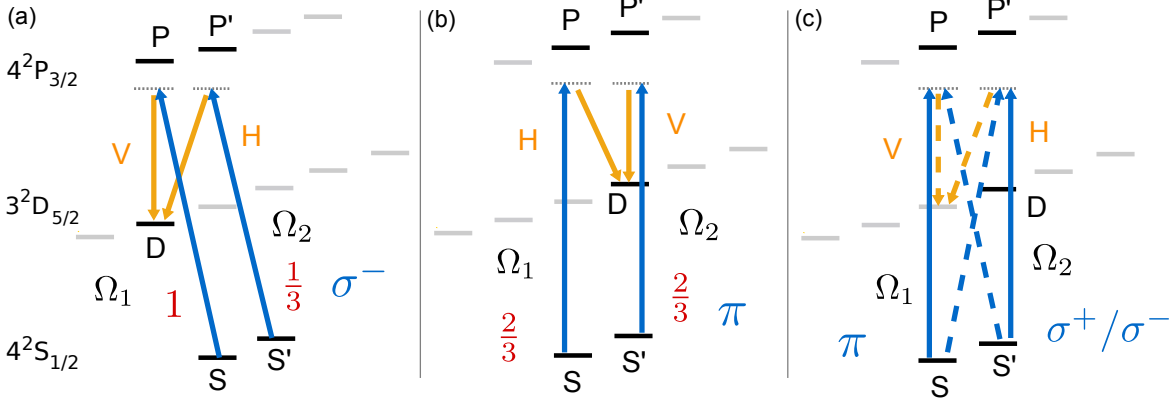


Figure 9.1: Different driving schemes for ion-photon state mapping. Indicated are the Clebsch-Gordan coefficients of the $S_{1/2} \leftrightarrow P_{3/2}$ transitions and the Rabi frequencies of the bichromatic driving field Ω_1 and Ω_2 . **(a)** σ^- -beam driving scheme. The different Clebsch-Gordan coefficients (indicated in red) result in a differential AC-Stark shift of the atomic-qubit levels S and S' . We therefore avoid this scheme, although we initially proposed it in [52]. **(b)** π -beam driving scheme without AC-Stark shift between S and S' . We choose this scheme in the experiment. **(c)** Wrong polarization components σ^+/σ^- (blue dotted lines) result in two unwanted effects: first, Raman transitions generate photons with unwanted polarizations (orange dotted lines). Second, Raman transitions between S and S' are driven that introduce a spin flip error to the atomic qubit.

of

$$\Delta\nu_{\text{AC-Stark}}^{S,S'} \approx \frac{\Omega_0^2}{4\pi\Delta_{l,c}} \left(1 - \sqrt{\frac{1}{3}}\right) \approx 200 \text{ kHz} \quad (9.4)$$

for a typical Rabi frequency of $\Omega_0 = (2\pi) \times 20$ MHz and Raman detuning of $\Delta_{l,c} = (2\pi) \times 400$ MHz. The phase of the initial state would thus precess at frequency $\nu_{\text{AC-Stark}}^{S,S'}$. As a consequence, the phase of the final photonic state would depend on the photon detection time within the photon time window of $\geq 10 \mu\text{s}$.

In principle, this differential AC-Stark shift could be compensated for via the difference detuning of the driving field $\Delta_1 - \Delta_2$. As the shift depends on the Rabi frequency of the bichromatic field, however, a calibration would represent a time-consuming experimental procedure. Additionally, intensity fluctuations of the drive beam could influence the fidelity of the mapping process.

A more robust alternative can be realized by a second driving scheme: applying a π -polarized drive beam, two Raman transitions can be driven that both end at $|D_{5/2, +\frac{1}{2}}\rangle$, as indicated in fig. 9.1(b). In this scenario, the photon is in a horizontally polarized state $|H\rangle$ if the initial state was $|S\rangle$; if the initial state was $|S'\rangle$, a vertically polarized photon $|V\rangle$ is generated. The transition strengths of the two Raman

transitions involved are exactly the same as for the previous scheme:

$$\text{for } |S_{1/2}, -\frac{1}{2}\rangle \leftrightarrow |P_{3/2}, -\frac{1}{2}\rangle \leftrightarrow |D_{5/2}, +\frac{1}{2}\rangle : \quad \alpha_i \cdot \beta_j = \sqrt{\frac{2}{3} \cdot \frac{2}{5}} \approx 0.52 \quad (9.5)$$

$$\text{for } |S_{1/2}, +\frac{1}{2}\rangle \leftrightarrow |P_{3/2}, +\frac{1}{2}\rangle \leftrightarrow |D_{5/2}, +\frac{1}{2}\rangle : \quad \alpha_i \cdot \beta_j = \sqrt{\frac{2}{3} \cdot \frac{1}{5} \cdot \frac{1}{2}} \approx 0.26 \quad (9.6)$$

In contrast to the previous scheme, however, differential AC-Stark shifts caused by different Clebsch-Gordan coefficients of the $S_{1/2} \leftrightarrow P_{3/2}$ transitions are avoided.

In order to realize this π -beam driving scheme in the laboratory, the polarization of the drive field has to be carefully aligned. If any σ -component of the drive beam polarization is present, unwanted Raman transitions could be driven in which a photon with unwanted polarization is generated (fig. 9.1(c)), corresponding to a spin flip error of the photonic qubit. Moreover, Raman transitions between S and S' would be driven without generating a photon in the resonator.

In the experiment, the propagation direction of the 393 nm drive beam is unchanged from the ion-photon entanglement measurement, but the magnetic-field direction is now orthogonal both to the cavity axis and to the drive-beam's propagation direction (the magnetic field is now oriented along the y axis of fig. 8.1). Additionally, we increase the amplitude of the magnetic field to 4.5 G for optimal separation of the target carrier transitions from the motional sidebands of neighboring transitions (fig. 7.4(a)). For optimizing the drive beam's linear polarization, we employ the population transfer caused by the undesirable Raman transition between S and S' as a signal. With the laser at 393 nm detuned by ≈ 4 GHz from the $S_{1/2} \leftrightarrow P_{3/2}$ transition, we minimize the population transfer such that after 2 ms less than 10% of the S state population is transferred to the S' state. At this suppression, population transfer between the S and S' state during the mapping process is negligible compared to off-resonant scattering (sec. 9.4).

For both schemes discussed in this section, there are two other origins of differential AC-Stark shifts between the two Raman transitions: the different Clebsch-Gordan coefficients on the cavity transitions ($P_{3/2} \leftrightarrow D_{5/2}$) and the different detuning of the bichromatic field from the two $S_{1/2} \leftrightarrow P_{3/2}$ transitions. The different Clebsch-Gordan coefficients on the cavity transition result in a shift on the order of 1 kHz, while the different detuning results in a shift on the order of 5 kHz for the values of Ω_0 and $\Delta_{l,c}$ given above. At the corresponding time scale of photon detection of $\geq 200 \mu\text{s}$, the coherence of the photonic state, however, is limited by other processes (as will be described in sec. 9.4), and these two shifts can therefore be neglected in our experiment.

9.3 Quantum process tomography

The mapping process of eq. (9.1) is characterized via process tomography, in which the bichromatic Raman transition is applied to four orthogonal initial states of the

atom: $|S\rangle$, $|S'\rangle$, $|S - S'\rangle$, $|S + iS'\rangle$. Following optical pumping to the Zeeman state $|S\rangle$, the atomic qubit is encoded in the states $|S\rangle$ and $|S'\rangle$ via two laser pulses on the quadrupole transition that couples the $S_{1/2}$ and $D_{5/2}$ manifolds. The length and phase of a first pulse on the $|S\rangle \leftrightarrow |D_{5/2}, m_J = -1/2\rangle$ transition set the amplitude and phase of the initial state. The state is subsequently transferred back to the S manifold via a π -pulse on the $|D_{5/2}, m_J = -1/2\rangle \leftrightarrow |S'\rangle$ transition. For each input state, we measure the polarization state of the output photon via state tomography, using three orthogonal measurement settings (fig. 8.1 and table 8.1).

Process tomography extracts the process matrix χ , which parameterizes the map from an arbitrary input density matrix ρ_{in} to its corresponding output state ρ_{out} in the basis of the Pauli operators $\sigma_{0,1,2,3} \equiv \{\mathbb{1}, \sigma_x, \sigma_y, \sigma_z\}$:

$$\rho_{\text{out}} = \sum_{i,j} \chi_{i,j} \sigma_i \rho_{\text{in}} \sigma_j. \quad (9.7)$$

As the ideal mapping process preserves the qubit, the overlap $\chi_{0,0}$ with the identity should be equal to one. We identify $\chi_{0,0}$ as the process fidelity, which quantifies the success of the mapping. A maximum likelihood reconstruction [155] of χ for the experimental data is plotted in fig. 9.2(a) for a 2 μs window of photons exiting the cavity. Here the matrix element $\chi_{0,0}$ indicates a process fidelity of $(92 \pm 2)\%$, well above the classical threshold of $1/2$. Other diagonal elements $\chi_{1,1} = (3 \pm 1)\%$ and $\chi_{3,3} = (4 \pm 2)\%$ reveal a minor depolarization of the quantum state.

Another metric for quantum processes is the mean state fidelity, which evaluates the state fidelities $\langle \psi_{\text{in}}^i | \rho_{\text{out}}^i | \psi_{\text{in}}^i \rangle$ for a set of input states $|\psi_{\text{in}}^i\rangle$, where ρ_{out}^i represent the corresponding photon output states. The mean state fidelity can also be directly extracted from the process fidelity for an ideal unitary process [156]. For each of our four input states, state tomography of the output photon is shown in fig. 9.2b, using the same photon collection window as in fig. 9.2a. The corresponding state fidelities are $(96 \pm 1)\%$ for $|S\rangle$, $(94 \pm 2)\%$ for $|S'\rangle$, $(97 \pm 2)\%$ for $|S - S'\rangle$, and $(95 \pm 2)\%$ for $|S + iS'\rangle$, yielding a mean of $(96 \pm 1)\%$. This agrees with the value of $(95 \pm 1)\%$ extracted from the process fidelity and exceeds the classical threshold [156] of $2/3$.

9.4 Time evolution of the photon polarization

We now consider the evolution over time of the photonic output states ρ_{out}^i generated from these four atomic input states. In fig. 9.2(c), we plot the temporal shape of the emitted photon in each of three measurement bases, a total of 12 cases. For each input state, there exists one polarization measurement basis in which photons would ideally impinge on only one detector. If the ion is prepared in the state $|S\rangle$ and measured in the H/V polarization basis, for example, the mapping scheme of fig. 9.1(b) should only produce the photon state $|H\rangle$. However, a few microseconds after the Raman driving field is switched on, we see that the photon state $|V\rangle$ appears and is generated

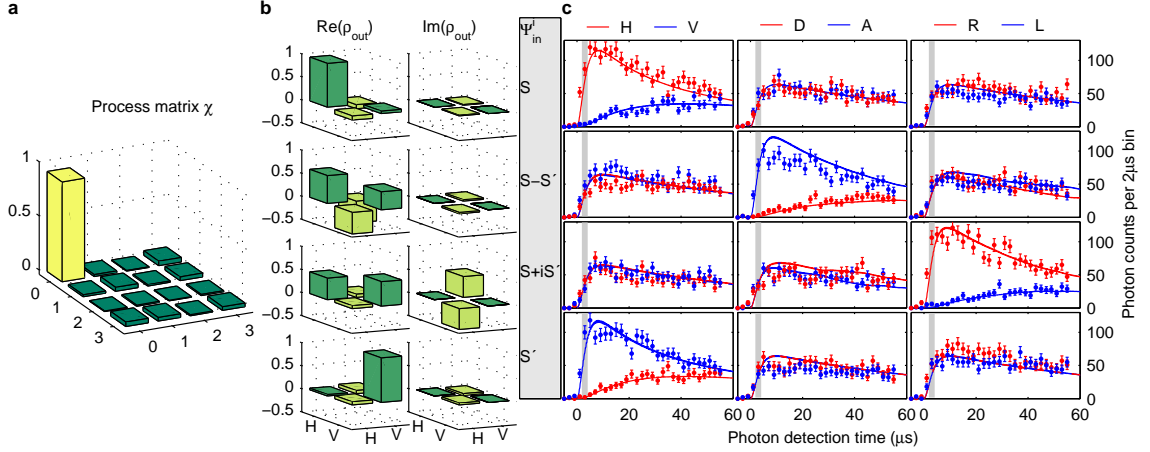


Figure 9.2: Process and state fidelities of the ion–photon mapping. (a), Absolute values of the process matrix χ reconstructed from cavity photons detected between 2 μs and 4 μs after the bichromatic field is switched on at time = 0. (b), State tomography of photons in the same time window for the four input states $|S\rangle$, $|S - S'\rangle$, $|S + iS'\rangle$, and $|S'\rangle$, shown in rows from top to bottom. (c), Each state tomography corresponds to measurements in the three bases H/V , D/A , and R/L (columns). For each input state, the temporal shapes of single photons are plotted in red for polarizations H, D, R and in blue for polarizations V, A, L . In each row, in two of three columns, photons are equally distributed over both detectors, while in the third, photons are generated ideally with a single polarization. Master-equation simulations (red and blue lines) successfully reproduce the observed dynamics. The grey shaded area indicates the time window used for tomography.

with increasing probability over the next 55 μs . The mechanism here is off-resonant excitation of the $4^2P_{3/2}$ manifold and decay to the previously unpopulated state $|S'\rangle$, followed by a Raman transition generating the ‘wrong’ polarization. If the ion is prepared in $|S'\rangle$, the temporal photon shapes are inverted and symmetric, with the initial state $|V\rangle$ followed by the gradual emergence of $|H\rangle$. We have confirmed this process through master-equation simulations of the ion–cavity system, also plotted in fig. 9.2(c). These simulations will be described in more detail in Birgit Brandstätter’s thesis [83].

For the superposition input states $|S - S'\rangle$ and $|S + iS'\rangle$, the mapping generates a photon with anti-diagonal polarization $A = (H - V)/\sqrt{2}$ and right-circular polarization $R = (H + iV)/\sqrt{2}$, respectively. Thus, photons impinge predominantly on one detector in the diagonal(D)/anti-diagonal(A) and right(R)/left(L) bases, where D and L are defined in table 2.1. Here, as for states $|S\rangle$ and $|S'\rangle$, photons with the ‘wrong’ polarization are due to off-resonant scattering before the mapping occurs. In this case, scattering destroys the phase relationship between the S and S' components. (Note that for eight of the cases in fig. 9.2c, the measurement basis projects the photon polarization onto the two detection paths with equal probability.)

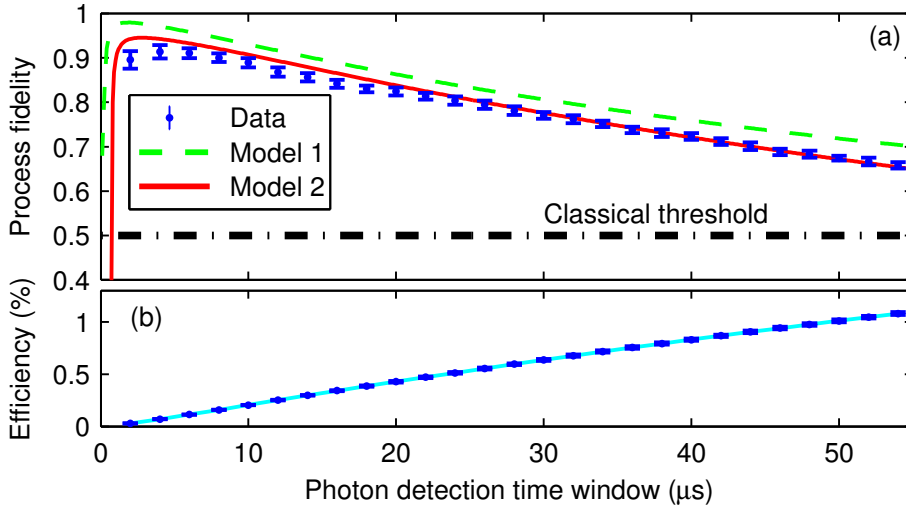


Figure 9.3: Time dependence of process fidelity and efficiency. (a), Cumulative process fidelity and (b), process efficiency are plotted as a function of the photon-detection time window, where error bars represent one standard deviation. A green dashed line indicates the simulated process fidelity for the same parameters as in fig. 9.2. To this model, we now add the effects of detector dark counts, imperfect state initialization, and magnetic-field fluctuations, quantified in independent measurements, with the result indicated by a red line. A fit to the process efficiency is used to weight the effect of dark counts. The second model, including detector dark counts etc., agrees well with the data, while the first one represents achievable values for this ion-cavity system.

The accumulation of scattering events over time suggests that the best mapping fidelities can be achieved by taking into account only photons detected within a certain time window. Such a window is used for the preceding analysis of process and state fidelities. For each attempt to prepare and map the ion’s state, the probability to detect a photon within this window is $4 \cdot 10^{-4}$, which we identify as the process efficiency. This efficiency can be increased at the expense of fidelity by considering a broader time window. Fig. 9.3 shows both the cumulative process fidelity and efficiency as a function of the photon-detection window. The fidelity initially increases because at short times (< 100 ns), photons are produced primarily via the off-resonant rather than the resonant component of the Raman process and thus are not in the target polarization state. This coherent effect, which we have investigated through simulations, is quickly damped due to the low amplitude of off-resonant Raman transitions. The cumulative process fidelity reaches a maximum between $2 \mu\text{s}$ and $4 \mu\text{s}$ after the bichromatic driving field is switched on, the time interval used to analyze the data of fig. 9.2(a) and (b). The fidelity then slowly decreases as a function of time due to the increased likelihood of off-resonant scattering.

If all photons detected within $55 \mu\text{s}$ are taken into account, the process efficiency exceeds 1%, while the process fidelity of $(66 \pm 1\%)$ remains above the classical threshold of $1/2$. This process efficiency includes losses in the cavity mirrors, output path, and detectors. The corresponding probability for state transfer within the cavity is 14.7%. A longer detection time window would allow transfer probabilities approaching one, but fidelities would fall below the classical threshold. Simulations that include the effects of detector dark counts, imperfect state initialization, and magnetic-field fluctuations agree well with the data of fig. 9.3. In the absence of these three effects, simulations indicate that fidelities of 98% would be possible in our ion-cavity system.

The atomic superposition of $|S\rangle$ and $|S'\rangle$ experiences a 12.6 MHz Larmor precession, which corresponds to a rotation of the states' relative phase at this frequency. One might expect that as a result, it would not be possible to bin data from photons generated from this superposition across a range of arrival times as described above. However, because the frequency difference $\Delta_1 - \Delta_2$ of the bichromatic Raman field matches the frequency difference between the two states, the Raman process generates a photon that preserves the initial states' relative phase. As a result, the phase of the photon superposition is independent of detection time, as will be discussed further in the next section. This transfer scheme thus offers advantages for any quantum system in which a magnetic field lifts the degeneracy of the states encoding a qubit.

9.5 Time independence of the mapping process

If one employs a mapping protocol with one drive laser field (monochromatic) such as the one presented in [30], the phase of the atomic qubit changes due to Larmor precession if the atomic states involved are non-degenerate. This is a similar scenario as for the monochromatic entanglement protocols of refs. [25, 35, 126], in which the time interval between photon detection and atom detection has to be constant for all measurements if non-degenerate atomic states are involved. For a monochromatic mapping protocol, it is the time interval between the initialization of the atomic state and its mapping to the photon that has to be constant. Otherwise, the phase of the photon state will reveal the atom's Larmor precession [30]. In contrast, for the two Raman fields $\Omega_1 e^{i\omega_1 t}$ and $\Omega_2 e^{i\omega_2 t}$, the mapping field can be applied at any time for the correct choice of frequency $\omega_1 - \omega_2 = \Delta E_{S,S'}/\hbar$. For this choice, the phase of the photon state remains constant although the atomic state undergoes Larmor precession. We explain this result here, following the notation of sec. 8.6.

In contrast to sec. 8.6, the model system now consists of two initial states $|S, n\rangle$, $|S', n\rangle$, two intermediate states $|P, n\rangle$, $|P', n\rangle$ and only one target state $|D, n\rangle$, as indicated in fig. 9.4). The $|S, n\rangle \leftrightarrow |P, n\rangle$ transition is driven by the field $\Omega_1 e^{i\omega_1 t}$ at detuning $\Delta_{l_1} = \omega_S - \omega_P - \omega_{l_1}$, while the $|S', n\rangle \leftrightarrow |P', n\rangle$ transition is driven by the field $\Omega_2 e^{i\omega_2 t}$ at detuning $\Delta_{l_2} = \omega_{S'} - \omega_{P'} - \omega_{l_2}$.

We choose a unitary transformation that takes into account the atomic precession

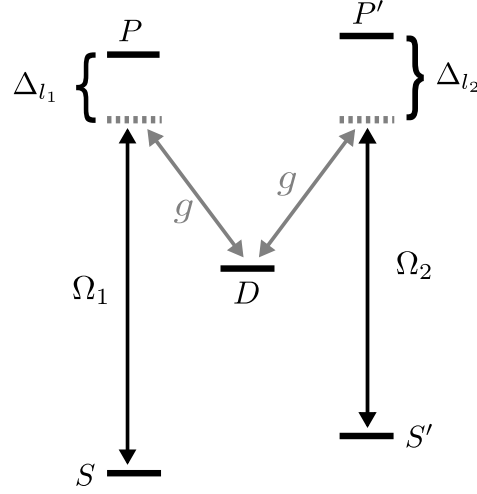


Figure 9.4: Model scheme of the mapping protocol. Indicated are the relevant levels S, S', P, P', D , the two driving fields with Rabi frequencies Ω_1, Ω_2 and detunings Δ_1, Δ_2 , and the vacuum field of the cavity with coupling strength g . In the case shown, both Raman conditions $\Delta_{l_1} = (\omega_D - \omega_P) - \omega_c$ and $\Delta_{l_2} = (\omega_D - \omega_{P'}) - \omega_c$ are fulfilled.

at the frequency $\omega_S - \omega_{S'}$:

$$U = e^{-i\omega_{l_1}t|S\rangle\langle S|} e^{-i\omega_{l_2}t|S'\rangle\langle S'|}. \quad (9.8)$$

After this transformation and adiabatic elimination of the state $|P, n\rangle$ (see section 2.3), the Hamiltonian is given by

$$\begin{aligned} \mathcal{H}/\hbar = & (\omega_S - \omega_P + \omega_{l_1}) |S\rangle\langle S| + (\omega_{S'} - \omega_P + \omega_{l_2}) |S'\rangle\langle S'| \\ & + (\omega_{P'} - \omega_P) |P'\rangle\langle P'| + (\omega_D - \omega_P) |D\rangle\langle D| \\ & + \omega_c |1\rangle\langle 1| + (g_1^{\text{eff}} |D, 1\rangle\langle S, 0| + g_2^{\text{eff}} |D, 1\rangle\langle S', 0| + \text{h.c.}), \end{aligned} \quad (9.9)$$

where the energy reference is the P state. Both ion-cavity couplings are time independent:

$$g_i^{\text{eff}} = \frac{\Omega_i \cdot g}{2\Delta_{l_i}}. \quad (9.10)$$

If we choose the frequencies of the two drive fields such that $|\omega_{l_1} - \omega_{l_2}| = |\omega_S - \omega_{S'}|$, corresponding to the Raman conditions $\omega_S + \omega_{l_1} = \omega_D + \omega_c = \omega_{S'} + \omega_{l_2}$, we calculate the energy of $|S', 0\rangle$ to be

$$\omega_{S'} - \omega_P + \omega_{l_2} = \omega_S - (\omega_S - \omega_{S'}) - \omega_P + \omega_{l_1} - (\omega_{l_1} - \omega_{l_2}) = \omega_S - \omega_P + \omega_{l_1}. \quad (9.11)$$

We conclude that the states $|S, 0\rangle$ and $|S', 0\rangle$ are degenerate in this frame, resulting in a constant phase of the atomic state. As the couplings are also time-independent, the phase φ of the mapped photonic state is constant at all times.

In the experiment, $|\omega_S - \omega_{S'}| \approx 12.6$ MHz, and $|\omega_{l_1} - \omega_{l_2}|$ is set via the RF signals send to the AOM, which can be controlled to a precision of 0.2 Hz (sec. 4.11). The time-independence of the mapping process is thus only limited by the residual differential AC-Stark shifts caused by the different detuning of the bichromatic field and different Clebsch-Gordan coefficients of the $P_{3/2} \leftrightarrow D_{5/2}$ transitions (sec. 9.2).

In this description, we have neglected off-resonant Raman transitions in which the drive laser Ω_1 and Ω_2 couple $|S', n\rangle$ to $|P', n\rangle$ and $|S, n\rangle$ to $|P, n\rangle$, respectively. Taking these transitions into account, the coupling terms in the Hamiltonian after transformation into the rotating frame and adiabatic elimination of $|P, n\rangle$ are identical to the ones in eq. (8.8). These coupling terms, oscillating at $|\omega_{l_1} - \omega_{l_2}|$, account for off-resonant Raman transitions. These terms were neglected in sec. 8.6 because $|g_i^{\text{eff}}| \ll |\omega_{l_1} - \omega_{l_2}|$ in the rotating wave approximation. However, these terms cannot be neglected on timescales shorter than $1/g_i^{\text{eff}}$, where the rotating wave approximation is no longer valid. On the time scale of ≤ 100 ns, these terms give rise to weak off-resonant Raman transitions that produce photons with undesired polarization. As a consequence, the process fidelity is low for the first datapoint of fig. 9.3. The rising probability to generate photons with the right polarization on longer timescales then results in a larger process fidelity for the second datapoint in fig. 9.3.

9.6 Conclusion

Following the deterministic initialization of an atomic qubit within a cavity, we have shown the coherent mapping of its quantum state onto a single photon. The mapping scheme achieves a high process fidelity, and by accepting compromises in fidelity, we increase the efficiency of the process within the cavity up to 14%. The transfer measurement is primarily limited by detector dark counts at 5.6 Hz, imperfect state initialization with a fidelity of 99%, magnetic-field fluctuations corresponding to an atomic coherence time of 110 μs , and the finite strength of the ion-cavity coupling in comparison to spontaneous decay rates. While a stronger coupling would improve the fidelity for a given efficiency, we note that the mapping fidelity in our current intermediate-coupling regime could also be improved by encoding the stationary qubit across multiple ions [157]. A direct application of this bichromatic mapping scheme is state transfer between two remote quantum nodes [22, 41]. Furthermore, via a modified bichromatic scheme, a single ion-cavity system can act as a deterministic source of photonic cluster states [158], an essential resource for measurement-based quantum computation [159].

10 Summary and Outlook

Summary

The goal of this dissertation was to explore the potential of an ion-cavity system for the realization of quantum network protocols.

As a first step, we have implemented tools for coherent initialization, manipulation, and state readout of the ion via laser pulses on the quadrupole transition. Furthermore, we extended the atomic coherence time by increasing the magnetic field stability. For interfacing the atomic qubit with a flying qubit, we optimized the ion-cavity coupling via improved cooling and precise positioning of the ion in all three dimensions.

We define the atomic qubit by the electronic state of the ion and the photonic qubit by the polarization of a single cavity photon. In order to couple these two qubits, we connect individual Zeeman substates of the atom via cavity-driven Raman transitions. Each Raman transition generates a single cavity photon. Its polarization is determined by the atomic states at which the Raman transitions starts and ends, as verified via spectroscopy. Finally, we have implemented a bichromatic scheme that drives two Raman transitions simultaneously. By selecting two appropriate transitions that produce photons with orthogonal polarization, we have realized two fundamental protocols of an ion-photon interface: ion-photon entanglement and state mapping.

The first protocol, entanglement between an ion and a photon, is regarded as a key resource of distributed quantum information processing. In our realization, we control both the phase and amplitudes of the entangled state. We verify the entanglement by quantum state tomography of the joint ion-photon state, resulting in a fidelity of 97.4% at near-unit photon-generation efficiency within the cavity. The second protocol, ion-photon state mapping, realizes the faithful transfer of the qubit state from the stationary to the flying qubit. In the future, quantum-state transfer between distant ions could be realized by connecting our cavity to a second ion-cavity apparatus. We characterize the ion-photon state mapping via quantum process tomography, yielding a process fidelity of 92.2% at a photon generation efficiency of 0.5%. This efficiency is increased to 15% by taking into account a longer time window for mapping, although in this case the fidelity decreases to 66% due to off-resonant excitation during the Raman process.

The high fidelities and efficiencies of the presented protocols are comparable to state-of-the art quantum interfaces that employ single neutral atoms in optical cavities [22, 29]. Although our apparatus does not realize strong atom-cavity coupling, this remarkable result is reached by the well-controlled localization of the ion in the resonator and the bichromatic driving scheme. In contrast to [22], the protocols pre-

sented in this dissertation combine a single-atom single-photon quantum interface with deterministic initialization and read-out of the atomic state. As a result, the success probability of any protocol that relies on the read-out of the atomic state (such as the quantum repeater) is increased by about one order of magnitude.

In summary, the results presented in this work offer a promising route towards networks connecting ion-based quantum computers. Moreover, the bichromatic driving scheme realized in this work ensures time independence of the quantum states in both protocols. As a result, this scheme is applicable to a range of physical systems incorporating non-degenerate qubit states.

Outlook

In the future, a prototype of a quantum network could be realized by two remote ion-cavity systems in a similar way as for neutral atoms in [22]. The ion-photon entanglement and state mapping protocols demonstrated here could then be applied to both systems to achieve direct state transfer and entanglement between distant ions. A second setup with a fiber cavity is under construction in our group. Although parameters of both setups will be different, the combination of both setups is possible. The temporal shape of photons from both setups can be overlapped via adjustment of the pulse shapes and Rabi frequencies of drive lasers [95]. Experiments involving both setups may then demonstrate a very efficient prototype of an ion-cavity quantum network.

In addition, two quantum interface protocols for one ion-trap cavity apparatus can be explored with the current setup. A first, direct application of the state-mapping protocol in a slightly modified version is the generation of photonic cluster states [158], a universal resource for measurement-based quantum computation [159]. In this protocol, the atom acts as a quantum memory and sequentially emits single photons interleaved with local operations on the memory. In an extension of this scheme, two or more ions could be used to generate two-dimensional photonic cluster states deterministically [107]. Although the original proposal considers quantum dots as photon emitters, an ion-cavity system presents itself as an optimal system: it combines the ability to perform local operations with perfect indistinguishability of the emitters.

The fidelity of the ion-photon state mapping protocol presented in this work is limited by off-resonant scattering due to a finite ion-cavity coupling. This limitation could be addressed by coupling multiple ions to the same cavity mode and encoding the logical qubit in the common state of all ions [157]. Entanglement between N ions would then increase the coupling of the logical qubit to the cavity by \sqrt{N} . In this way, well-established methods of generating entanglement of a string of ions [118] could be used to address the fundamental technical challenge of building a small cavity around an ion trap in order to obtain strong atom-cavity coupling.

A Battery circuit for trap-cavity piezo control

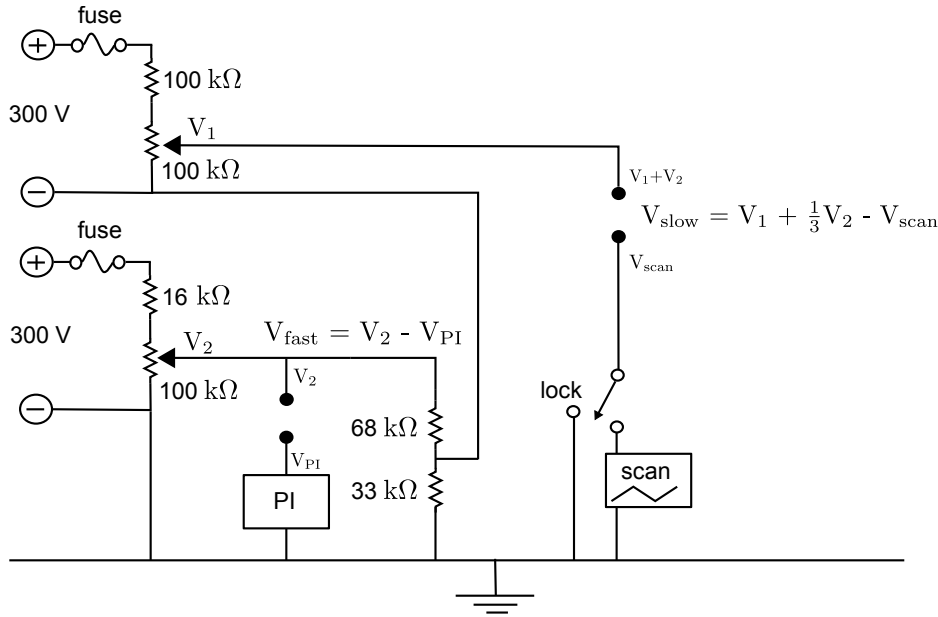


Figure A.1: High voltage battery circuit diagram.

Two 300 V batteries (Energizer EVEREADY 493) supply the voltages for the fast and slow piezo, tuned via 100 kΩ potentiometers. The fast piezo, responsible for stabilizing the cavity length, is connected on one electrode to the signal of a PI controller, and on the other electrode to the voltage V_2 . As the slow piezo needs about one third of the voltage in order to move by the same distance as the fast piezo, the slow piezo is driven by a fraction of $\sim 1/3$ of V_2 plus the voltage of the other battery V_1 . We can thus control the position of the cavity by changing V_2 while the cavity remains locked. A switch enables a scan mode where the second electrode of the slow piezo is connected to a signal generator in order to scan the cavity length. Higher values of the potentiometers and resistors would further reduce currents and therefore raise the battery lifetimes. However, 10-turn precision potentiometers with more than 100 kΩ resistance were not available at the time the circuit was built. They are available now and will be inserted in the future.

B Journal publications

The work presented in this thesis has given rise to a number of journal publications:

Tunable ion-photon entanglement in an optical cavity

A. Stute, B. Casabone, P. Schindler, T. Monz, P. O. Schmidt, B. Brandstätter, T. E. Northup and R. Blatt
Nature **485**, 482 (2012)

Quantum-state transfer from an ion to a photon

A. Stute*, B. Casabone*, B. Brandstätter, K. Friebe, T. E. Northup and R. Blatt
Nature photon. (accepted for publication)

Toward an ion-photon quantum interface in an optical cavity

A. Stute, B. Casabone, B. Brandstätter, D. Habicher, H. G. Barros, P. O. Schmidt, T. E. Northup and R. Blatt
Appl. Phys. B **107**, 1145 (2012)

Additional articles have been published in the framework of this thesis:

Quantum to classical transition in a single-ion laser

F. Dubin, C. Russo, H. G. Barros, A. Stute, C. Becher, P. O. Schmidt and R. Blatt
Nat. Phys. **6**, 350 (2010)

Deterministic single-photon source from a single ion

H. G. Barros, A. Stute, T. E. Northup, C. Russo, P. O. Schmidt and R. Blatt
New J. Phys. **11**, 103004 (2009)

Raman spectroscopy of a single ion coupled to a high-finesse cavity

C. Russo, H. G. Barros, A. Stute, F. Dubin, E. S. Phillips, T. Monz, T. E. Northup, C. Becher, T. Salzburger, H. Ritsch, P. O. Schmidt and R. Blatt
Appl. Phys. B **95**, 205 (2009)

Bibliography

- [1] P. Benioff, *The computer as a physical system: A microscopic quantum mechanical Hamiltonian model of computers as represented by Turing machines*, Journal of Statistical Physics **22**, 563 (1980).
- [2] R. P. Feynman, *Simulating physics with computers*, Int. J. Theor. Phys. **21**, 467 (1982).
- [3] P. W. Shor, *Algorithms for quantum computation: discrete logarithms and factoring*, in *Proc. Annu. Symp. Found. Comput. Sci.*, pp. 124–134 (1994).
- [4] L. Grover, *A fast quantum mechanical algorithm for database search*, in *Proceedings of the twenty-eighth annual ACM symposium on Theory of computing*, pp. 212–219, ACM (1996).
- [5] C. Bennett, G. Brassard, *et al.*, *Quantum cryptography: Public key distribution and coin tossing*, in *Proceedings of IEEE International Conference on Computers, Systems and Signal Processing*, vol. 175 (1984).
- [6] R. Hughes, *et al.*, *ARDA Quantum Computation Roadmap* (2004).
- [7] P. Zoller, *et al.*, *Quantum information processing and communication*, Eur. Phys. J. D **36**, 203 (2005).
- [8] P. Shor, *Fault-tolerant quantum computation*, in *Proceedings of IEEE 37th Annual Symposium on Foundations of Computer Science*, pp. 56–65, and arXiv:quant-ph/9605011v2 (1996).
- [9] P. W. Shor, *Scheme for reducing decoherence in quantum computer memory*, Phys. Rev. A **52**, R2493 (1995).
- [10] A. M. Steane, *Error Correcting Codes in Quantum Theory*, Phys. Rev. Lett. **77**, 793 (1996).
- [11] D. G. Cory, *et al.*, *Experimental Quantum Error Correction*, Phys. Rev. Lett. **81**, 2152 (1998).
- [12] J. Chiaverini, *et al.*, *Realization of quantum error correction*, Nature **432**, 602 (2004).

- [13] P. Schindler, *et al.*, *Experimental Repetitive Quantum Error Correction*, Science **332**, 1059 (2011).
- [14] H. J. Kimble, *The quantum internet*, Nature **453**, 1023 (2008).
- [15] L.-M. Duan and C. Monroe, *Colloquium: Quantum networks with trapped ions*, Rev. Mod. Phys. **82**, 1209 (2010).
- [16] C. Monroe, *Quantum information processing with atoms and photons*, Nature **416**, 238 (2002).
- [17] S. Barz, *et al.*, *Demonstration of blind quantum computing*, Science **335**, 303 (2012).
- [18] D. P. DiVincenzo, *The physical implementation of quantum computation*, Fortschr. Phys. **48**, 771 (2000).
- [19] R. Ursin, *et al.*, *Entanglement-based quantum communication over 144 km*, Nature Phys. **3**, 481 (2007).
- [20] L.-M. Duan and H. J. Kimble, *Efficient engineering of multiatom entanglement through single-photon detections*, Phys. Rev. Lett. **90**, 253601 (2003).
- [21] J. Volz, *et al.*, *Observation of Entanglement of a Single Photon with a Trapped Atom*, Phys. Rev. Lett. **96**, 030404 (2006).
- [22] S. Ritter, *et al.*, *An elementary quantum network of single atoms in optical cavities*, Nature **484**, 195 (2012).
- [23] A. Kuzmich, *et al.*, *Generation of nonclassical photon pairs for scalable quantum communication with atomic ensembles.*, Nature **423**, 731 (2003).
- [24] C. W. Chou, *et al.*, *Measurement-induced entanglement for excitation stored in remote atomic ensembles*, Nature **438**, 828 (2005).
- [25] B. B. Blinov, D. L. Moehring, L. M. Duan, and C. Monroe, *Observation of entanglement between a single trapped atom and a single photon*, Nature **428**, 153 (2004).
- [26] J. McKeever, *et al.*, *Deterministic generation of single photons from one atom trapped in a cavity*, Science **303**, 1992 (2004).
- [27] H. G. Barros, *et al.*, *Deterministic single-photon source from a single ion*, New J. Phys. **11**, 103004 (2009).
- [28] R. Miller, *et al.*, *Trapped atoms in cavity QED: coupling quantized light and matter*, J. Phys. B **38**, S551 (2005).

-
- [29] A. D. Boozer, *et al.*, *Reversible State Transfer between Light and a Single Trapped Atom*, Phys. Rev. Lett. **98**, 193601 (2007).
- [30] H. P. Specht, *et al.*, *A single-atom quantum memory*, Nature **473**, 190 (2011).
- [31] S. Olmschenk, *et al.*, *Quantum Teleportation Between Distant Matter Qubits*, Science **323**, 486 (2009).
- [32] J. M. Raimond, M. Brune, and S. Haroche, *Manipulating quantum entanglement with atoms and photons in a cavity*, Rev. Mod. Phys. **73**, 565 (2001).
- [33] D. N. Matsukevich, *et al.*, *Entanglement of a Photon and a Collective Atomic Excitation*, Phys. Rev. Lett. **95**, 040405 (2005).
- [34] J. Sherson, *et al.*, *Quantum teleportation between light and matter*, Nature **443**, 557 (2006).
- [35] E. Togan, *et al.*, *Quantum entanglement between an optical photon and a solid-state spin qubit*, Nature **466**, 730 (2010).
- [36] D. L. Moehring, *et al.*, *Entanglement of single-atom quantum bits at a distance*, Nature **449**, 68 (2007).
- [37] J. Simon, H. Tanji, and V. Saikat Ghosh, *Single-photon bus connecting spin-wave quantum memories*, Nature Phys. **3**, 765 (2007).
- [38] J. Hofmann, *et al.*, *Heralded Entanglement Between Widely Separated Atoms*, Science **337**, 72 (2012).
- [39] W. K. Wootters, *Entanglement of formation of an arbitrary state of two qubits*, Phys. Rev. Lett. **80**, 2245 (1998).
- [40] H.-J. Briegel, W. Dür, J. I. Cirac, and P. Zoller, *Quantum repeaters: the role of imperfect local operations in quantum communication*, Phys. Rev. Lett. **81**, 5932 (1998).
- [41] J. I. Cirac, P. Zoller, H. J. Kimble, and H. Mabuchi, *Quantum State Transfer and Entanglement Distribution among Distant Nodes in a Quantum Network*, Phys. Rev. Lett. **78**, 3221 (1997).
- [42] D. Leibfried, R. Blatt, C. Monroe, and D. Wineland, *Quantum dynamics of single trapped ions*, Rev. Mod. Phys. **75**, 281 (2003).
- [43] H. Häffner, C. Roos, and R. Blatt, *Quantum computing with trapped ions*, Phys. Rep. **469**, 155 (2008).

- [44] M. J. Gibbons, C. D. Hamley, C.-Y. Shih, and M. S. Chapman, *Nondestructive Fluorescent State Detection of Single Neutral Atom Qubits*, Phys. Rev. Lett. **106**, 133002 (2011).
- [45] A. Fuhrmanek, R. Bourgain, Y. R. P. Sortais, and A. Browaeys, *Free-Space Lossless State Detection of a Single Trapped Atom*, Phys. Rev. Lett. **106**, 133003 (2011).
- [46] G. R. Guthöhrlein, *et al.*, *A single ion as a nanoscopic probe of an optical field*, Nature **414**, 49 (2001).
- [47] A. B. Mundt, *et al.*, *Coupling a Single Atomic Quantum Bit to a High Finesse Optical Cavity*, Phys. Rev. Lett. **89**, 103001 (2002).
- [48] C. Russo, *et al.*, *Raman spectroscopy of a single ion coupled to a high-finesse cavity*, Appl. Phys. B **95**, 205 (2009).
- [49] D. R. Leibbrandt, J. Labaziewicz, V. Vuletić, and I. L. Chuang, *Cavity Sideband Cooling of a Single Trapped Ion*, Phys. Rev. Lett. **103**, 103001 (2009).
- [50] P. Herskind, *et al.*, *Realization of collective strong coupling with ion Coulomb crystals in an optical cavity*, Nat. Phys. **5**, 494 (2009).
- [51] J. D. Sterk, *et al.*, *Photon collection from a trapped ion-cavity system*, Phys. Rev. A **85**, 062308 (2012).
- [52] A. Stute, *et al.*, *Toward an ion-photon quantum interface in an optical cavity*, Appl. Phys. B **107**, 1145 (2012).
- [53] A. Stute, *et al.*, *Tunable ion-photon entanglement in an optical cavity*, Nature **485**, 482 (2012).
- [54] A. Stute, *et al.*, *Quantum state transfer from an ion to a photon*, in preparation.
- [55] J. Audretsch, *Verschränkte Systeme*, Wiley-VCH, Weinheim (2005).
- [56] J. Benhelm, *Precision Spectroscopy and Quantum Information Processing with Trapped Calcium Ions*, Ph.D. thesis, Universität Innsbruck (2008).
- [57] T. J. Weinhold, *Stepping stones towards linear optical quantum computing*, Ph.D. thesis, University of Queensland (2010).
- [58] E. T. Jaynes and F. W. Cummings, *Comparison of quantum and semiclassical radiation theories with application to the beam maser*, Proc. IEEE **51**, 89 (1963).
- [59] B. Shore, *The Theory of Coherent Atomic Excitation*, Wiley, New York (1990).

-
- [60] M. O. Scully, G. M. Meyer, and H. Walther, *Induced Emission due to the Quantized Motion of Ultracold Atoms Passing through a Micromaser Cavity*, Phys. Rev. Lett. **76**, 4144 (1996).
- [61] C. Cohen-Tannoudji, *Atom-Photon-Interactions*, Wiley (1992).
- [62] C. W. Gardiner, J. Ye, H. C. Nagerl, and H. J. Kimble, *Evaluation of heating effects on atoms trapped in an optical trap*, Phys. Rev. A **61**, 045801 (2000).
- [63] H. Carmichael, *An Open Systems Approach to Quantum Optics*, Springer (1993).
- [64] C. Gardiner and P. Zoller, *Quantum Noise: A Handbook Of Markovian And Non-markovian Quantum Stochastic Methods With Applications To Quantum Optics*, Springer Series in Synergetics, Springer, Berlin (2004).
- [65] C. M. da Silva Baptista Russo, *Photon statistics of a single ion coupled to a high-finesse cavity*, Ph.D. thesis, Universität Innsbruck (2008).
- [66] R. J. Glauber, *Coherent and Incoherent States of the Radiation Field*, Phys. Rev. **131**, 2766 (1963).
- [67] C. C. Gerry and J. H. Eberly, *Dynamics of a Raman coupled model interacting with two quantized cavity fields*, Phys. Rev. A **42**, 6805 (1990).
- [68] M. Alexanian and S. K. Bose, *Unitary transformation and the dynamics of a three-level atom interacting with two quantized field modes*, Phys. Rev. A **52**, 2218 (1995).
- [69] Y. Wu, *Effective Raman theory for a three-level atom in the Λ configuration*, Phys. Rev. A **54**, 1586 (1996).
- [70] C. Di Fidio, S. Maniscalco, W. Vogel, and A. Messina, *Cavity QED with a trapped ion in a leaky cavity*, Phys. Rev. A **65**, 033825 (2002).
- [71] D. Kielpinski, *et al.*, *A Decoherence-Free Quantum Memory Using Trapped Ions*, Science **291**, 1013 (2001).
- [72] C. Roos, *et al.*, *'Designer atoms' for quantum metrology*, Nature **443**, 316 (2006).
- [73] C. Monroe, *et al.*, *Demonstration of a Fundamental Quantum Logic Gate*, Phys. Rev. Lett. **75**, 4714 (1995).
- [74] G. Kirchmair, *et al.*, *High-fidelity entanglement of $^{43}\text{Ca}^+$ hyperfine clock states*, Phys. Rev. A **79**, 020304 (2009).
- [75] C. F. Roos, *et al.*, *Bell States of Atoms with Ultralong Lifetimes and Their Tomographic State Analysis*, Phys. Rev. Lett. **92**, 220402 (2004).

- [76] J. Jin and D. A. Church, *Precision lifetimes for the Ca^+ $4p^2P$ levels: Experiment challenges theory at the 1% level*, Phys. Rev. Lett. **70**, 3213 (1993).
- [77] P. A. Barton, *et al.*, *Measurement of the lifetime of the $3d^2D_{5/2}$ state in $^{40}\text{Ca}^+$* , Phys. Rev. A **62**, 032503 (2000).
- [78] D. James, *Quantum dynamics of cold trapped ions with application to quantum computation*, Appl. Phys. B **66**, 181 (1998).
- [79] R. Gerritsma, *et al.*, *Precision measurement of the branching fractions of the $4p\ 2P_{3/2}$ decay of Ca II*, Eur. Phys. J. D **50**, 13 (2008).
- [80] R. Loudon, *The Quantum Theory of Light*, Oxford Science Publications, Oxford (1983).
- [81] J. J. Sakurai, *Modern Quantum Mechanics*, Addison-Wesley (1994).
- [82] S. M. Tan, *A computational toolbox for quantum and atomic optics*, J. Opt. B: Quantum Semiclass. Opt. **1**, 424 (1999).
- [83] B. Brandstätter, *Development of an ion trap with an integrated fiber Fabry-Perot resonator for cavity QED experiments*, Ph.D. thesis, Universität Innsbruck, in preparation.
- [84] F. Dubin, *et al.*, *Quantum to classical transition in a single-ion laser*, Nat. Phys. **6**, 350 (2010).
- [85] H. G. de Barros, *Raman spectroscopy and single-photon source in an ion-cavity system*, Ph.D. thesis, Universität Innsbruck (2010).
- [86] D. Meschede, H. Walther, and G. Müller, *One-Atom Maser*, Phys. Rev. Lett. **54**, 551 (1985).
- [87] S. Gleyzes, *et al.*, *Quantum jumps of light recording the birth and death of a photon in a cavity.*, Nature **446**, 297 (2007).
- [88] P. Maunz, *et al.*, *Cavity cooling of a single atom*, Nature **428**, 50 (2004).
- [89] Harlander, M. Brownnutt, W. Hänsel, and R. Blatt, *Trapped-ion probing of light-induced charging effects on dielectrics*, New J. Phys. **12**, 093035 (2010).
- [90] M. Brownnutt, M. Kumph, P. Rabl, and R. Blatt, *Electro-magnetic field noise near surfaces*, in preparation.
- [91] S. T. Gulde, *Experimental Realization of Quantum Gates and the Deutsch-Jozsa Algorithm with Trapped $^{40}\text{Ca}^+$ Ions*, Ph.D. thesis, Universität Innsbruck (2003).

-
- [92] W. Paul, *Electromagnetic traps for charged and neutral particles*, Rev. Mod. Phys. **62**, 531 (1990).
- [93] A. E. Siegman, *Lasers*, University Science Books, Sausalito, CA (1986).
- [94] M. Albert, *et al.*, *Collective strong coupling between ion Coulomb crystals and an optical cavity field: Theory and experiment*, Phys. Rev. A **85**, 023818 (2012).
- [95] M. Keller, *et al.*, *Continuous generation of single photons with controlled waveform in an ion-trap cavity system*, Nature **431**, 1075 (2004).
- [96] T. Monz, *A Frequency Offset Lock for Cavity-Driven Raman Transitions*, Master's thesis, Universität Innsbruck (2005).
- [97] M. Chwalla, *Precision spectroscopy with $^{40}\text{Ca}^+$ ions in a Paul trap*, Ph.D. thesis, Universität Innsbruck (2009).
- [98] E. Black, *An introduction to Pound–Drever–Hall laser frequency stabilization*, Am. J. Phys. **69**, 79 (2001).
- [99] L.-S. Ma, P. Jungner, J. Ye, and J. L. Hall, *Delivering the same optical frequency at two places: accurate cancellation of phase noise introduced by an optical fiber or other time-varying path*, Opt. Lett. **19**, 1777 (1994).
- [100] G. Kirchmair, *Quantum non-demolition measurements and quantum simulation*, Ph.D. thesis, Universität Innsbruck (2010).
- [101] D. Habicher, *Abbildung, Adressierung und Zustandsdetektion zweier Ionen in einem optischen Resonator*, Master's thesis, Universität Innsbruck (2011).
- [102] A. B. Mundt, *Cavity QED with Single Trapped Ca^+ -Ions*, Ph.D. thesis, Universität Innsbruck (2003).
- [103] B. H. Rhode, *Experimente zur Quanteninformationsverarbeitung in einer linearen Ionenfalle*, Ph.D. thesis, Universität Innsbruck (2001).
- [104] C. F. Roos, *Controlling the quantum state of trapped ions*, Ph.D. thesis, Universität Innsbruck (2000).
- [105] E. Hecht, *Optics*, Addison Wesley, 4 edn. (2001).
- [106] P. Cristofolini, *Entwurf und Bau eines beugungsbegrenzten Objektivs*, Universität Innsbruck (2009).
- [107] S. E. Economou, N. Lindner, and T. Rudolph, *Optically Generated 2-Dimensional Photonic Cluster State from Coupled Quantum Dots*, Phys. Rev. Lett. **105**, 093601 (2010).

- [108] D. F. V. James, P. G. Kwiat, W. J. Munro, and A. G. White, *Measurement of qubits*, Phys. Rev. A **64**, 052312 (2001).
- [109] P. Schindler, *Frequency synthesis and pulse shaping for quantum information processing with trapped ions*, Master's thesis, Universität Innsbruck (2008).
- [110] P. Pham, *A general-purpose pulse sequencer for quantum computing*, Master's thesis, Massachusetts Institute of Technology (2005).
- [111] D. Wineland and W. Itano, *Laser cooling of atoms*, Physical Review A **20**, 1521 (1979).
- [112] H. J. Metcalf and P. van der Straten, *Laser Cooling and Trapping*, Springer, New York, 2nd edn. (2001).
- [113] J. Eschner, *et al.*, *Laser cooling of trapped ions*, J. Opt. Soc. Am. B **20**, 1003 (2003).
- [114] G. Alzetta, A. Gozzini, L. Moi, and G. Orriols, *An experimental method for the observation of r.f. transitions and laser beat resonances in oriented Na vapour*, Il Nuovo Cimento B **36**, 5 (1976).
- [115] A. H. Myerson, *et al.*, *High-Fidelity Readout of Trapped-Ion Qubits*, Phys. Rev. Lett. **100**, 200502 (2008).
- [116] J. I. Cirac and P. Zoller, *Quantum Computations with Cold Trapped Ions*, Phys. Rev. Lett. **74**, 4091 (1995).
- [117] A. Sørensen and K. Mølmer, *Quantum Computation with Ions in Thermal Motion*, Phys. Rev. Lett. **82**, 1971 (1999).
- [118] J. Benhelm, G. Kirchmair, C. F. Roos, and R. Blatt, *Towards fault-tolerant quantum computing with trapped ions*, Nat. Phys. **4**, 463 (2008).
- [119] G. Kirchmair, *et al.*, *Deterministic entanglement of ions in thermal states of motion*, New Journal of Physics **11**, 023002 (2009).
- [120] Q. A. Turchette, *et al.*, *Heating of trapped ions from the quantum ground state*, Phys. Rev. A **61**, 063418 (2000).
- [121] N. F. Ramsey, *Experiments with separated oscillatory fields and hydrogen masers*, Rev. Mod. Phys. **62**, 541 (1990).
- [122] T. Monz, *et al.*, *14-qubit entanglement: creation and coherence*, Phys. Rev. Lett. **106**, 130506 (2011).

-
- [123] T. Monz, *et al.*, *Realization of Universal Ion-Trap Quantum Computation with Decoherence-Free Qubits*, Phys. Rev. Lett. **103**, 200503 (2009).
- [124] D. Berkeland, *et al.*, *Minimization of ion micromotion in a Paul trap*, Journal of applied physics **83**, 5025 (1998).
- [125] Eschner, *Sub-wavelength resolution of optical fields probed by single trapped ions: Interference, phase modulation, and which-way information*, Eur. Phys. J. D **22**, 341 (2003).
- [126] T. Wilk, S. C. Webster, A. Kuhn, and G. Rempe, *Single-Atom Single-Photon Quantum Interface*, Science **317**, 488 (2007).
- [127] A. S. Parkins and H. J. Kimble, *Quantum state transfer between motion and light*, J. Opt. B: Quantum Semiclass. Opt. **1**, 496 (1999).
- [128] C. Law and H. Kimble, *Deterministic generation of a bit-stream of single-photon pulses*, J. Mod. Opt. **44**, 2067 (1997).
- [129] B. Weber, *et al.*, *Photon-Photon Entanglement with a Single Trapped Atom*, Phys. Rev. Lett. **102**, 030501 (2009).
- [130] P. Maunz, *et al.*, *Heralded Quantum Gate between Remote Quantum Memories*, Phys. Rev. Lett. **102**, 250502 (2009).
- [131] A. Einstein, B. Podolsky, and N. Rosen, *Can Quantum-Mechanical Description of Physical Reality Be Considered Complete?*, Phys. Rev. **47**, 777 (1935).
- [132] E. Schrödinger, *Die gegenwärtige Situation der Quantenmechanik*, Die Naturwissenschaften **48**, 807 (1935).
- [133] J. Bell, *On the Einstein Podolsky Rosen Paradox*, Physics **1**, 195 (1964).
- [134] S. Hill and W. K. Wootters, *Entanglement of a Pair of Quantum Bits*, Phys. Rev. Lett. **78**, 5022 (1997).
- [135] J. F. Clauser, M. A. Horne, A. Shimony, and R. A. Holt, *Proposed Experiment to Test Local Hidden-Variable Theories*, Phys. Rev. Lett. **23**, 880 (1969).
- [136] A. Aspect, P. Grangier, and G. Roger, *Experimental Tests of Realistic Local Theories via Bell's Theorem*, Phys. Rev. Lett. **47**, 460 (1981).
- [137] P. G. Kwiat, *et al.*, *New High-Intensity Source of Polarization-Entangled Photon Pairs*, Phys. Rev. Lett. **75**, 4337 (1995).
- [138] W. Tittel, J. Brendel, H. Zbinden, and N. Gisin, *Violation of Bell Inequalities by Photons More Than 10 km Apart*, Phys. Rev. Lett. **81**, 3563 (1998).

- [139] G. Weihs, *et al.*, *Violation of Bell's Inequality under Strict Einstein Locality Conditions*, Phys. Rev. Lett. **81**, 5039 (1998).
- [140] M. Rowe, *et al.*, *Experimental violation of a Bell's inequality with efficient detection*, Nature **409**, 791 (2001).
- [141] Y. Hasegawa, *et al.*, *Violation of a Bell-like inequality in neutron optical experiments: quantum contextuality*, Journal of Optics B: Quantum and Semiclassical Optics **6**, S7 (2004).
- [142] D. L. Moehring, M. J. Madsen, B. B. Blinov, and C. Monroe, *Experimental Bell Inequality Violation with an Atom and a Photon*, Phys. Rev. Lett. **93**, 090410 (2004).
- [143] N. Brunner, N. Gisin, V. Scarani, and C. Simon, *Detection Loophole in Asymmetric Bell Experiments*, Phys. Rev. Lett. **98**, 220403 (2007).
- [144] A. Aspect, J. Dalibard, and G. Roger, *Experimental Test of Bell's Inequalities Using Time-Varying Analyzers*, Phys. Rev. Lett. **49**, 1804 (1982).
- [145] N. Gisin, G. Ribordy, W. Tittel, and H. Zbinden, *Quantum cryptography*, Rev. Mod. Phys. **74**, 145 (2002).
- [146] W. Rosenfeld, *et al.*, *Towards a loophole-free test of Bell's inequality with entangled pairs of neutral atoms*, Advanced science letters **2**, 469 (2009).
- [147] M. Hijlkema, *et al.*, *A single-photon server with just one atom*, Nat. Phys. **3**, 253 (2007).
- [148] M. S. Kaznady and D. F. V. James, *Numerical strategies for quantum tomography: Alternatives to full optimization*, Phys. Rev. A **79**, 022109 (2009).
- [149] T. Monz, *Quantum information processing beyond ten ion-qubits*, Ph.D. thesis, Universität Innsbruck (2011).
- [150] Z. Hradil, *Quantum-state estimation*, Phys. Rev. A **55**, R1561 (1997).
- [151] B. Efron and R. Tibshirani, *An introduction to the bootstrap*, Chapman & Hall, New York (1993).
- [152] A. Davison and D. Hinkley, *Bootstrap methods and their application*, Cambridge Univ. Press, New York (1997).
- [153] M. A. Nielsen and I. L. Chuang, *Quantum Computation and Quantum Information*, Cambridge University Press, Cambridge (2010).

- [154] G. Rempe, *et al.*, *Optical bistability and photon statistics in cavity quantum electrodynamics*, Phys. Rev. Lett. **67**, 1727 (1991).
- [155] M. Ježek, J. Fiurášek, and Z. Hradil, *Quantum inference of states and processes*, Phys. Rev. A **68**, 012305 (2003).
- [156] M. Horodecki, P. Horodecki, and R. Horodecki, *General teleportation channel, singlet fraction, and quasidistillation*, Phys. Rev. A **60**, 1888 (1999).
- [157] L. Lamata, *et al.*, *Ion Crystal Transducer for Strong Coupling between Single Ions and Single Photons*, Phys. Rev. Lett. **107**, 030501 (2011).
- [158] N. H. Lindner and T. Rudolph, *Proposal for Pulsed On-Demand Sources of Photonic Cluster State Strings*, Phys. Rev. Lett. **103**, 113602 (2009).
- [159] R. Raussendorf and H. J. Briegel, *A One-Way Quantum Computer*, Phys. Rev. Lett. **86**, 5188 (2001).

Bibliography

Danksagung

Es war mir eine Freude, mit so wundervollen Menschen an diesem interessanten Thema zu arbeiten. Allen, die zu dieser Arbeit beigetragen haben, möchte ich für ihre wissenschaftliche wie menschliche Unterstützung danken.

An erster Stelle gebührt dieser Dank Rainer Blatt, der mich in seiner Forschungsgruppe willkommen hieß und immer fest an den Erfolg unserer Experimente glaubte.

Tracy Northup und Piet Schmidt gehören zu den sympathischsten Betreuern, die man finden kann. Ihre Türen standen immer offen für Fragen und sie haben stets eine Atmosphäre geschaffen, in der es eine Freude war, unsere Messungen sowie neue Ideen zu diskutieren. Tracy war auch eine große Hilfe im Labor, besonders, als wir den Laser auf dem Quadrupolübergang in unser Experiment integrierten. Bei der Korrektur dieser Arbeit hat sie einen sehr positiven Einfluss auf meine englischen Schreibkünste gehabt. Vielen Dank! Piet verdanke ich einen Großteil meiner Laserlockkenntnisse. Er brachte mir auch alle Handgriffe bei, die man benötigt, um einen Ti:Sa Laser zu zähmen.

Die meiste Zeit für diese Arbeit habe ich gemeinsam mit Bernardo Casabone und Helena Barros bei den Messungen im Labor verbracht. Ihnen möchte ich für den hohen Einsatz und die fantastische Zusammenarbeit danken. Bei Bernardo möchte ich mich für seinen Enthusiasmus bedanken, und seine schnelle Auffassungsgabe, mit der er sich in unser Experiment einarbeitete: Gracias por tu entusiasmo que siempre contribuías al experimento y tu gran esfuerzo en el laboratorio. Colaborar contigo fue un gran enriquecimiento para mí! Von Helena lernte ich alle wichtigen Handgriffe an unserem Transferlasertisch, sowie mit Geduld an die Experimente zu gehen.

Dem ganzen weiteren cavity-QED Team danke ich für die intensive Zusammenarbeit über viele Jahre: Carlos Russo, Birgit Brandstätter, Francois Dubin, Konstantin Friebe, Johannes Ghetta und Klemens Schüppert. Es war eine Bereicherung, von ihnen zu lernen und mit ihnen über die Grundsätze unserer Experimente zu diskutieren. Besonderer Dank geht natürlich an Carlos Russo: Nicht nur für die Konstruktion unseres experimentellen Aufbaus, sondern auch, weil ich über sein Poster den Weg nach Innsbruck gefunden habe. Birgit danke ich für ihre Simulationen, die einen großen Beitrag zum Verständnis des Zustandstransfers geleistet haben.

Dem ganzen $^{40}\text{Ca}^+$ Team danke ich für den Humor im Labor und die viele Arbeit mit unseren gemeinsamen Lasern. Es war großartig, mit Euch ein Labor zu teilen! Ihre Kenntnisse haben unser Experiment erheblich beschleunigt: Philipp Schindler half uns bei der Erweiterung der Pulse Box, Thomas Monz, Philipp und Daniel Nigg bei der Zustands- und Prozesstomographie, und Mike Chwalla hat das Licht von seinem 729nm-Laser spendiert.

Christian Roos, Gerhard Kirchmair, Wolfgang Hänsel und Markus Henrich danke ich für das Weitergeben ihres Know-Hows des Ionenfangens und anregende Diskussionen über die Grundsätze der Quantenoptik. Christian und Gerhard gaben uns viele hilfreiche Ratschläge, als wir den 729nm-Laser in unseren Aufbau integrierten.

Lukas Slodicka, Andrew White und Julio Barreiro haben uns Ideen für die Justage der Polarisationsdetektion gegeben, und Klemens Hammerer hat mit uns Ideen für neue Experimente diskutiert.

Großer Dank geht auch an Michael Hofer und Wolfgang Kratz von der Elektronikwerkstatt für ihre Hilfe beim Reparieren unserer Ti:Sa-Elektronikbox, nachdem Kühlflüssigkeit von einem geplatzten Rohr den Hochspannungsteil der Schaltung zerstört hatte. Ihre Ruhe und Sorgfalt waren in dieser Situation Balsam für meine Seele.

Bei Andreas Reinalter, Anton Schönherr, Helmut Jordan und Armin Sailer von der mechanischen Werkstatt bedanke ich mich für die sorgfältige Fertigung vieler Teile, die wir im Laufe der Jahre an das Experiment angebaut haben.

Patricia Moser, Karin Köhle, Renate Kemedinger, Ingeborg Kaindl, Nicole Jorda und Christine Götsch-Obmascher danke ich für die unkomplizierte Hilfe mit allen administrativen Aufgaben.

Nicht zu vergessen sind meine Freunde, meine WG, die Big Band der Musikschule und das Team des Öztalmarathons. Sie haben es geschafft, mich oft genug aus dem Labor zu locken und meinen Alltag enorm zu bereichern.

Meiner Familie danke ich für die Freiheit und die Unterstützung, die sie mir stets gegeben hat, den Weg zu gehen, den ich für richtig hielt. Am meisten danke ich dir, Mira, für die Begleitung auf hohe Gipfel und durch tiefe Täler und all deine Geduld und Unterstützung auf diesem langen Weg.